Chan Joshi

UNIVERSITY OF CALIFORNIA

Los Angeles

Theory and Simulations on Beat Wave Excitation of Relativistic Plasma Waves

A dissertation submitted in partial satisfaction of the requirements for the degree of Doctor of Philosophy in Electrical Engineering

by

Warren Bicknell Mori

1987

To my family

Hideo, Ann, Susanne, Bruce, and Quincy

LIST OF SYMBOLS

ω_o	frequency difference of lasers
ω_o	pump frequency
$\omega_{1,2}$	laser frequencies
ω_p	plasma frequency
ω_{po}	average plasma frequency
ω_{pi}	ion plasma frequency
ω_{BG}	Bohm Gross frequency
ω_{ac}	ion acoustic frequency
ω_-	stokes frequency
ω_+	anti-stokes frequency
$\Delta\omega$	frequency difference
κ_o	wave number difference of lasers
$\kappa_{1,2}$	laser wave numbers
κ	density ripple wave number
κ	Boltzmans constant
$\Delta\kappa$	wave number difference
k	idler wave number
k_o	pump wave number
k_-	stokes wave number
k_+	anti-stokes wave number

e	electron charge
e_m	peak normalized ($mc\omega_p/e$) amplitude of first harmonic
e_j	normalized ($mc\omega_p/e$) electric field amplitude of $(j-1)$ harmonic
e_f	value of e_o at the fixed point
δe	$e_o - e_f$
v_j	normalized (c) fluid velocity of $(j-1)$ harmonic
v_ϕ	wave phase velocity
v_{go}	light wave group velocity
n_j	normalized ($\bar{n}_o$) density of $(j-1)$ harmonic
N	total electron density
n_i	ion density
γ	relativistic Lorentz factor
γ	phenomological damping coefficient
γ_ϕ	relativistic Lorentz factor for $v=v_\phi$
$\bar{\gamma}$	normalized $(27F^2C/4)^{1/3}$ damping
ξ	Lagrangian fluid displacement
x_o	Lagrangian position coordinate
$\alpha_{1,2}$	normalized ($mc\omega_{1,2}/e$) electric field of lasers
m	electron mass
M	ion mass

L_o	laser beam cross section
v_{th}	electron thermal velocity $(\kappa T_e/m)^{1/2}$
a_e	modified electron thermal velocity $(2\kappa T_e/m)^{1/2}$
T_e	electron temperature
T_i	ion temperature
ϵ	perturbation expansion parameter
ϵ	dielectric function
ϵ	amplitude of ion density
ϵ_j	coupling constant in nonlinear wave equation
c_j	velocity in wave equation
c	speed of light
C	$(3/16)(\omega_p^2/\omega_o^2)(v_o^2/c^2)\omega_o$
F	amplitude of beat wave driving force $\alpha_1\alpha_2\omega_o/4$
F_o	$2F$
F_o	peak value of F in rise time
δ	$\omega_p - \omega_o$
Δ	$\omega_p^2 - \omega_o^2$
Δ	$\Delta_o + F$
Δ_o	mismatch $(\omega_o^2 - \omega_p^2)/2\omega_o$
Δ_c	$-(27F^2C/2)^{1/3}$
$\bar{\Delta}$	$\Delta(27F^2C/4)^{-1/3}$
τ	laser rise time

t_s	beat wave growth time
E_o	normalized pump amplitude
E_-	normalized stokes amplitude
E_+	normalized anti-stokes amplitude
J_n	n^{th} order ordinary Bessel function of the first kind
ψ_o	phase difference of lasers $(\kappa_o x - \omega_o t)$
$\bar{\psi}_o$	$(\kappa_o x + \omega_o t)$
ψ_m	phase that maximizes E_x
ψ	phase of plasma wave $(\kappa_o x - \omega_o t + \phi)$
ϕ_f	value of ϕ at the fixed point
y	sine ϕ
y_f	sine ϕ_f
δy	$y - y_f$

ACKNOWLEDGEMENTS

In the course of this research I have been blessed with the support of many people.

I am grateful for the advice, patience, and computer time from the X-1 group at Los Alamos during my three summers as a GRA. Special thanks go to my advisers away from UCLA, Dave Forslund and Joe Kindel, for their selfless support and guidance. Working with Dave was a special treat.

Every graduate student needs and values the friendship and camaraderie of their office mates. My office mates were Tom Katsouleas, Jose Milovich, Chris Darrow, and Inge Jechart. For the endless hours of useful and useless discussions, I thank you.

I benefited from many conversations with Bob Bingham and Colin McKinstrie at various conferences and workshops.

I have been fortunate to have had a triumvirate of advisers at UCLA. I thank Prof. Chen for his insistence on clarity and his probing questions during our weekly group meetings and his office hours. For his enthusiasm, insight, and ideas during our discussions, I thank Prof. Dawson. Whatever I have become as a researcher I owe mostly to Chan Joshi for his patience and guidance over the years.

Last, I thank my mother for her time and effort in typing this dissertation.

VITA

August 8, 1959--Born, Weymouth, Massachusetts

1981--B.S., University of California, Berkeley

1982-1987--Research Assistant, Department of Electrical Engineering and Department of Physics, University of California at Los Angeles

1983-1985--Summer Graduate Research Assistant, Los Alamos National Laboratory

1984--M.S., University of California at Los Angeles

PUBLICATIONS

W. B. Mori, C. Joshi, and J. M. Dawson, "A Plasma Wave Accelerator - Surfatron II," IEEE Trans. on Nucl. Sci. NS-30, 3244 (1983).

T. Katsouleas, C. Joshi, W. B. Mori, J. M. Dawson, and F. F. Chen, "Prospects of the Surfatron Laser Plasma Accelerator," Proc. 12th Intl. Conf. on High Energy Accelerators, Fermilab (1983).

C. Joshi, W. B. Mori, T. Katsouleas, J. M. Dawson, J. M. Kindel, and D. W. Forslund, "Ultra-High Gradient Particle Acceleration by Intense Laser-Driven Plasma Density Waves," Nature 311, 525 (1984).

J. M. Kindel, D. W. Forslund, W. B. Mori, C. Joshi, and J. M. Dawson, "Plasma Simulation Studies of Electron Acceleration

for Beat Wave and Single Frequency Laser Heating Schemes," Proc. of the 1984 Int. Conf. on Plasma Physics, Lausanne, Switzerland, June-July 1984, I, 187.

D. W. Forslund, J. M. Kindel, W. B. Mori, C. Joshi, and J. M. Dawson, "Two-Dimensional Studies of Single Frequency and Beat Wave Laser-Plasma Heating," Phys. Rev. Letters 54, 558 (1985).

R. Bingham, W. B. Mori, and J. M. Dawson, "Some Nonlinear Processes Relevant to the Beat Wave Accelerator," in Laser Acceleration of Particles, ed. by C. Joshi and T. Katsouleas (Am. Inst. of Physics, NY, 1985) pp. 138-145.

T. Katsouleas, C. Joshi, J. M. Dawson, F. F. Chen, C. E. Clayton, W. B. Mori, C. Darrow, and D. Umstadter, "Plasma Accelerators," in Laser Acceleration of Particles, ed. by C. Joshi and T. Katsouleas (Am. Inst. of Physics, NY, 1985) pp. 63-98.

J. M. Kindel, D. W. Forslund, W. B. Mori, C. Joshi, and J. M. Dawson, "Two Dimensional Beat Wave Acceleration Simulations," Proc. of the Int. Conf. on Lasers '84, ed. by K. M. Corcoran, D. M. Sullivan, and W. C. Stwalley, pp. 462-465 (1985).

W. B. Mori, C. Joshi, J. M. Dawson, K. Lee, D. W. Forslund, and J. M. Kindel, "Studies of the Plasma Droplet Accelerator Scheme," IEEE Trans. on Nucl. Sci., NS-32, 3555 (1985).

W. B. Mori, "On Nonlinear Frequency Shifts in Beat Wave Excitation," Proc. of the CECAM Workshop on Interaction and Transport in Laser-Plasmas, Orsay, France (1985).

C. Darrow, D. Umstadter, T. Katsouleas, W. B. Mori, C. E. Clayton,

and C. Joshi, "Quasi-Resonant Mode Coupling in a Beat Excited Plasma," Phys. Rev. Lett 56, 2629 (1986).

C. Joshi, T. Katsouleas, C. E. Clayton, W. B. Mori, J. M. Kindel, and D. W. Forslund, "Experimental, Theoretical, and Computational Studies of the Plasma Beat Wave Accelerator at UCLA," Proc. of the Symposium on Adv. Accelerator Concepts, Madison, Wisconsin, August 21-27, 1986. To be published in the Am. Inst. of Physics Conference Proceedings Series.

T. Katsouleas, C. Joshi, and W. B. Mori, "Comment on 'Free-Electron Laser and Laser Electron Acceleration Based on the Megagauss Magnetic Fields in Laser-Produced Plasmas," Phys. Rev. Lett. 57. 1960 (1986).

W. B. Mori, "On Beat Wave Excitation of Relativistic Plasma Waves," IEEE Trans. on Plasma Science, special issue on Plasma-Based High-Energy Accelerators, ed. by T. Katsouleas (April 1987).

C. Darrow, W. B. Mori, T. Katsouleas, C. Joshi, D. Umstadter, and C. E. Clayton, "Electrostatic Mode Coupling of Beat Excited Electron Plasma Waves," IEEE Trans. on Plasma Science, special issue on Plasma-Based High-Energy Accelerators, ed. by T. Katsouleas (April 1987).

W. B. Mori, C. Joshi, J. M. Dawson, D. W. Forslund, and J. M. Kindel, "Two-Dimensional Simulations of Intense Laser Irradiation of Underdense Plasmas," Laser Interaction and Related Plasma Phenomena, Vol. 7, ed. by H. Hora and G. Miley (Plenum, New York, 1987).

W. B. Mori, C. Joshi, J. M. Dawson, D. W. Forslund, and J. M. Kindel, "Laser Beam Self-Focusing and Filamentation in a Plasma," Phys. Rev. Lett, in preparation.

W. B. Mori, C. Joshi, J. M. Dawson, T. Katsouleas, D. W. Forslund, and J. M. Kindel, "Computer Simulations of Beat Wave Excitation," Phys. Fluids, in preparation.

TABLE OF CONTENTS

	Page
List of Symbols	iv
Acknowledgements	viii
Vita and Publications	ix
Abstract	xvi
Chapter I. INTRODUCTION	1
PART A - BEAT WAVE EXCITATION	
Chapter II. THEORY	6
A. Introduction	6
B. Beat Wave Excitation	7
1. Model Equations	7
2. Growth and Saturation	12
a. Early Time Behavior	13
b. Late Time (Asymptotic) Behavior	14
3. Rise Time Effects	26
4. Phase Velocity Shift	34
5. Harmonics	37
6. Pump Depletion	41
7. Inhomogeneities	44
8. 2-D Effects	53
C. Summary	56
Chapter III. SIMULATIONS	59
A. Introduction	59

B. Results 61

1. Short Rise Time $\tau \leq t_s$ 61

2. Long Rise Time $\tau \geq t_s$ 73

3. $\Delta \neq 0$ 76

4. Density Gradient 81

5. Density Ripple 85

6. Discrete Ions 88

7. Two Dimensions 89

C. Summary 114

PART B - COMPETING INSTABILITIES

Chapter IV. DESCRIPTIONS OF COMPETING INSTABILITIES 118

A. Introduction 118

B. Growth Rates 120

1. Relativistic Instabilities 121

2. Ponderomotive Force Driven Instabilities of Electromagnetic Waves 131

a. SBS 131

b. SRS 135

c. Self-Focusing and Filamentation 138

3. Ponderomotive Force Driven Instabilities of Electrostatic Waves 140

a. Parametric Decay and Self-Modulation Simulations 141

CHAPTER V. SIMULATIONS OF COUPLING INSTABILITIES 144

A. Introduction 144

B. Electromagnetic Self-Focusing and Filamentation .. 145

1. Plane Waves 146

2. Finite Wave Fronts 152

3. Long Time Behavior 171

C. Ion Driven Instabilities 174

1. SBS 175

2. Parametric Decay 183

D. Summary and Conclusions 190

CHAPTER VI. SOME FINAL THOUGHTS 195

REFERENCES 198

APPENDIX A - ON NONLINEAR PLASMA FREQUENCY SHIFTS IN BEAT WAVE EXCITATION 202

APPENDIX B - EXCITATION OF PLASMA WAVES WITH $\Delta\omega = 2\omega_p$ ... 214

ABSTRACT OF THE DISSERTATION

Theory and Simulations of Beat Wave Excitation of Relativistic Plasma Waves

by

Warren Bicknell Mori

Doctor of Philosophy in Electrical Engineering

Professor Francis F. Chen, Co-Chair

Professor John M. Dawson, Co-Chair

Professor Chandrashekhar Joshi, Co-Chair

The generation of excitation of large amplitude plasma waves by the beating of two collinear laser beams is studied analytically and via computer experiments. When the difference (beat) frequency of the two lasers is near the natural frequency of the plasma, a large amplitude wave appropriate for accelerating particles to ultrahigh energies can be excited. The subject is divided into two parts. The first is the analysis of beat wave excitation (BWE) in the absence of competing processes. The second is the identification and the determination of the relative importance of the competing processes.

Beat wave excitation is studied analytically in the Eulerian fluid description for prescribed forms of the input light waves. The full set of the Maxwell and plasma fluid equations is reduced

perturbatively to a single cubic nonlinear equation. In the process, a controversy existing over the sign and magnitude of the nonlinear term is resolved. The consistency between the Eulerian and Lagrangian description is explicitly verified.

The implications of the reduced equation are studied. The subjects of saturation, phenomonological damping, phase velocity, pump rise time, harmonics, cascading, density inhomogeneities, and two-dimensional effects are briefly discussed analytically. The analytical results, whenever possible, are tested in computer experiments--both in one and two dimensions. It is found that for early enough times the simulations agree with the reduced cubic nonlinear equation rather accurately. The simulations illustrate the limitations of the theory.

The possible competing instabilities are investigated. Relativistic self-modulation and self-focusing of both plasma waves and light waves are discussed in more detail since they are less common in the literature. The other instabilities examined are Stimulated Brillouin Scatter, Stimulated Raman Scatter, and ponderomotive filamentation of the light waves; while ponderomotive self-modulation and parametric decay of the plasma wave are discussed. These competing processes and their importance to BWE are examined through computer experiments. It is found that strongly coupled parametric decay presents the most serious problem for BWE. The other instabilities occur, but their relative importance can be decreased when parameters relevant to particle accelerators are considered.

CHAPTER I - INTRODUCTION

Theoretical particle physicists continue to put forth new theories on the nature of and interaction between the smallest particles that compose our universe. These theories are based partly on existing experimental results and on conjecture. In order to test these conjectures, experimental high-energy physicists have had to collide various subatomic particles at increasingly higher energies. For now, accelerator technology has kept pace with this demand with remarkable success. Since the first cyclotrons of the 1930s, the maximum energy provided by accelerators has increased by nearly an order of magnitude per decade. This is displayed in what is referred to as the Livingston chart, and it is presented in Fig. 1.

The maximum accelerating gradient provided by present-day accelerators is 20 $\frac{\text{MeV}}{\text{m}}$.[1] Using this gradient, the largest accelerators provide 1 TeV protons and 50 GeV electrons. To do so, these machines have become extremely large and expensive. If the present-day technology is continued to be used. then future accelerators will have to be even larger and more expensive. For example, the proposed SSC (super conducting super collider) will be 90 km in circumference and cost an estimated $4.4 billion.[2] Eventually, either new technologies that provide larger gradients or cheaper real estate need to be found.

One of the limitations of conventional technology is that the

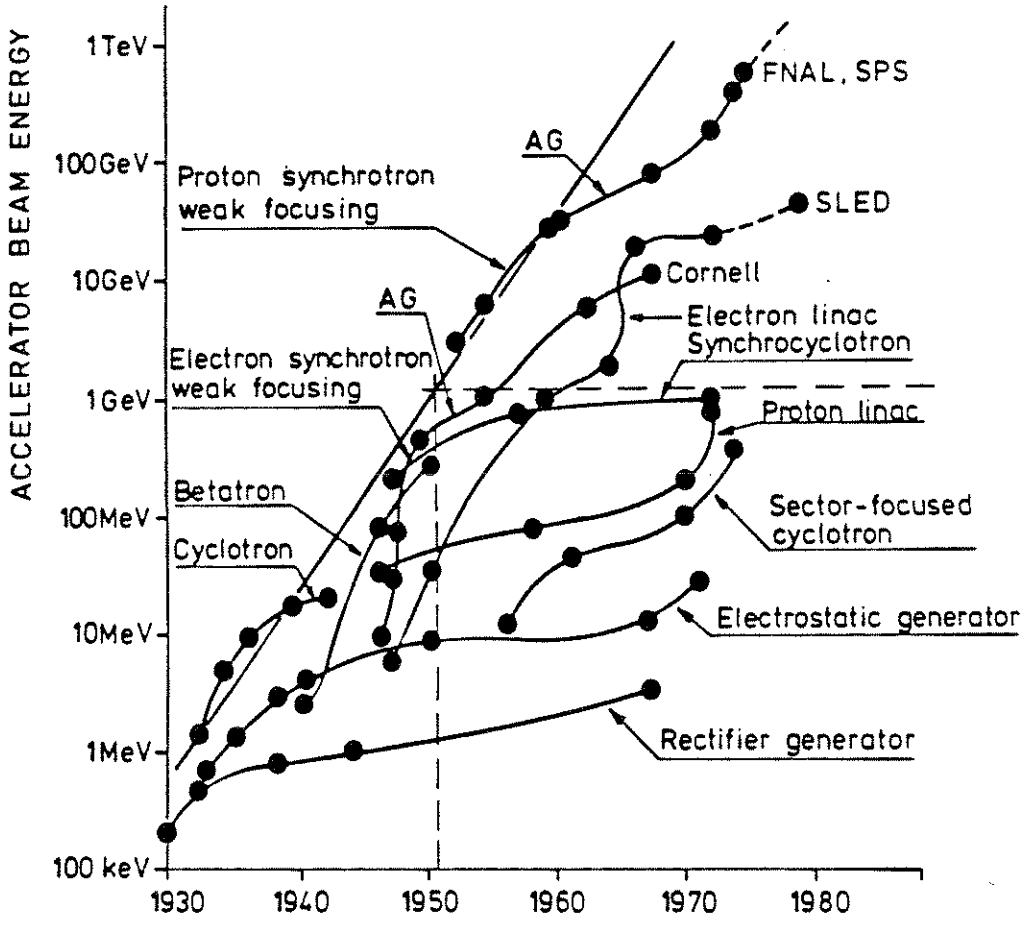

Figure 1. The Livingston chart: progress in high energy accelerators.

walls of the accelerator break down for large fields. A plasma cannot break down as it is already ionized and, thus, can support much larger fields. If these fields can be formed into a coherent longitudinal wave, then they can accelerate particles. When the phase velocity of the wave is close to the speed of light, then the final energy of the accelerated particles can be quite high.

With the advent of high-power lasers, researchers have attempted to find ways of utilizing large electric fields of the lasers directly to accelerate particles. In vacuum, this has to date been fruitless. On the other hand, laser acceleration in magnetic fields[3] or in gases with indexes of refraction greater than unity[4] have already been shown to hold promise.

It was recently suggested that high-intensity lasers could be used to excite a plasma wave. The idea was to use two collinear lasers with a frequency separation equal to the background plasma frequency. The beating pattern of the two laser beams through nonlinear interactions with the plasma provides a force called the ponderomotive force. This force bunches the electrons at the spacing of the beating pattern and they oscillate at the beat frequency. If the beat frequency matches the resonant plasma frequency, the plasma wave is resonantly excited. This scheme[5,6,7] has been labeled the Plasma Beat Wave Accelerator (PBWA). It is common to both the subjects of laser accelerators and plasma accelerators.

It is straightforwardly shown[6] that the energy obtained from an electrostatic wave with a scalar potential of the form

$$\frac{e\phi}{mc^2} = e_o \sin \omega_p\left(t - \frac{x}{v_\phi}\right)$$

is $4e_o\gamma_\phi^2\ mc^2$ and it is acquired in a distance $2\pi\gamma_\phi^2\frac{c}{\omega_p}$ if $\gamma_\phi >> 1$. We define $\gamma_\phi = \left(1 - \frac{v_\phi^2}{c^2}\right)^{-1/2}$ and $\omega_p = \left(\frac{4\pi e^2 \bar{n}_o}{m}\right)^{1/2}$ where $\bar{n}_o$ is the plasma density. Therefore, the values of e_o and γ_ϕ are the parameters that determine the promise of an accelerator based on a plasma wave. Note that the value of the electric field corresponding to such a scalar potential is $\sim e_o\sqrt{n_o}\left(\frac{V}{cm}\right)$ where n_o is in units of cm^{-3}. For a plasma density of 10^{16}, this gives an accelerating gradient of $e_o 10^4\left(\frac{MeV}{m}\right)$, which is 500 times larger than current accelerators provide (e_o is generally smaller than unity).

In order to determine the promise of the PBWA, it is necessary to characterize the properties of a plasma wave excited from beat wave excitation (BWE). Previous work has shown that e_o is a function of laser intensity,[8,9] while γ_ϕ is equal to the ratio of the laser frequency to the plasma frequency.[7] In this dissertation the properties of e_o and γ_ϕ are investigated further. In Part A, BWE is addressed in the absence of competing instabilities but including such effects as damping, laser rise time, and inhomogeneities. In Chapter II, the properties of e_o and γ_ϕ are studied analytically. The limitations of the analytic work are examined via computer simulations in Chapter III. In Part B, the role of competing instabilities is discussed. Chapter IV is devoted to identifying which instabilities are believed to be important. In Chapter V, the relevance of the competing instabilities is deter-

mined from computer simulations. The implications of the simulations to an eventual accelerator are summarized in Chapter VI.

We mention that although this work has been motivated by the interest in PBWA, it is also intended to illustrate the multitude of basic plasma physics phenomena that arise in intense irradiation of underdense plasmas. In this spirit, some phenomena that occur well after any plasma wave is discernible are mentioned.

PART A. ON BEAT EXCITATION OF RELATIVISTIC PLASMA WAVES

CHAPTER II. THEORY

IIA. Introduction

The subject of charged particle acceleration by longitudinal waves in plasmas has received considerable attention during the previous 10 years. This has been particularly true in the fields of laser fusion coronal physics[10,11,12,13] and beat wave acceleration.[5,6,7,14,15,16] With few exceptions, the early work was concerned with plasma waves whose phase velocities (v_ϕ) were small enough when compared to the speed of light (c) so that the relativistic factor associated with the phase velocity $\gamma_\phi \equiv [1 - (v_\phi^2/c^2)]^{-1/2}$ was close to unity.[10,11,12,13] Recently interest has shifted to the opposite situation where $\gamma_\phi >> 1$.[5,6,7,8,14] Electrons trapped in plasma waves with this property can acquire enormous amounts of energy; and if the electric field of the plasma wave is large then these enormous energies can be acquired in remarkably short distances--distances so short, in fact, that such plasma waves have been suggested as the basis for future high energy accelerators. In this dissertation we concern ourselves primarily with the high γ_ϕ limit with the accelerator application in mind.

There are two mechanisms presently being seriously considered to excite the plasma wave. In one, a relativistic bunch of elec-

trons is injected into the plasma, resulting in a "wake field" behind the bunch with a v_ϕ equal to the velocity of the bunch.[17] This scheme will not be discussed in this dissertation, although the issues concerning the stability of large amplitude plasma waves are identical to those in the second scheme. In the second, two collinear laser beams whose frequency difference equals the plasma frequency, resonantly drive up a plasma wave with a phase velocity approximately equal to the group velocity of light in a plasma.[5,6,7] When this mechanism is used as the driver, the acceleration scheme called, for obvious reasons, the plasma beat wave accelereator (PBWA).

In Sec. IIB we start from Maxwells equations and the Eulerian equation of motion, assuming two input light waves. The resulting envelope equations are reviewed and the magnitude and sign of the nonlinear frequency shift is examined in Appendix A. We then focus on issues concerning the PBWA. In Sec. IIC the results of Chapter II are summarized.

IIB. Beat Wave Excitation

IIB1. Model Equations

During the past 20 years the process of resonantly exciting plasma waves from two electromagnetic waves whose frequency difference matches the plasma frequency has been proposed as a means to (1) diagnose the plasma density,[18] (2) heat a plasma,[8,19] (3) generate current in a "Tokamak,"[20] (4) study the ionosphere,[21] and (5) accelerate electrons to ultra high energies.[5,6,7,14] In this

dissertation we present theory emphasizing the last application. The Eulerian fluid equations are used as the starting point to study the problem analytically. The early work on beat excitation used the Lagrangian fluid equations.[8,9] Recent work, however, has used the Eulerian fluid equations and this has led to a discrepancy in the literature.[22,23,24] This is resolved in Appendix A,[25,26] Furthermore, the use of Eulerian coordinates permits straightforward transitions to the study of the stability of transverse waves.

In the cold plasma limit the starting equations are the relativistic equations of motion for electrons without the pressure term, the continuity equation, and Maxwells equations:

$$\frac{d}{dt}\vec{p} = \left(\frac{\partial}{\partial t} + \vec{v}\cdot\nabla\right)\vec{p} = -e\left(\vec{E} + \frac{\vec{v}\times\vec{B}}{c}\right) \tag{1}$$

$$\frac{\partial N}{\partial t} + \nabla\cdot N\vec{v} = 0 \quad (N \equiv \bar{n}_o + n) \tag{2}$$

$$\nabla\times\vec{B} = \frac{4\pi}{c}\vec{j} + \frac{1}{c}\frac{\partial\vec{E}}{\partial t} \tag{3}$$

$$-\nabla\times\vec{E} = \frac{1}{c}\frac{\partial\vec{B}}{\partial t} \tag{4}$$

$$\nabla\cdot\vec{E} = 4\pi\rho = -4\pi en. \tag{5}$$

Combining Eqs. (3) and (4) in the usual way gives

$$\left(-\nabla\times\nabla\times - \frac{1}{c^2}\frac{\partial^2}{\partial t^2}\right)\vec{E} = \frac{4\pi}{c^2}\frac{\partial}{\partial t}\vec{j} = \frac{4\pi}{c^2}\frac{\partial}{\partial t}(-eNv). \tag{6}$$

We define $N \equiv \bar{n}_o + n$ where $\bar{n}_o$, the background density, is not a function of time.

It follows then that Eq. (6) becomes

$$\left(\nabla^2 - \frac{1}{c^2}\frac{\partial^2}{\partial t^2} - \nabla\nabla\cdot\right)\vec{E} = -\frac{4\pi e}{c^2}\left(\bar{n}_o\cdot\frac{\partial}{\partial t}\vec{v} + \frac{\partial}{\partial t}n\vec{v}\right) \tag{7}$$

An equation for $\frac{\partial\vec{v}}{\partial t}$ can be obtained from Eq. (1) by noting that

$$\frac{d}{dt}\vec{p} = \frac{d}{dt}\gamma\vec{v} = \gamma^3\left[\left(1 - \frac{v^2}{c^2}\right)\overleftrightarrow{I} + \frac{\vec{v}\vec{v}}{c^2}\right]\cdot\frac{d\vec{v}}{dt} = -\frac{e}{m}\left(\vec{E} + \frac{\vec{v}\times\vec{B}}{c}\right) \tag{8}$$

where $\overleftrightarrow{I}$ is the unit dyadic. Inverting the dyadic leads to

$$\frac{d\vec{v}}{dt} = -\frac{e}{\gamma m}\left(\overleftrightarrow{I} - \frac{\vec{v}\vec{v}}{c^2}\right)\cdot\left(\vec{E} + \frac{\vec{v}\times\vec{B}}{c}\right) \tag{9}$$

Consequently,

$$\frac{\partial\vec{v}}{\partial t} = -\vec{v}\cdot\nabla\vec{v} - \frac{e}{\gamma m}\left(\overleftrightarrow{I} - \frac{\vec{v}\vec{v}}{c^2}\right)\cdot\left(\vec{E} + \frac{\vec{v}\times\vec{B}}{c}\right) \tag{10}$$

Substituting Eq. (10) into Eq. (7) gives

$$\left(\nabla^2 - \frac{1}{c^2}\frac{\partial^2}{\partial t^2} - \nabla\nabla\cdot\right)\vec{E} = -\frac{4\pi e}{c^2}\left\{\frac{\partial}{\partial t}n\vec{v} - \bar{n}_o\vec{v}\cdot\nabla\vec{v} - \frac{\bar{n}_o e}{m\gamma}\left(\overleftrightarrow{I} - \frac{\vec{v}\vec{v}}{c^2}\right)\cdot\left(\vec{E} + \frac{\vec{v}\times\vec{B}}{c}\right)\right\} \tag{11}$$

We expand γ to lowest order $\gamma \simeq \left(1 + \frac{1}{2}\frac{v^2}{c^2}\right)$ and collect the linear

terms on the left-hand side, resulting in

$$\left(\nabla^2 - \frac{1}{c^2}\frac{\partial^2}{\partial t^2} - \frac{\omega_p^2}{c^2} + \nabla\nabla\cdot\right)\vec{E} = -\frac{4\pi e}{c^2}\left\{\frac{\partial}{\partial t}\left(n\vec{v}\right) - \bar{n}_o\vec{v}\cdot\nabla\vec{v}\right.$$

$$-\frac{\bar{n}_o e}{m}\left(-\frac{1}{2}\frac{v^2}{c^2}\overleftrightarrow{I} - \frac{\vec{v}\vec{v}}{c^2}\right)\cdot\vec{E}$$

$$\left.-\frac{\bar{n}_o e}{m}\left(1 - \frac{1}{2}\frac{v^2}{c^2}\right)\frac{\vec{v}\times\vec{B}}{c}\right\} \qquad (12)$$

where the fact that $\vec{v}\vec{v}\cdot\frac{v\times B}{c} = 0$ was used. The $\frac{v^2}{c^2} << 1$ approximation is valid for many situations of interest. If needed, more terms in the expression can be kept, although what is outlined below would become algebraically more complicated.

Equation (12) describes both the longitudinal and transverse waves. In this dissertation we concentrate on the evolution of the longitudinal wave. We assume that the wave is being driven by linearly polarized transverse waves of the form $\hat{y}B_{io}\sin(\kappa_i x - \omega_i t)$, where $i = 1,2$ and $\omega_1 - \omega_2 \equiv \omega_o$. The equation for E_x reduces to

$$\left(\frac{\partial^2}{\partial t^2} + \omega_p^2\left(1 - \frac{3}{2}\epsilon^2\frac{v_x^2}{c^2} - \frac{1}{2}\epsilon^2\frac{v_z^2}{c^2}\right)\right)E_x = \epsilon 4\pi e\left\{\frac{\partial}{\partial t}nv_x - \bar{n}_o\vec{v}\cdot\nabla v_x\right.$$

$$\left.+\epsilon\frac{\bar{n}_o e}{m}\frac{v_x v_z}{c^2}E_z - \frac{\bar{n}_o e}{m}\left(\frac{\vec{v}\times\vec{B}}{c}\right)x\right\} \qquad (13)$$

where ϵ is simply a small parameter used for bookkeeping purposes (later to be set equal to unity).

To solve Eq. (13), the formalism of Krylov-Bogoliubov-

Mitropolsky[27,28] was employed. The dynamical variables (E_x, V_x, V_z, n) are assumed to be of the form

$$e = e_o \cos \psi + \sum \varepsilon^i e_i(e_o,\psi) \tag{14}$$

The quantities e_o and ψ evolve according to

$$\frac{\partial e_o}{\partial t} = \varepsilon A_1(e_o,\psi) + \varepsilon^2 A_2(e_o,\psi) + \ldots \tag{15}$$

$$\frac{\partial e_o}{\partial x} = \varepsilon D_1(e_o,\psi) + \varepsilon^2 D_2(e_o,\psi) + \ldots \tag{16}$$

$$\frac{\partial \psi}{\partial t} = -\omega_p + \varepsilon B_1(e_o,\psi) + \ldots \tag{17}$$

$$\frac{\partial \psi}{\partial x} = -\kappa_o + \varepsilon C_1(e_o,\psi) + \ldots \tag{18}$$

The functions A_i, B_i, C_i, and D_i are chosen so that e_o does not grow secularly in time. In addition, we assume $\nabla \to \partial/\partial x$, i.e., we have a one-dimensional system.

After some straightforward algebra, given in Appendix A, the following equation is obtained:

$$\left\{\frac{\partial^2}{\partial t^2} + 2\gamma\frac{\partial}{\partial t} + \omega_p^2\left(1 - \frac{3}{8}\frac{v_\phi^2}{c^2}|e_o|^2 - \frac{1}{4}(\alpha_1^2 + \alpha_2^2)\right)e_o e^{i\psi}\right\}$$

$$= \frac{c}{v_\phi}\frac{\alpha_1\alpha_2}{2}\omega_p^2 e^{i\psi_o} \equiv F_{NL}e^{i\psi_o} \tag{19}$$

where $e_o \equiv \frac{eEx}{mc\omega_p}$ is the normalized longitudinal field amplitude,

$\alpha_i \equiv \frac{eE_i}{mc\omega_i}$ is the normalized field of a laser, γ is a phenomenological damping term, and $\psi_o \equiv (\kappa_o x - \omega_o t)$. The full derivation and its subtleties along with a brief history is given in Appendix A.

We note that the $\epsilon^2 V_x V_z E_z$ term on the right-hand side of Eq. (13) is exactly canceled by the $\epsilon^2 V_{z1} V_{z2} E_x$ term on the left-hand side of Eq. (13) when $\omega_o = \omega_p$. These terms do not cancel but contribute to an instability when $\omega_o = 2\omega_p$. This instability was first reported by Rosenbluth and Liu.[8] However, their growth rate is incorrect by a factor of 5/4 since they neglected the two previously mentioned terms. The complete details are given in Appendix B where the driving term for the growth rate is derived in both Eulerian and Lagrangian coordinates.

IIB2. Growth and Saturation

In this section, as was done previously by others,[8,9,22] Eq. (19) is reduced to two coupled ordinary first-order nonlinear differential equations. We note that these are simply Eqs. (15) and (17). Although the details are not shown, they result from the perturbation expansion given in Appendix A. However, we will obtain Eqs. (15) and (17) from (19) to be more illustrative. To begin, we define $\psi = \psi_o + \phi$ and neglect for the time being the α_j's on the left-hand side of Eq. (19) to obtain

$$-2i\omega_o(\dot{e}_o + i\dot{\phi}e_o) - 2i\gamma\omega_o e_o + (\omega_p^2 - \omega_o^2)e_o - \frac{3}{8}\omega_p^2 \frac{v_\phi^2}{c^2} e_o^3 = F_o e^{-i\phi} \tag{20}$$

where second-order derivatives of the slowly varying e_o and ϕ are

neglected. Separating out the imaginary and real parts gives

$$2\omega_o \dot{e}_o = F_o \sin\phi + 2\gamma\omega_o e_o \tag{21}$$

$$2\omega_o e_o \dot{\phi} = (\omega_\delta^2 - \omega_p^2) e_o + \frac{3}{8}\omega_p^2 \frac{v_\phi^2}{c^2} e_\delta^3 + F_o \cos\phi \tag{22}$$

which reduces to

$$\dot{e}_o = F \sin\phi - \gamma e_o \tag{23}$$

$$e_o \dot{\phi} = \Delta e_o + C e_o^3 + F \cos\phi \tag{24}$$

where $F \equiv \frac{\alpha_1 \alpha_2 \omega_o}{4}$, $C \equiv \frac{3}{16}\frac{\omega_p^2}{\omega_\delta^2}\frac{v_\phi^2}{c^2}\omega_o$, and $\Delta \equiv \frac{\omega_\delta^2 - \omega_p^2}{2\omega_\delta^2}\omega_o$. The problem of plasma wave growth is, therefore, reduced to two coupled equations in e_o, the plasma wave amplitude, and ϕ, the phase difference between the driving lasers and the plasma wave. The growth depends on the normalized laser intensity F, the damping γ, and Δ, the initial mismatch between the beat frequency ω_o and the plasma frequency ω_p.

IIB2a. Early Time Behavior

By early time it is meant that damping has not yet played a role. This is true crudely for times less than a few $1/\gamma$. First we note that if $e_o = 0$ at $t = 0$, then $\cos\phi \to 0$ instantaneously and $\dot{e}_o = F$. The initial growth is therefore linear in time as is well known. In addition, as shown by Tang et al.[9] a constant of the

motion exists when damping is negligible and F is not a function of time and it is

$$K = e_o \cos \phi + \frac{1}{F}\left(\frac{Ce_o^4}{4} + \frac{\Delta e_o^2}{2}\right) \tag{25}$$

When $e_o = 0$ at $t = 0$, Eq. (25) becomes

$$\left(F \cos \phi + \frac{Ce_o^3}{4} + \frac{\Delta e_o}{2}\right) = 0 \tag{26a}$$

and substituting Eq. (26a) into Eq. (24) gives

$$\dot{\phi} = \frac{\Delta}{2} + \frac{3}{4} Ce_o^2. \tag{26b}$$

The maximum e_o occurs when $\dot{e}_o = 0$, i.e., when $\sin \phi = 0$. Therefore, the maximum $e_o \equiv e_m$ is found by solving Eq. (23) for $\cos \phi = -1$

$$\frac{Ce_m^3}{4} + \frac{\Delta e_m}{2} - F = 0 \tag{27}$$

When the beat frequency of the lasers is ω_p ($\Delta = 0$), Eq. (27) gives

$$e_m = \left(\frac{4F}{C}\right)^{1/3} \tag{28}$$

which is the result of Rosenbluth and Liu.[8] Furthermore, Tang et al.[9] have shown that as a function of Δ the maximum e_m is

$$e_m = \left(\frac{16\ F}{C}\right)^{1/3} \tag{29a}$$

and it occurs when

$$\Delta = -\left(\frac{27}{2}\ CF^2\right)^{1/3} \tag{29b}$$

For reference, we provide an expression obtained via a Taylor expansion for e_m as a function of Δ, for $\Delta > -\left(\frac{27}{2}\ F^2C\right)^{1/3}$

$$e_m \simeq \left(\frac{4F}{C}\right)^{1/3} - \left(\frac{2}{27}\ \frac{\Delta^3}{F^2C}\right)^{1/3} \tag{30}$$

Equation (27) in general has three roots, all of which are not necessarily real. Importantly, and perhaps not surprisingly, Tang et al.[9] numerically found that the physically relevant solution is the smallest one, when $e_o = 0$ at $t = 0$. McKinstrie and Forslund[26] have recently shown this to be true on analytical grounds. As a consequence, a discontinuity exists in the solution of Eq. (27) when Eq. (29b) is satisfied. To be more specific, when

$$\Delta < -\left(\frac{27}{2}\ CF^2\right)^{1/3} \tag{31}$$

the solution for e_m is on another branch of the solution to Eq. (26a) for which

$$e_m = \left(\frac{2F}{C}\right)^{1/3} \tag{32}$$

when Eq. (29a) is satisfied. The reason that a small negative frequency mismatch results in a larger peak amplitude is that it helps to compensate for the relativistic frequency shift, which is also in the negative direction. This fact is discussed in the previous work[9,22] so no further discussion will be given.

Throughout, we have referred to e_m as the peak amplitude rather than the amplitude at saturation. We do this because Eqs. (23) and (24) show that although $\dot{e}_o = 0$ at e_m, $\dot{\phi} \neq 0$ concomitantly. Therefore, $e_o = e_m$ only for an instant. The fixed point (a center) $\dot{e}_o = 0$ and $\dot{\phi} = 0$ is only approached with the inclusion of some form of dissipation, and this will be discussed next.

IIB2b. Late Time (Asymptotic Behavior)

The previous section addressed the so-called early time behavior. In this section we investigate what effect dissipation has on the asymptotic plasma wave amplitude. This issue was first investigated by Lee et al.[29] without the inclusion of a frequency mismatch. It was found that for times much larger than a damping time the plasma wave asymptotically approaches an amplitude, a factor $4^{1/3}$ smaller than the Rosenbluth and Liu[8] peak amplitude. The importance of collisional damping has already been found to be important in some recent experiments.[30] In this section we allow for a frequency mismatch and we investigate how the asymptotic amplitude is approached in time. It is important to know whether it is approached in a monotonic or oscillatory manner.

It is well-known that the qualitative properties of the asymp-

totic solution to a system of two coupled ordinary differential equations of two functions (f_1, f_2)

$$\dot{f}_1 = \phi_1(f_1, f_2); \; \dot{f}_2 = \phi_2(f_1, f_2) \tag{33}$$

can be obtained by studying the behavior of f_1 and f_2 near the fixed points, i.e., points where

$$\dot{f}_1 = \dot{f}_2 = 0. \tag{34}$$

We begin, therefore, by identifying the fixed points. The starting set of equations are

$$\dot{e}_o = F \sin \phi - \gamma e_o \tag{35}$$

$$e_o\dot{\phi} = \Delta e_o + C e_o^3 + F \cos \phi \tag{36}$$

It follows then that the fixed points (e_f, ϕ_f) are defined by the equations

$$F \sin \phi_f - \gamma e_f = 0 \tag{37}$$

$$\Delta e_f + C e_f^2 + F \cos \phi_f = 0 \tag{38}$$

Substituting the expression for cos ϕ_f obtained from Eq. (37),

$$\cos \phi_f = (1 - \sin^2 \phi_f)^{1/2} = \left\{1 - \left(\frac{\gamma e_f}{F}\right)^2\right\}^{1/2}$$

into Eq. (38) gives

$$\Delta e_f + C e_f^3 + F\left[1 - \left(\frac{\gamma e_f}{F}\right)^2\right]^{1/2} = 0 \tag{39}$$

This can easily be rewritten to give

$$e_f^6 + \frac{2\Delta}{C} e_f^4 + \frac{1}{C^2}(\Delta^2 + \gamma^2) e_f^2 - \frac{F^2}{C^2} = 0. \tag{40}$$

Since Eq. (40) is a cubic equation in e_f^2, we need to determine the stability of the three fixed points and whether the stable fixed points are nodes or spiral points.[31] To determine this we expand Eqs. (35) and (36) about $(e_f, \sin \phi_f)$. We let $\sin \phi \equiv y$ and substitute into Eqs. (35) and (36) the definitions

$$e_o = e_f + \delta e \quad \text{and} \quad y = y_f + \delta y \tag{41}$$

to obtain

$$\dot{\delta e} = -\gamma \delta e + F \delta y + O(\delta y^2, \delta e^2, \delta y \delta e) \tag{42}$$

$$\dot{\delta y} = -\frac{1}{F}(3Ce_f^2 + \Delta)(Ce_f^2 + \Delta) - \gamma \delta y + O(\delta y^2, \delta e^2, \delta y \delta e) \tag{43}$$

where e_f and y_f are obtained from Eqs. (37) and (38)

We rewrite Eqs. (42) and (43) in matrix notation to find

$$\frac{d}{dt}\begin{bmatrix}\delta e\\ \delta y\end{bmatrix} = \begin{bmatrix}-\gamma & F\\ -\frac{1}{F}(3Ce_f^2 + \Delta)(Ce_f^2 + \Delta & -\gamma\end{bmatrix}\begin{bmatrix}\delta e\\ \delta y\end{bmatrix} \qquad (44)$$

The stability of the fixed points is determined from the eigenvalues λ of the matrix in Eq. (44). The eiginvalues are given by

$$(\lambda + \gamma)^2 + (3Ce_f^2 + \Delta)(Ce_f^2 + \Delta) = 0 \qquad (45)$$

or

$$\lambda = -\gamma \pm \left(-(3Ce_f^2 + \Delta)(Ce_f^2 + \Delta)\right)^{1/2} \qquad (46)$$

If the discriminant of Eq. (46) is positive and greater than γ^2 for some e_f and Δ, then that particular fixed point is a saddle point and essentially unstable.

To recapitulate, Eq. (40) can be used to determine e_f of the fixed point and Eq. (37) can then be used to determine the corresponding ϕ_f (or y_f). The stability and type of fixed point can be determined from Eq. (46). Although general expressions for the e_f's as as functions of Δ and γ are possible, since Eq. (40) is a cubic equation for e_f^2, they are so cumbersome as to be rendered useless. Consequently, we investigate the relevant e_f's, Δ's, and γ's in various limits.

$\underline{\Delta = 0}$

When the mismatch is zero the solution to Eq. (40) can be

written down formally as[24,27]

$$e_f = \left\{\left[\frac{F^2}{2C^2} + \left(\frac{\gamma^6}{27C^6} + \frac{F^4}{4C^4}\right)^{1/2}\right]^{1/3} + \left[\frac{F^2}{2C^2} - \left(\frac{\gamma^6}{27C^6} + \frac{F^4}{4C^6}\right)^{1/2}\right]^{1/3}\right\} \tag{47}$$

This expression was first given by Lee et al.[29] [Note that for $\Delta = 0$ there is only one real root to Eq. (40).] The behavior for e_f can be crudely separated into two regimes by the parameter γ. For small values of γ, i.e., when

$$\frac{\gamma^6}{27C^6} << \frac{F^4}{4C^4} \quad \text{or} \quad \gamma << \left(F^2C\right)^{1/3} \tag{48}$$

we find from Eq. (47) that

$$e_f \simeq \left(\frac{F}{C}\right)^{1/3}, \tag{49}$$

which could also be obtained simply from Eqs. (37) and (38) or (40) in the $\Delta = 0$ and $\gamma = 0$ limit. Consequently, as already stated, e_f is a factor $4^{1/3}$ smaller than e_m. We emphasize, however, that the actual solution to e_o in the $\Delta = \gamma = 0$ limit follows the Rosenbluth and Liu behavior until $t \sim 1/\gamma$, at which time it approaches the asymptotic value e_f.

To see this, note that Eq. (46) gives for the eigenfrequency

$$\lambda = -\gamma \pm i\,(3\,(CF^2)^{1/3})^{1/2} \tag{50}$$

where $e_f = \left(\frac{F}{C}\right)^{1/3}$ was used. (When $\Delta = 0$, λ is always complex

since the discriminant is always negative.) Estimating the time to saturation as $\frac{\pi}{\mathrm{Im}\lambda}$ gives $t_s = 1.8(F^2C)^{-1/3}$, which is an excellent estimate to the actual value of $\sim 1.2(4)^{1/3}(F^2C)^{-1/3}$.[9] Since $\mathrm{Im}\lambda >> \mathrm{Re}\lambda(=-\gamma)$, then the trajectory in phase space spirals around the fixed point many times before it approaches it.

For large values of γ when

$$\gamma >> \left(F^2C\right)^{1/3} \tag{51}$$

Eq. (47) reduces to

$$e_f \simeq \left(\frac{F}{\gamma}\right)^2 \tag{52}$$

This is just the answer obtained when the nonlinear frequency shift is neglected. As in the small γ limit, Eq. (52) could also be obtained from Eqs. (37) and (38) or from Eq. (40).

$\underline{\Delta \neq 0}$

When $\Delta \neq 0$ there is the possibility that three real roots exist. The condition for this will be discussed shortly. Furthermore, two of these solutions are stable while the third is unstable. The unstable root is always the middle one.[27] In what follows we explore the γ, Δ parameter space to determine the salient values for damping and mismatch.

For convenience, Eq. (40) is rewritten in normalized variables

$$\bar{e}_f^6 + \frac{3}{2}\bar{\Delta}\,\bar{e}_f^4 + \frac{9}{16}\left(\bar{\Delta}^2 + \bar{\gamma}^2\right)\bar{e}_f^2 - \frac{1}{16} = 0 \qquad (53)$$

where

$$e_f = \bar{e}_f\left(\frac{4F}{C}\right)^{1/3}, \quad \Delta = \left(\frac{27}{4}F^2C\right)^{1/3}\bar{\Delta}, \quad \text{and} \quad \gamma = \left(\frac{27}{4}F^2C\right)^{1/3}\bar{\gamma}\ .$$

Since Eq. (53) is a cubic equation in $\bar{e}_f^2$, then the condition that three real roots exist (if $\bar{e}_f^2$ is always positive) is easily obtained as[32]

$$\bar{\gamma}^6 + 2\bar{\Delta}^2\bar{\gamma}^4 + (\bar{\Delta}^4 + \frac{4}{3}\bar{\Delta})\bar{\gamma}^2 + \frac{4}{27}(1 + \bar{\Delta}^3) \leq 0 \qquad (54)$$

For a fixed $\bar{\gamma}$, Inequality (54) is satisfied neither for positive Δ nor for any $-\infty < \bar{\Delta} < \bar{\Delta}_m$ (except for $\bar{\gamma} \to 0$ when Inequality (54) is satisfied for all $\bar{\Delta} < -1$). Additionally, for real $\bar{\gamma}$, Eq. (54) with the equality is only satisfied for two real Δ's.[33] Therefore, three real solutions for $\bar{e}_f^2$ only exist between these $\bar{\Delta}$'s. This is illustrated in Figs. 2a and 2b where the solutions to Eqs. (53) and (54) are plotted. The plot in Fig. 2a is the well-known tuning curve for a cubic nonlinear oscillator.[27] The inequality given by Eq. (54) is equivalent[33] to using Eq. (53) and the condition $d\bar{e}_f^2/d\bar{\Delta} = \infty$,

$$\bar{e}_f^4 + 2\bar{\Delta}\bar{e}_f^2 + \frac{3}{16}(\bar{\Delta}^2 + \bar{\gamma}^2) = 0 \qquad (55)$$

The requirement that the eigenvalue λ be 0 is identical to Eq.

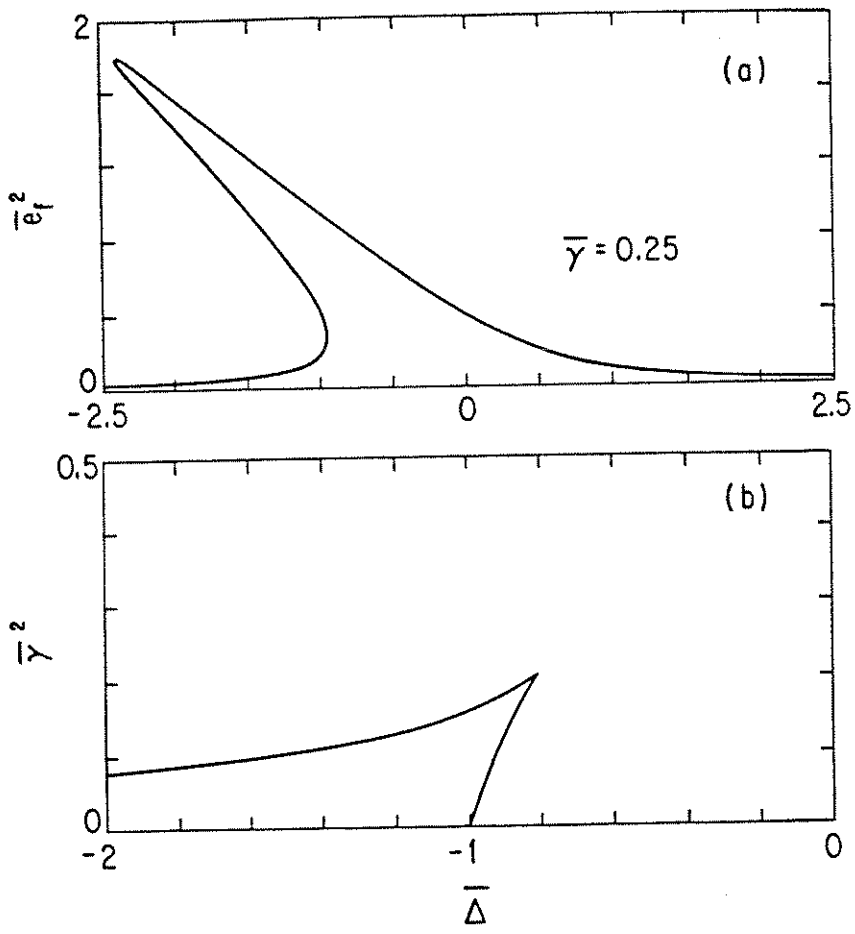

Figure 2. In (a) we plot the real solutions to Eq. (53) for $\bar{\gamma}$ = .25 and (b) we plot real solutions to Equality (54).

(55). This is due to the fact that an unstable root only exists when three solutions exist, so the threshold conditions are identical.

It is clear from Fig. 2b that at most two solutions satisfy the equality given by (54). Furthermore, as the normalized damping increases, eventually Inequality (54) cannot be satisfied for any $\bar{\Delta}$. This value of $\bar{\gamma}^2$ can be analytically determined from the condition that the discriminant, when solving for $\bar{e}_f^2$, of the solution to Eq. (55) vanishes.[33] This gives

$$\bar{\Delta}^2 = 3\bar{\gamma}^2 \quad \text{and} \quad \bar{e}_f^2 = -\frac{\bar{\Delta}}{2} .$$

Substituting these expressions back into Eq. (55) gives $\bar{\gamma} = .458$.

The maximum value of $\bar{e}_f$ for a particular $\bar{\gamma}$ is also easily determined. From Eq. (37), $e_f = \frac{F}{\bar{\gamma}} \sin \phi_f$, so the maximum e_f is $\frac{F}{\bar{\gamma}}$ and from Eq. (38) this occurs for $\Delta = -\frac{CF^2}{\gamma^2}$. In normalized units these are $\bar{e}_f = \frac{1}{3\bar{\gamma}}$ and $\bar{\Delta} = -\frac{4}{27}\bar{\gamma}^2$. These could also be obtained from the condition that $d\bar{e}_f^2/d\bar{\Delta} = 0$.[33] We note that in general $\bar{\Delta} = -4/27\ \bar{\gamma}^2$ is close to the most negative $\bar{\Delta}$ that satisfies Eq. (54).

When only one solution exists for $\bar{e}_f$, no confusion arises as to the asymptotic evolution since for this case the fixed point is unique and stable. However, when three solutions exist with two being stable, it is not obvious a priori which stable fixed point is approached for a given initial condition. To solve this problem we need to determine the basin of attraction[34] for each fixed point as functions of Δ and γ. However, we are interested in the partic-

ular initial condition $e_o(0) \simeq 0$. For this case we present arguments, which have been checked in a limited fashion numerically, that rely on the work of Tang et al.[9] They obtained, as discussed earlier, in the absence of damping, the maximum value of e_o as a function of time (e_m) for the initial condition $e_o(0) = 0$. If damping is included, it seems reasonable to assume that e_m should still be an upper bound. Therefore, for a given Δ and γ, if a stable fixed point e_f exists such that $e_f > e_m$, then it is not accessible when $e_o(0) = 0$. Therefore, the mismatch $\Delta = \left(-\frac{27}{2}F^2C\right)^{1/3}$ or $\bar{\Delta} = -2^{1/3}$ is still a significant Δ. It can be shown that the largest Δ for which Eq. (54) is satisfied is always larger than $\bar{\Delta} = -1$, which is larger than $-2^{1/3}$. Hence, there is a region in Δ space where two stable points exist with smaller amplitudes than e_m. For these situations we have not, as yet, determined the basins of attraction as parameterized by Δ and γ.

Qualitatively though, the inclusion of damping can be thought of as decreasing the mismatch (making it more negative). This can be seen from Eqs. (37) and (38). In Eq. (37) the negative mismatch negates the positive cubic nonlinearity allowing the driver and the plasma wave to remain in phase longer. However, as shown by Tang et al.[9] if the mismatch becomes too negative ($\bar{\Delta} < -2^{1/3}$) then $\dot{\phi}$ is initially so large that F sin ϕ decreases rapidly enough to prevent Ce_o^2 from ever becoming larger than Δ. When damping is present then e_o will increase at a slower rate for a given Δ. Therefore, with some damping the threshold Δ, for which $\dot{\phi}$ is always negative, is less negative than for $\gamma = 0$. This description is observed numeri-

cally. Currently, we are attempting to quantify the above description.

Last, we investigate the dependence of e_f as a function of γ for $\bar{\Delta} = -2^{1/3}$ since, as just argued, this is the $\bar{\Delta}$ for which e_f is largest when $e_o(0) = 0$. When $\bar{\gamma}$ is "small" the value of $d\bar{e}_f^2/d\bar{\Delta} = -3/4$; which is not a function of $\bar{\Delta}$ or $\bar{\gamma}$. Since $\bar{e}_f^2 \simeq 1$ when $\bar{\Delta} = -1$ (for $\gamma = 0$) then

$$\bar{e}_f^2 \simeq -\frac{3}{4}\bar{\Delta} + \frac{1}{4} \tag{56}$$

for $\bar{\Delta} < -1$. Therefore, $\bar{e}_f(\Delta = -2^{1/3}) \simeq 1.1$. As γ is increased, eventually the most negative $\bar{\Delta}$ for which three real solutions exist equals $-2^{1/3}$. The value of γ for which this occurs can be determined by solving Eq. (54) and this is presented in Fig. 1b. An approximate value for this γ can be found by utilizing the fact that the most negative Δ is very close to the Δ where $\bar{e}_f = \frac{1}{3\bar{\gamma}}$. Earlier it was shown that $\bar{e}_f = \frac{1}{3}\bar{\gamma}$ when $\bar{\Delta} = \frac{-4}{27\bar{\gamma}^2}$. When $\bar{\Delta} = -2^{1/3}$, it follows that $\bar{\gamma} = .34$, which is very close to the exact value obtained from Fig. 1b. Additionally, for this value of $\bar{\gamma}$, $e_f = .97$, which is not very different from the $\gamma = 0$ amplitude. This value for $\bar{\gamma}$ is also very close to the value above which only one real solution exists, $\bar{\gamma} = .458$.

IIB3. Rise Time Effects

Until now we have assumed that α_1 and α_2, i.e., F were constant in time. If this assumption is relaxed, it could alter the results

in two ways--the first being the nonlinear frequency shift due to the relativistic corrections to the electron's motion in the fields of the lasers. Recall that the total nonlinear frequency shift is

$$\delta\omega = \dot{\phi} = -\frac{3}{16}|e_o|^2 - \frac{1}{8}(|\alpha_1|^2 + |\alpha_2|^2) - F\cos\phi \qquad (57)$$

When $\alpha_1 = \alpha_2$, then $F = \frac{\alpha_1\alpha_2}{4} = \frac{\alpha_1^2}{4} = \frac{\alpha_2^2}{4}$ so

$$\delta\omega = -\frac{3}{16}|e_o|^2 - F - F\cos\phi. \qquad (58)$$

If α_1 and α_2 are constant in time, then the contributions of α_1 and α_2 to $\delta\omega$ as shown in Eq (57) can simply be renormalized out.

The second way a non-constant F could alter the results is if the value of e_m is reached during the rise time of the lasers. In this case e_m depends on the instanteous value of F. To investigate both rise time effects we start from a slightly modified version of Eqs. (25) and (26)

$$\dot{e}_o = F\sin\phi - \frac{\dot{F}}{2}\cos\phi \qquad (59)$$

$$e_o\dot{\phi} = \Delta e_o + Ce_o^3 + F\cos\phi + \frac{\dot{F}}{2}\sin\phi \qquad (60)$$

The $\dot{F}$ terms appear naturally in the perturbation analysis given in Appendix A. As in Ref.16 , we multiply Eq. (59) by cos ϕ and Eq. (60) by -sin ϕ and add these equations to obtain

$$\frac{d}{dt}(e_o \cos \phi) = - \Delta e_o \sin \phi - Ce_o^3 \sin \phi - \frac{\dot{F}}{2} \tag{61}$$

We next use Eq. (59) and define $\Delta = \Delta_o + F$, where $\frac{d\Delta_o}{dt} = 0$, to find

$$\frac{d}{dt}\left(e_o \cos \phi + \frac{F}{2} + \frac{e_o^2}{2} + \frac{\Delta_o e_o^2}{2F} + \frac{Ce_o^4}{4F}\right)$$

$$+ \left[\frac{\Delta_o e_o^2}{2F^2} + \frac{Ce_o^4}{4F^2} + \left(\frac{\Delta_o e_o}{2F} + \frac{e_o}{2} + \frac{Ce_o^3}{2F}\right) \cos \phi\right]\dot{F} = 0 \tag{62}$$

For most of the growth time $\cos \phi << 1$ and since $\frac{F}{e_o} << 1$, then

$$\frac{\Delta_o e_o}{2F} << \frac{\Delta_o e_o^2}{2F^2} \quad \text{and} \quad \frac{Ce_o^3}{2F} << \frac{Ce_o^4}{4F^2} \tag{63}$$

allowing Eq. (62) to be rewritten as

$$\frac{d}{dt}\left(e_o \cos \phi + \frac{F}{2} + \frac{e_o^2}{2} + \frac{\Delta_o e_o^2}{2F} + \frac{Ce_o^4}{4F}\right.$$

$$\left. + \left(\frac{\Delta_o e_o^2}{2F^2} + \frac{Ce_o^4}{4F^2} + \frac{e_o}{2} \cos \phi\right)\dot{F} = 0. \right. \tag{64}$$

We assume a priori that the last term does not, to lowest order, effect the evolution of e_o, so that $e_o \cos \phi$ can be approximated as

$$- \frac{F}{2} - \frac{e_o^2}{2} - \frac{\Delta_o e_o^2}{2F} - \frac{Ce_o^4}{4F} .$$

The last term in Eq. (81) then becomes

$$\left(\frac{\Delta_o e_o^2}{2F^2} + \frac{Ce_o^4}{4F^2} - \frac{F}{4} - \frac{e_o^2}{4} - \frac{\Delta_o e_o^2}{4F} - \frac{Ce_o^4}{8F}\right)\dot{F} \tag{65}$$

In general, $F \ll 1$ and $e_o^2/F^2 \ll 1$, so

$$\frac{\Delta_o e_o^2}{2F^2} \gg \frac{\Delta_o e_o^2}{4F}, \quad \frac{Ce_o^4}{4F^2} \gg \frac{Ce_o^4}{8F}, \quad F\dot{F} \ll \dot{F}, \text{ and } \frac{Ce_o^4}{4F^2} \gg \frac{e_o^2}{4} .$$

Expression (65) can therefore be rewritten as

$$\left(\frac{\Delta_o e_o^2}{2F^2} + \frac{Ce_o^4}{4F^2}\right)\dot{F}$$

permitting Eq. (64) to be approximated as

$$\frac{d}{dt}\left(e_o \cos\phi + \frac{F}{2} + \frac{e_o^2}{2} + \frac{\Delta_o e_o^2}{2F} + \frac{Ce_o^4}{4F}\right) + \left(\frac{\Delta_o e_o^2}{2F^2} + \frac{Ce_o^4}{4F^2}\right)\dot{F} = 0 \qquad (66)$$

We next note the following:

$$\frac{d}{dt}\frac{Ce_o^4}{4F} = \frac{Ce_o^3}{F}\frac{de_o}{dt} - \frac{C}{4}\frac{e_o^4}{F^2}\frac{dF}{dt} .$$

The ratio of the terms on the right-hand side is

$$R \equiv \frac{\dfrac{dF}{dt}\, e_o}{4F\,\dfrac{de_o}{dt}} .$$

Since for most of the growth time $\sin\phi \simeq 1$, then from Eq. (25) the ratio R excluding the numerical factor can be replaced by

$$r \equiv \frac{\dfrac{dF}{dt}\int dt\, F}{F^2} . \qquad (67)$$

For a large class of monotonically increasing functions, the ratio r for a finite F is ≃ 1 until dF/dt → 0 for a finite F. To show this we solve Eq. (67) for r =1 and find $F = F_0 e^{-(t-t_0)/c_1}$ which can be used as a reasonable fit to many monotonically increasing functions of t. Another example is if $F = F_0 t^n$ then $r = n/(n+1)$, which tends to unity as n gets large.

If r ≃ 1, it then follows that

$$\frac{C}{4}\frac{e_0^4}{F^2}\frac{dF}{dt} \simeq \frac{1}{3}\frac{d}{dt}\frac{Ce_0^4}{4F}.$$

A similar argument can be used to conclude

$$\frac{\Delta_0}{2}\frac{e_0^4}{F^2}\frac{dF}{dt} \simeq \frac{d}{dt}\frac{\Delta_0 e_0^2}{2F}.$$

In what follows we assume the lasers' intensity, i.e., F rises monotonically from 0 to F_0 in a time τ and for t > τ it remains constant at the value F_0. (If it decreased after τ then the values we calculated would be lower bounds.) There are now two situations to study. The first is that when the plasma wave reaches its peak amplitude for some saturation time $t_s > \tau$ while the second is that when $t_s < \tau$. (This is not necessarily the logical order.)

For the first situation (t > τ, F = F_0), Eq. (64) becomes

$$e_0 \cos\phi + \frac{e_0^2}{2} + \frac{\Delta_0 e_0^2}{2F_0} + \frac{Ce_0^4}{4F_0} + \left[\frac{\Delta_0 e_{0(\tau)}^2}{2F_0} + \frac{Ce_{0(\tau)}^4}{2F_0} + \frac{F_0}{2}\right] \qquad (68)$$

where $e_0(\tau) \simeq \int_0^\tau dt\ F(t)$. The term in brackets is an upper bound

since the integral was carried out for times when $dF/dt = 0$. Furthermore, the term in parantheses, no longer being a function of time, can be relabeled as a constant κ, resulting in

$$e_o \cos \phi + \frac{e_o^2}{2} + \frac{\Delta_o e_o^2}{2F_o} + \frac{Ce_o^4}{4F_o} + \kappa = 0. \tag{69}$$

When e_o reaches its peak amplitude, by definition $\dot{e}_o = 0$ or

$F \sin \phi - \frac{\dot{F}}{2} \cos \phi = 0$. For $t > \tau$, $\dot{F} = 0$ so when

$\dot{e}_o = 0$, $\sin \phi = 0$ or $\cos \phi = -1$. It then follows from Eq. (69) that the peak amplitude $\bar{e}_o$ is given by

$$-\bar{e}_o + \frac{(\Delta_o + F_o)}{2F_o} \bar{e}_o^2 + \frac{C\bar{e}_o^4}{4F_o} + \kappa = 0. \tag{70}$$

We next assume that κ represents only a slight perturbation in Eq. (70). The amplitude $\bar{e}_o$, considered as a function of κ, can then be obtained via a Taylor expansion

$$\bar{e}_o = e_m + \frac{d\bar{e}_o}{d\kappa} \kappa + \ldots .$$

From Eq. (70) we obtain

$$\frac{d\bar{e}_o}{d\kappa} = \frac{1}{1 - \frac{\Delta e_m}{F} - \frac{Ce_m^3}{F}} . \tag{71}$$

For Δ's ($\Delta = \Delta_o + F$) of interest, the denominator is less than -3.

Hence, the absolute value of the correction to e_m is smaller than

$$\frac{1}{3}\left(\frac{\Delta_o e_o^2(\tau)}{2F_o} + \frac{C}{12}\frac{e_o^4(\tau)}{F_o} + \frac{F_o}{2}\right) \tag{72}$$

The largest possible percentage correction to e_m occurs if $t_s \sim \tau$. Formula (72) would then be $\frac{e_m}{9}$ implying a 16 percent negative correction. Therefore, in general for this first case where $t_s > \tau$, the peak amplitude $\bar{e}_o$ does not depend on the form or the existence of the time dependence of F, just on the final value F_o.

We next discuss the second situation where saturation occurs for a $t_s > \tau$. Using the assumptions that $r \simeq 1$ and $t_s < \tau$, Eq. (68) gives

$$e_o \cos\phi + \frac{F}{2} + \frac{e_o^2}{2} + \frac{\Delta_o e_o^2}{F} + \frac{Ce_o^4}{3F} = 0. \tag{73}$$

If $\dot{F} << F$, then as before when $\dot{e}_o = 0$, $\cos\phi = -1$. Hence, saturation occurs whenever e_o reaches a value such that

$$-e_o(t_s) + \frac{F(t_s)}{2} + \frac{e_o^2(t_s)}{2} + \Delta_o\frac{e_o^2(t_s)}{F(t_s)} + \frac{Ce_o^4(t_s)}{3F(t)} = 0. \tag{74}$$

We assume $e_o(t) = \int_o^t dt'F$ to obtain analytic expressions. This is true except for $t \simeq t_s$ (as $\sin\phi \simeq 0$). The value of t_s is found by determining the value of t that satisfies

$$-\int_o^{t_s} dt'F(t') + \frac{F(t_s)}{2} + \frac{\left[\int_o^{t_s} dt'F(t')\right]^2}{2} + \frac{2\Delta_o}{3}\frac{\left[\int_o^{t_s} dt'F(t')\right]^2}{F(t)}$$

$$+ \frac{C}{3} \frac{\left[\int_o^{t_s} dt' F(t')\right]^4}{F(t)} = 0. \tag{75}$$

The value of $\bar{e}_o$ is consequently

$$\bar{e}_o \simeq \int_o^{t_s} dt' F(t'). \tag{76}$$

If $\Delta_o = 0$ and we neglect the F/2 term, Eq. (75) can be rewritten as

$$\int_o^{t_s} dt' F = \left(\frac{3F(t_s)}{C}\right)^{1/3}. \tag{77}$$

So $\bar{e}_o$ saturates at a time t_s when $\bar{e}_o$ is equal to its instantaneous "Rosenbluth and Liu" peak value. If $\Delta \neq 0$, then the instantaneous "Tang et al." value would be used.

To obtain some scaling laws, we assume the trial function of $F = F_o \frac{t^2}{\tau^2}$ and find

$$\omega_p t_s \simeq 2.38(\omega_p \tau)^{4/7} F_o^{-2/7} \tag{78a}$$

and

$$\bar{e}_o = \int_o^{t_s} dt F(t) \simeq 4.5 F_o^{1/7} \tau^{-2/7}. \tag{78b}$$

In Refs. 8 and 29 we used $\left(\frac{4F}{C}\right)^{1/3}$ rather than $\left(\frac{3F}{C}\right)^{1/3}$ in Eq. (77) and this accounts for the small numerical discrepancies (~ percent). The formulas in Eqs. (78a) and (78b) agree well with previous simulation results [5,8,30,31] and those to be presented later

in Chapter III.

IIB4. Phase Velocity Shift

In regard to phase velocity shifts, the arguments used by previous authors[9] is that since $\omega_0 - \dot{\phi}$ represents the frequency shift and since κ is assumed to be fixed, $\delta v_\phi = (\omega_0 - \dot{\phi})/\kappa = \delta\omega/\kappa$. Taking this expression seriously leads erroneously to the conclusion that a plasma wave excited by Beat Wave Excitation could never lead to significant acceleration. To see this we quote a result first derived in Ref. 6 That is, the maximum energy gained in a single stage of the PBWA is

$$4e_0\gamma_\phi^2\, mc^2. \tag{79}$$

Since v_ϕ is now a function of e_0, hence so is γ_ϕ. Furthermore, for large v_ϕ, γ_ϕ changes by large amounts for small changes in v_ϕ. This is easily seen from

$$\delta\gamma_\phi = \frac{d\gamma_\phi}{dv_\phi}\,\delta v_\phi = \gamma_\phi^3\,\frac{v_\phi}{c}\,\frac{\delta v_\phi}{c} - \frac{v_\phi\delta v_\phi}{c} - \frac{\gamma_\phi^3\delta v_\phi}{c}\,. \tag{80}$$

As a result, small changes can alter the maximum energy gain by enormous amounts.

Using the expression for $\dot{\phi}$ given in Eq. (26b) gives

$$\frac{v_\phi}{c} \equiv \beta_\phi = \frac{v_{\phi o}}{c}\left(1 - \frac{9}{64}\,e_0^2\right) \tag{81}$$

where $v_{\phi o} \equiv \omega_o/\kappa_o \simeq v_{go}$. It follows therefore that

$$\gamma_\phi^2 \equiv \left(1 - \frac{v_\phi^2}{c^2}\right)^{-1} = \left[1 - \frac{v_{\phi o}^2}{c^2}\left(1 - \frac{9}{32}\, e_o^2\right)\right] \tag{82}$$

$$\simeq \frac{\omega_1^2}{\omega_p^2}\left(1 - \frac{9}{32}\,\frac{\omega_p^2}{\omega_o^2}\,\frac{v_{\phi o}^2}{c^2}\, e_o^2\right). \tag{83}$$

We have assumed that $\gamma_{\phi o} = \frac{\omega_o}{\omega_p}$. For large α_i's, the value of $\gamma_{\phi o}$ is larger due to a nonlinear decrease in the index of refraction of light. The maximum energy gained as a function of e_o occurs when

$$\frac{d}{de_o}\, e_o\gamma_\phi^2 = \frac{d}{de_o}\,\frac{\omega_1^2}{\omega_p^2}\left(e_o - \frac{9}{32}\,\frac{\omega_p^2}{\omega_1^2}\,\frac{v_{\phi o}^2}{c^2}\, e_o^3\right) = 0. \tag{84}$$

This occurs for

$$e_o = \left(\frac{32}{27}\,\frac{\omega_1^2}{\omega_p^2} = \frac{c^2}{v_{\phi o}^2}\right)^{1/2} \simeq \frac{\omega_p}{\omega_1}\ . \tag{85}$$

If this were true, then the maximum energy gained would scale as $\omega_1/\omega_p(mc^2)$ rather than $\omega_1^2/\omega_p^2(mc^2)$.

Fortunately for the future of the PBWA, the above analysis has one important error. It was assumed that ϕ was a function of time only, while in reality it is also a function of position. We argue, henceforth, that ϕ is instead a function of $t - x/v_{go}$ to lowest order. We can do this because in a cold plasma one point in the plasma is not influenced by other points, so only the driving

force will cause spatial variations. The driving force's envelope moves at the group velocity of light v_{go}, so $t - x/v_{go}$ is the appropriate variable.

The phase of the excited plasma wave now has the form

$$\kappa_o x - \omega_o t + \phi(x,t). \tag{86}$$

The phase velocity is therefore derived from

$$\frac{d}{dt}\left[\kappa_o x - \omega_o t + \phi(x,t) = 0\right] \Rightarrow \kappa_o v_\phi - \omega_o + \frac{\partial\phi}{\partial t} + v_\phi \frac{\partial\phi}{\partial x} = 0. \tag{87}$$

As a result

$$v_\phi = \frac{\omega_o - \dfrac{\partial\phi}{\partial t}}{\kappa_o + \dfrac{\partial\phi}{\partial x}} = v_{\phi o}\left[\frac{1 - \dfrac{1}{\omega_o}\dfrac{\partial\phi}{\partial t}}{1 + \dfrac{1}{\kappa_o}\dfrac{\partial\phi}{\partial x}}\right]. \tag{88}$$

Using the fact that ϕ is a function of $t - \frac{x}{v_{go}}$ gives

$$\frac{\partial\phi}{\partial x} = -\frac{1}{v_{go}}\frac{\partial\phi}{\partial t}. \tag{89}$$

We can therefore write

$$v_\phi = v_{\phi o}\,\frac{\left(1 - \dfrac{1}{\omega_o}\dfrac{\partial\phi}{\partial t}\right)}{\left(1 - \dfrac{1}{\omega_o}\dfrac{v_{\phi o}}{v_{go}}\dfrac{\partial\phi}{\partial t}\right)}. \tag{90}$$

Recalling that $v_{\phi o} \simeq v_{go}$, then from Eq. (90) we see that $v_\phi \simeq v_{\phi o}$. The conclusion is, therefore, that a nonlinear shift in κ arises arises that compensates for the nonlinear shift in ω enabling the

phase velocity to remain constant.

IIB5. Harmonics

In this section we briefly comment on the issue of plasma wave harmonics. The presence of harmonics gives rise to nonlinear wave steepening (but not to any nonlinear frequency shift). Noble[22] used a different approach to obtain the nonlinear waveforms. He used asymptotic expansion about the exact solution to the undriven nonlinear differential equation. His solution was consequently in terms of elliptic functions. We prefer to use an expansion in terms of sinusoids. In fact, we find that retaining the first three terms in the asymptotic expansion is adequate to describe the nonlinear character of the wave for many pump strengths of interest.

From the perturbation analysis in Appendix A, expressions were obtained for e_1 and e_2 as functions of e_o and they were

$$e_1 = \tfrac{1}{2}\, e_o^2 \sin 2\left(\kappa_o x - \omega_o t + \phi\right) \tag{91}$$

$$e_2 = -\tfrac{9}{64}\, e_o^3 \cos 3\left(\kappa_o x - \omega_o t + \phi\right). \tag{92}$$

The value for the total longitudinal electric field is, therefore

$$E_x = e_o\left(\cos\psi + \frac{e_o}{2}\sin 2\psi - \tfrac{9}{64}\, e_o^2 \cos 3\psi + 0(e_o^3)\right). \tag{93}$$

The importance of the correction to E_x from e_1 can be easily estimated recursively. Taking the derivative of Eq. (93) and setting

it to zero yields (e_2 can be neglected when calculating ψ_m)

$$-\sin \psi_m + e_o \cos 2\psi_m = 0 \quad \text{or} \tag{94}$$

$$\psi_m = \sin^{-1}\left[-\frac{1}{4e_o} + \frac{1}{2}\left(\frac{1}{4e_o^2} + 2\right)^{1/2}\right]. \tag{95}$$

The amplitude

$$E_x = e_o \cos \psi_m + \frac{e_o^2}{2} \sin 2\psi_m - \frac{9}{64} e_o^3 \cos 3\psi_m \tag{96}$$

can be obtained exactly for a particular set of parameters. To ascertain a scaling law, we assume that $e_o << 1$, then Eq. (95) gives $\psi_o = e_o$. It follows then that

$$E_x \equiv e_o \cos \psi_m + \frac{e_o^2}{2} \sin 2\psi_m - \frac{9}{64} e_o^3 \cos 3\psi_m \simeq e_o\left(1 + \frac{23}{64} e_o^2\right). \tag{97}$$

The percentage increase to E_x is $\sim\frac{23}{64} e_o^2$. If it is ever necessary, the contributions from higher harmonics can also be formally obtained.

The ratio of the second harmonic to the fundamental for the electric field is $\frac{1}{2} e_o$ as shown in Eq. (113). The ratio is different, however, for the potential and the density since $|\kappa\phi| = |E| = \left|\frac{n4\pi}{\kappa}\right|$. The ratio is $\phi_1/\phi_o = e_o/4$ for the potential, and the ratio is $n_1/n_o = e_o$ for the density. Since the second harmonic is twice as large in the density as the electric field, it might appear that the percentage increase to the density would then be twice as

large also. This is not the case, however, as the percentage increase to the density is much larger. To see this we simply note that since

$$E = e_o \cos \psi + \frac{e_o^2}{2} \sin 2\psi, \tag{98}$$

the total perturbed density is

$$n = n_o \sin \psi - n_o^2 \cos 2\psi. \tag{99}$$

The value of ψ that maximizes n is $\psi = \pi/2$ where, as it happens, both sin ψ and -cos 2ψ obtain their maximum values. As a result, the maximum n becomes

$$n_m = n_o(1 + n_o) = e_o(1 + e_o)$$

which clearly illustrates that n_m is much larger than E_m .

We now derive[37] from simple arguments the absolute maximum and minimum values for the density. We only use Ampere's Law, Gauss's Law, the fact that all fields are only functions of the variable $\psi \equiv x - ct$, and the fact that v is limited to $-c < v < c$. So

$$\frac{\partial}{\partial t} E + 4\pi j = 0 \Rightarrow \frac{d}{d\psi} E - 4\pi eN \frac{v}{c} = 0 \tag{100a}$$

$$\frac{\partial}{\partial x} E = 4\pi e(\bar{n}_o - N) \Rightarrow \frac{d}{dx} E = 4\pi e(\bar{n}_o + N). \tag{100b}$$

Subtracting Eq. (100a) from Eq. (100b) gives

$$\bar{n}_o - N = N \frac{v}{c}.$$

Hence,

$$N = \frac{\bar{n}_o}{1 - v/c} \tag{101}$$

leading to the conclusion that

$$-\frac{\bar{n}_o}{2} < N < \infty. \tag{102}$$

A point of interest is that when $v = v_\phi$, which in this case is $v \sim c$, the wave is defined to be in the wave breaking state. A formula often quoted for the associated cold wave breaking value for the electric field is $mc\omega_p/c$. However, Akhiezer and Polovin[37] showed that the correct cold wave breaking value for the electric field is

$$\frac{\sqrt{2}\, mc\omega_p}{e}\left(\gamma_\phi - 1\right)^{1/2}. \tag{103}$$

This indicates that for relativistic phase velocities, i.e., $\gamma_\phi >> 1$, electric fields considerably larger than $mc\omega_p/e$ are theoretically possible. In practice, thermal effects will, in general, keep the electric field below $mc\omega_p/e$ so the often-quoted result is still a good guide.

IIB6. Pump Depletion

As the plasma wave is excited, the energy of the pump waves is necessarily depleted. The depletion of the pumps for practical reasons should not occur in distances less than that needed to obtain the maximum possible electric field E_m. On the other hand, for maximum efficiency the depletion distance should not be larger than the acceleration distance so that most of the energy of the pumps is not wasted. The considerations outlined above are crudely quantified below following the same procedure used in Ref. 35. We begin with an equation that represents energy balance

$$L_p A_p E_p^2 = c\tau_\ell A_\ell (E_1^2 + E_2^2) \tag{104}$$

where L_p is the length over which the plasma wave is excited, τ_ℓ is the laser pulse duration, the A's are the cross-sectional areas, and the E's are electric fields. We assume $A_p = A_\ell$ and normalize the E's to get

$$L_p e_m^2 = c\tau_\ell \, 2a_1^2 \frac{\omega_1^2}{\omega_p^2} . \tag{105}$$

Since L_p need be no longer than the distance for maximum acceleration, we set it equal to

$L_p = 2\pi\gamma_\phi^2 \frac{c}{\omega_p} \equiv \frac{\pi\omega_1^2}{\omega_p^2} \frac{c}{\omega_p}$. In addition, for e_o we use

$e_m = \left(\frac{64}{3} F\right)^{1/3} (\alpha_1^2 = 4F)$, resulting in

$$2\pi \frac{\omega_1^2}{\omega_p^2} \frac{c}{\omega_p} \left(\frac{64}{3}F\right)^{2/3} = c\tau_\ell \; 8F \frac{\omega_1^2}{\omega_p^2} \tag{106}$$

or

$$c\tau_\ell = \frac{2\pi}{8} \left(\frac{64}{3}\right)^{2/3} F^{-1/3} \frac{c}{\omega_p} \; . \tag{107}$$

We estimate τ_ℓ crudely as the time required for e_o to reach e_m for a constant F. This can be approximated as[9]

$$\omega_p \tau_\ell \sim 1.2 \left(\frac{64}{3}\right)^{1/3} F^{-2/3}. \tag{108}$$

We substitute Eq. (108) into Eq. (107) to obtain

$$\left(\frac{64}{3}\right)^{1/3} F^{-2/3} = \frac{2\pi}{8} \left(\frac{64}{3}\right)^{2/3} F^{-1/3} \tag{109}$$

or

$$F = \left(\frac{8}{2\pi}\right)^3 \left(\frac{3}{64}\right) (1.2)^3 \simeq .1. \tag{110}$$

The conclusion is that for maximum efficiency $F \simeq .1$. and that $c\tau_\ell \simeq 13c/\omega_p$.

The above estimate may at first glance seem too crude since we assumed that F was constant in time when calculating τ_ℓ. However, the effect of pump cascading has also been neglected. Pump cas-

cading refers to the generation of electromagnetic modes at frequencies $\pm n\omega_o$ from the original pumps. This subject, although done in another context, was first investigated by Cohen, Kaufman, and Watson.[13] They found that if all light waves were approximately at the same frequency, $\omega_L >> \omega_p$ and dispersion was neglected, then the driving force F of the plasma wave is constant. When such assumptions are made, however, energy is no longer conserved. Although it is difficult to rigorously prove analytically, it appears that even when energy is conserved the phenomena of cascading results in a more constant driving force.

Recently Horton and Tajima[38] have addressed the issue of pump deplection in the PBWA. In their work they neglect the cascading and are therefore able to obtain some analytical expressions since they are dealing with a three-wave system. On the other hand, Karttunen and Salomaa[39] have addressed cascading as it applies to the PBWA following the original work of Cohen et al.[19] They assume there to be an infinite number of waves all with the same frequency $\omega_L >> \omega_p$ and they neglect dispersion to obtain analytical expressions. They find that frequency cascading is approximately symmetrical in the + and - directions. If energy is conserved, then for appreciable efficiency cascading must be in the - direction in order to conserve photons (Manley-Rowe relation). If cascading is in the - direction and dispersion is included, then the phase velocity of the plasma wave might decrease in an average sense. Since the phase relationship between each pair of light waves is different, the coherence of the plasma wave might also be affected.

The analysis of cascading is further complicated by the necessity of including the higher order coupling such as that shown in Appendix B. The issue of pump depletion and/or cascading and efficiency is, consequently, not completely resolved. This area is one of the most important unresolved issues in Beat Wave Excitation.

IIB7. Inhomogeneities

In the previous sections we have assumed that the time invariant part of the plasma density N_0 (the ion density) did not vary with position. Within the validity of linear theory the differential equation that describes the excitation of the plasma wave in a cold plasma, when formulated in Eulerian coordinates, is easily extended to inhomogeneous plasmas. (In Lagrangian coordinates the linear assumption has a different meaning.) The resulting partial differential equation is easily solved because of the absence of spatial derivatives. Therefore, the differential equations can be solved at each position independently of the other positions. In other words, in a cold plasma there is no communication between different positions in a plasma. Plasma non-uniformities of interest are density ripples resulting from ion waves, ion noise, and long-scale length density gradients. We next briefly discuss each in turn.

The effect of sinusoidal density ripples on plasma oscillations has been studied previously through theory and computer simulations and recently experiments.[40] Dawson and Oberman[42] investigated the

damping of dipole plasma oscillations with uniformly distributed discrete ions. Subsequently, they demonstrated[43] that the presence of coherent ion waves would lead to a considerably larger damping rate. Their theory includes kinetic effects and assumes "steady state."

Kruer[44] and Kaw, Lin, and Dawson,[45] on the other hand, solved an initial value problem for a single ripple and then made ad hoc assumptions concerning kinetic effects based on simulation results. For illustrative purposes, we follow a procedure analogous to that used by Kaw, Lin and Dawson.[45]

In the presence of an ion ripple, the model linear differential equation for beat wave excitation is

$$\left[\frac{\partial^2}{\partial t^2} + \omega_{po}^2\left(1 + \frac{\delta n}{n_o}\sin \kappa x\right)\right]E_x = F_o \sin(\kappa_o x - \omega_o t). \qquad (111)$$

We have neglected relativistic effects since we are interested in the early time, e.g., linear behavior. The solution to Eq. (111) can be written down explicitly since spatial derivatives are absent and for the initial conditions

$$E_x\Big|_{t=o} = \frac{\partial E_x}{\partial t}\Big|_{t=o}; \quad \text{it is}$$

$$E_x = \frac{F_o \sin \psi_o}{\omega_p^2 - \omega_o^2} - \frac{F_o \sin(\kappa_o x - \omega_p t)}{\omega_p^2 - \omega_o^2} + \frac{(\omega_o - \omega_p)F_o}{\omega_p} \frac{\cos \kappa_o x \sin \omega_p t}{\omega_p^2 - \omega_o^2} \qquad (112)$$

where

$$\omega_p^2 \equiv \omega_{po}^2(1 + \epsilon \sin \kappa x) \text{ and } \epsilon \equiv \frac{\delta_n}{\bar{n}_o}.$$

We next define $\Delta \equiv \omega_p^2 - \omega_{po}^2$ and $\delta \equiv \omega_p - \omega_{po}$.

It follows then that

$$\Delta = \omega_{po}^2 \epsilon \sin \kappa x \tag{113}$$

and after Taylor expanding that

$$\delta = \omega_{po}(1 + \epsilon \sin \kappa x)^{1/2} - \omega_{po} = \frac{\omega_{po}\epsilon}{2} \sin \kappa x - \frac{\epsilon^2}{8} \omega_{po} \sin^2 \kappa x + \ldots$$

$$= \frac{\Delta}{2\omega_{po}} - \frac{\Delta^2}{\omega_{po}^3 8} + \ldots \tag{114}$$

We set $\omega_o = \omega_{po}$ and use Eqs. (113) and (114) to rewrite Eq. (112) as

$$E_x = \frac{F_o}{\Delta} \sin \psi_o - \frac{F_o}{\Delta} (\sin \psi_o \cos \delta t - \cos \psi_o \sin \delta t) \tag{115}$$

$$+ \frac{\delta}{\omega_p} \frac{F_o}{\Delta} \cos \kappa_o x (\sin \omega_{po} t \cos \delta t + \cos \omega_{po} t \sin \delta t).$$

In the limit that $\epsilon \to 0$, Eq. (115) becomes

$$E_x = \frac{F_o t}{2\omega_p} \cos \psi_o + \frac{F_o}{4\omega_{po}^2} (\sin \bar{\psi}_o - \sin \psi_o) \tag{116}$$

which describes the well-known secular growth. The terms on the

right are necessary in order that $\left.\frac{\partial E}{\partial t}\right|_{t=0} = 0$. We define $\bar{\psi}_o \equiv (\kappa_o x + \omega_o t)$.

To obtain useful analytic expressions, we keep only the lowest order term in Eq. (114). With this substitution, Eq. (116) can be expressed as

$$E_x = \frac{F_o}{\Delta} \sin \psi_o - \frac{F_o}{\Delta} \sin \psi_o \sum_{-\infty}^{\infty} J_n\left(\frac{\epsilon}{2} \omega_p t\right) \cos n\kappa x$$

$$+ \frac{F_o}{\Delta} \cos \psi_o \sum_{-\infty}^{\infty} J_n\left(\frac{\epsilon}{2} \omega_p t\right) \sin n\kappa x$$

$$- \frac{F_o}{\omega_o^2 4}\left[\left(\sin \bar{\psi}_o - \sin \psi_o\right)\sum_{-\infty}^{\infty} J_n\left(\frac{\epsilon}{2} \omega_p t\right) \cos n\kappa x\right.$$

$$\left. + \cos \bar{\psi}_o + \cos \psi_o\right)\sum_{-\infty}^{\infty} J_n\left(\frac{\epsilon}{2} \omega_p t\right) \sin \kappa x\Bigg] \qquad (117)$$

or

$$E_x = \frac{F_o}{\Delta}\left[\sin \psi_o - \sum_{-\infty}^{\infty} J_n\left(\frac{\epsilon}{2} \omega_p t\right)\sin (\psi_o - n\kappa x)\right.$$

$$- \delta\left(\sum_{-\infty}^{\infty} J_n\left(\frac{\epsilon}{2} \omega_{pt}\right)\sin (\bar{\psi}_o - n\kappa x)\right.$$

$$\left.\left. - \sum_{-\infty}^{\infty} J_n\left(\frac{\epsilon}{2} \omega_p t\right)\sin (\psi_o - n\kappa x)\right)\right] \qquad (118)$$

where the identities

$$\cos\left(t \frac{\epsilon}{2} \omega_p \sin \kappa x\right) = \sum_{-\infty}^{\infty} J_n\left(\frac{\epsilon}{2} \omega_{pt}\right) \cos n\kappa x \qquad (119)$$

$$\sin\left(t\,\frac{\epsilon}{2}\,\omega_p \sin \kappa x\right) = \sum_{-\infty}^{\infty} J_n\left(\frac{\epsilon}{2}\,\omega_{pt}\right) \sin n\kappa x \qquad (120)$$

are used. In order to reduce Eq. (118) into a sum of coupled modes we need to use the expression

$$\frac{1}{\Delta} = \frac{1}{\epsilon \sin \kappa x} = \frac{2}{\epsilon} \sum_{j} \sin\,[(2j + 1)\kappa x]. \qquad (121)$$

Substituting Eq. (121) into Eq. (118) gives

$$E_x = \frac{F_o}{\epsilon}\left[\sum_{j=o}^{\infty} \cos\,[\psi_o - (2j + 1)\kappa x] - \cos\,[\psi_o + (2j + 1)\kappa x]\right.$$

$$- \sum_{n=-\infty}^{\infty} J_n\left(\frac{\epsilon}{2}\omega_p t\right) \sum_{j=o}^{\infty} \left\{\cos\,[\psi_o - (n + 2j + 1)\kappa x]\right.$$

$$\left. - \cos\,\{\psi_o - [n - (2j + 1]\kappa x)\}\right\}$$

$$\left. - \frac{F_o}{2}\left\{\sum_{-\infty}^{\infty} J_n\left(\frac{\epsilon}{2}\omega_p t\right)\,[\sin\,(\bar{\psi}_o - n\kappa x)] - \sin\,(\psi_o - n\kappa x)]\right\}. \qquad (122)\right.$$

Recall that the main purpose of the preceding analysis was to determine what effect a static density ripple has on the evolution of the mode with phase velocity ω_o/κ_o, i.e., modes with ψ_o in the argument of the sinusoids. We label this the fundamental mode. From Eq. (122) we find that the fundamental mode evolves in time according to

$$\frac{2F_o}{\epsilon\omega_{po}^2} \sum_{j=o}^{\infty} J_{2n+1}\left(\frac{\epsilon}{2}\,\omega_p t\right) \cos\,\psi_o - \frac{F_o}{2} J_o\left(\frac{\epsilon}{2}\,\omega_p t\right)\left(\sin\,\bar{\psi}_o - \sin\,\psi_o\right). \qquad (123)$$

As before, the term on the right is required to satisfy the chosen initial conditions. From Eq. (123) we extract two important points. The first is that the fundamental mode, i.e., the mode with phase velocity ω_o/κ_o, has a maximum value of

$$E_x(\psi_o) \simeq .734 \frac{2F_o}{\epsilon\omega_{po}^2} \tag{124}$$

where .734 is the maximum value of $\sum_{n=o}^{\infty} J_{2n+1}(x) = \frac{1}{2}\int_o^x dx' J_o(x')$. For parameters of interest, Eq. (124) can give a value for E_x significantly below that of relativistic saturation. The second point is that the time at which this maximum value is obtained is given by

$$\frac{\epsilon\omega_p\tau_s}{2} = 2.4 \Rightarrow \omega_p\tau_s = \frac{4.8}{\epsilon} \tag{125}$$

where the maximum of $\sum_{n=o}^{\infty} J_{2n+1}(x)$ occurs at the first zero of $J_o(x)$, $x = 2.4$. We note that if J_n is expanded (the higher order J_n's do not contribute at early times) for small t, we obtain

$$E_x(\psi) \simeq \frac{F_o}{2} t \cos\psi_o \tag{126}$$

which is the early time secular growth. Our physical explanation is that given by Kaw, Lin, and Dawson.[45] As the fundamental mode is excited it couples to the ion wave and excites plasma waves with wave numbers at $\kappa_o \pm n\kappa$. The coupling represents a loss of energy for the fundamental mode. The amplitude of the fundamental

mode is bounded because eneregy is being lost to mode coupling faster than energy is being extracted from the pump. The evolution of the other modes is also given in Eq. (122).

Before we proceed we will briefly describe the validity of our simple yet surprisingly revealing treatment. The first issue is the validity of our starting linear differential equation. We have dropped the terms

$$\left(\frac{\partial}{\partial t}\, nv - \bar{n}_o v\, \frac{\partial}{\partial x}\, v\right) \tag{127}$$

while retaining the term

$$\omega_{po}^2\, \epsilon\, \sin \kappa x\, E. \tag{128}$$

We do this because nonlinear terms in expression (136) contribute no response at frequency ω_p until the 3rd order. Therefore, crudely speaking our model equation is valid if

$$\epsilon >> E^2, \tag{129}$$

which is satisfied for many situations of interest. Furthermore, numerical studies indicate that condition (129) is actually too severe. Another issue is the dropping of the higher order terms in Eq. (114). This is justified if

$$\frac{\epsilon^2}{8}\, \omega_{po}\, t\, \sin^2 \kappa x < \frac{\pi}{2}\, . \tag{130}$$

The preceding inequality is always satisfied for times up to and including the saturation time given in Eq. (127). This statement, based on physical grounds, assumes that ϵ is always less than unity.

Last, the treatment presented here has neglected thermal effects (both fluid and kinetic). Although no details will be given here, we briefly comment that the thermal effects reduce the amount of coupling described earlier. A more comprehensive treatment is found in Ref. 41. The fundamental mode consequently saturates at a higher level than in the cold plasma case. In particular, we find that the saturation amplitude (neglecting relativistic effects) of the fundamental mode scales linearly with the temperature. The reason that thermal effects reduce mode coupling is that the modes with high n (i.e., large κ) have a significant Bohm Gross frequency shift and, hence, are not resonant. Kaw et al.[45] called coupling with thermal effects quasi-resonant mode coupling for the undriven case. Further details can be found in Ref. 40. Additionally, we find in some preliminary kinetic simulations that for initially cold plasmas the slow (higher n) modes heat the plasma so that eventually only a few modes are nearly resonant.

In the preceding analysis the effect of a single coherent ion wave on the amplitude of the primary wave was considered. When many ion waves are present (a spectrum) the formalism described above remains unchanged. In the formulas for Δ and δ the term ϵ

sin κx is simply replaced with a summation $\sum_j \epsilon_j (\sin \kappa_j x + \phi_j)$.

Dawson and Oberman[43] treated a related problem from a different perspective. They calculated the effective damping of a spectrum of ion waves on a long wave length (dipole) electric field. This damping mechanism has the following physical origin. Concommitant with the electric field (E_o) there exists a fluid velocity (v_o). This velocity couples with the density spectrum to generate a current spectrum (j_s). The current in turn induces an electric field (E_s). The energy dissipated (j_s, E_s) is then equated with the energy lost $(\partial/\partial t)/(E_o^2/8\Pi)$ to give an effective damping rate

$$\gamma = \frac{\omega_o}{8} \sum_i \left|\frac{\delta n_i}{n_o}\right|^2 I_m \frac{1}{\epsilon(\omega_o, \kappa_i)} . \qquad (131)$$

Horton and Tajima[46] obtained a similar expression. They ignored kinetic effects and used a renormalized ϵ. Implicit in these calculation was, however, the assumption that the values of E_s resulting from j_s are steady-state amplitudes. Consequently, if other processes occur before the electric field (E_s) reaches its steady-state value, then the ensuing damping rate will not be given by Eq. (131). If the damping given by Eq. (131) is found to apply, then it could be used as the phenomenological damping used in Eq. (37).

Last, we briefly discuss the effect of long scale length density gradients. If thermal effects are neglected, then, as before, the problem becomes trivial in the linear limit. To see this we find it most convenient to resort to the Lagrangian descriptions.

For a time invariant density profile, the differential equations describing the evolutions of plasma oscillations for an arbitrary driving force is

$$\frac{\partial^2}{\partial t^2}\,\xi + \frac{4\pi e^2}{m}\int_{x_0}^{x_0+\xi} dx'\; n_0(x') = F \tag{132}$$

where $\xi(x_0,t)$ is the displacement of a fluid element from its equilibrium position. We assume $n_0(x) = n_0\left(1 + \frac{x}{L}\right)$ to obtain

$$\left[\frac{\partial^2}{\partial t^2} + \omega_{po}^2\left(1 + \frac{x_0}{L}\right)\right]\xi + \frac{\omega_{po}^2\xi^2}{2L} = F. \tag{133}$$

If the displacement is much less than the scalelength $\xi \ll L$, the last term on the left-hand side can be neglected. As before, the excitation can be treated locally as long as thermal effects do not matter. This is observed in the computer simulations which appear later in Chapter III.

IIB8. 2-D Effects

The description of Beat Wave excitation given previously in one dimension is altered in two important ways when two-dimensional effects are considered. (We ignore transverse instabilities of the plasma wave[47] and lasers[43] in this section.) The first occurs because n and E_x are no longer proportional to each other and this is inherently a nonrelativistic phenomenon. The second occurs because the relativistic detuning is different for different radial positions (assuming a radial dependent pump). This effect is

important whenever the saturation time is amplitude dependent.

The first effect was first discussed in the context of the plasma wake field accelerator.[49] Recently Fedele et al.[50] studied radial fields in cylindrical coordinates as they apply specifically in the PBWA. Their results can be summarized as follows. In the linear limit it can be easily shown that the scalar potential possesses the same transverse profile as the ponderomotive potential. Consequently, E_x, being proportional to ϕ in the linear approximation, has a transverse profile that also follows that of the ponderomotive potential. On the other hand, E_y and n have more complicated transverse profiles as they depend on transverse derivatives. The precise form for E_y and n depends on the details of the transverse profile.

The second effect was uncovered by two-dimensional simulations.[5,15] The evolution of e_x and e_y is described by three coupled differential equations.[51] To lowest order, however, we assume that the evolution of e_x does not depend on the evolution of e_y, i.e., we assume $E_x >> E_y$. This is tantamount to the neglect of transverse derivatives. Therefore, the variable y simply becomes a parameter in the equation for E_x. Recall from Eqs. (25) and (26) that in absence of rise time considerations the evolution of the envelope of E_x is described by

$$\dot{e}_0(y) = F(y) \sin \phi(y) \tag{134}$$

$$e_0(y)\, \dot{\phi}(y) = Ce_0(y)^3 + F(y) \cos \phi(y) \tag{135}$$

where the y dependence is explicitly shown. The final maximum amplitude is therefore

$$\left(4\,\frac{F(y)}{C}\right)^{1/3} \tag{136}$$

and the time it takes to reach this value can be crudely estimated to be

$$t_s \simeq \left(\frac{4}{F(y)^2 C}\right)^{1/3} \tag{137}$$

by assuming the secular growth until saturation. Since t_s scales as $F(y)^{-2/3}$ on the outside of the laser beam where F is smallest the plasma wave potential and accelerating electric field will saturate at a later time. This means that the potential will develop shorter scalelength transverse variations than those of the ponderomotive potential. The resulting transverse electric field E_y will now exhibit a more complicated spectrum of focusing and defocusing fields than those predicted from the linear calculations. To illustrate the development of the short scalelength perturbations, we first assume a solution where y is treated as a parameter.

$$\phi = \phi_0(y,t)\,\sin\,[\kappa_0 x - \omega_0 t - \int dt\,\Delta\omega_0(y,t)]. \tag{138}$$

The radial, i.e., E_y field is then given by

$$E_y = \frac{\partial \phi_o}{\partial y} \sin [\kappa_o x - \omega_o t - \int dt\, \Delta\omega_o(y,t)]$$

$$- \left(\int dt\, \frac{\partial \Delta\omega}{\partial y}\right) \phi_o \cos (\kappa_o x - \omega_o t - \Delta\omega_o t). \qquad (139)$$

Since transverse derivatives are assumed to be small (when $\frac{\partial \phi_o}{\partial y} < \kappa_o \phi_o$), then the first term in Eq. (139) is small. (This is the linear correction.) The second term, however, increases monotonically in time, so even though $(\partial\Delta\omega)/(\partial y)$ is small, a time t_o exists such that $\int dt(\partial\Delta\omega)/(\partial y)$ is finite. Specifically, E_y will become of the order of E_x when

$$\omega_p\, t_c = \left\langle \left(\frac{\partial \Delta\omega}{\partial y}\right) \right\rangle^{-1}, \qquad (140)$$

or for $\Delta\omega$ due to relativistic frequency shifts

$$\omega_p\, t_c \simeq \frac{32}{\langle a^2 \rangle}. \qquad (141)$$

At this time our assumption that $E_x >> E_y$ breaks down, so the full set of coupled equations must be used. The analysis presented above, although not rigorous, is remarkably consistent with simulations presented in Chapter III and elsewhere.[5,15]

IIC. Summary

We have examined various issues related to Beat Wave Excitation emphasizing their importance to the PBWA. We reviewed the basic

Eulerian fluid equations and concluded that the nonlinear frequency shift is negative and due only to relativistic effects. We examined the early time behavior for the case where the driving force is time-dependent. It was demonstrated that if "saturation" occurs after the rise time of the pulse the "saturation" amplitude does not depend on the details of the rise time. On the other hand, if "saturation" occurs during the rise time the saturation amplitude is nearly equal to the instantaneous "Rosenbluth and Liu" or "Tang et al." values.

We investigated the late time behavior including mismatch by studying the fixed points $\dot{e}_o = 0$ and $\dot{\phi} = 0$. It was argued that e_f, the value of e_o at the fixed point, is largest when $\Delta \simeq -\left(\frac{27}{2} F^2C\right)^{1/3}$ and $\gamma < .35\left(\frac{27}{4} F^2C\right)^{1/3}$. (We assume $e_o(0) = 0$.) For these parameters the maximum $e_f \simeq \left(\frac{4F}{C}\right)^{1/3}$. On the other hand, for $\gamma > .35\left(\frac{27}{4} F^2C\right)^{1/3}$ the maximum $e_f = \frac{F}{\gamma}$ and it occurs for $\Delta = -\frac{CF^2}{\gamma^2}$.

The importance of the higher harmonics was examined. It was concluded that for pump strengths of interest ($F \lesssim .0025$) the inclusion of the third harmonics gives waveforms that exhibit the level of wave steepening observed in simulations. We also argued from a simple-minded picture that the phase velocity of the plasma wave remains roughly constant. A nonlinear shift in κ arises along with the nonlinear shift in ω in such a way that v_ϕ is reasonably constant.

Next the issue of plasma inhomogeneities was addressed. We first examined how a single coherent ion wave $n = n_o(1 + \epsilon \sin \kappa_i x)$ couples energy from the primary wave $\left(\frac{\omega_o}{\kappa_o} = v_\phi = c\right)$ into other slow

waves $\left(\frac{\omega_o}{k_o \pm nk_i} < c\right)$. We found that this mechanism can lead to saturation levels of the primary wave below the relativistic saturation one if $\varepsilon > .5(F^2C)^{1/3}$. More details including thermal and kinetic effects are given by Darrow et al.[40,41] We discussed BWE in long wavelength density gradients. It was shown that if the electrons Lagrangian fluid excursion in the wave is small compared to the density scalelength, then the problem can be treated locally.

Last, the two-dimensional structure of the plasma wave was described. In particular, the modification to the structure of the focusing and defocusing fields from relativistic detuning was presented.

CHAPTER III. SIMULATIONS OF BEAT WAVE EXCITATION

IIIA. Introduction

In Chapter II the theory of Beat Wave Excitation was given. In this section we present simulation results that confirm and illuminate much of the theory. Although some numerical results will be presented, the bulk of this part will consist of results from particle-in-cell (PIC) kinetic[52] simulations. The kinetic simulations utilized the code WAVE, which is two-dimensional (2-space and 3-velocity components) and relativistic. Some of the details of WAVE can be found in Refs. 53 and 54. A partial list of the parameters used in the simulations is shown in Tables I and II.

The previous simulation studies[7,35,36] on the PBWA (prior to Refs. 5 and 15) were all one-dimensional (1-D). The 1-D simulations can be categorized into those in which the lasers are initialized over the entire system (Type I) or those where the lasers are launched into the system. The simulations in which the lasers are launched (Type II) can be further categorized into those where the lasers' rise time was or was not relevant. Type I simulations suffer from several limitations; therefore, they will not be discussed. These limitations are:

1. κ_p is fixed - In Type I simulations initial value problems are studied, i.e., time evolution problems. The pumps are initialized over the entire simulation box and then are allowed to evolve in time. The wavelength of the plasma wave, $2\pi/\kappa_p$, is

therefore forced to equal the wavelength of the ponderomotive force $2\pi/\Delta\kappa$. Consequently, the phase velocity of the plasma wave both decreases in time, as discussed previously in Sec. IIB4, and is artificial since the wavelength needs to be an integer number of simulation box lengths.

2. Pulse propagation effects are absent - In the PBWA it is crucial that one understands how the laser pulse evolves as it moves through the plasma. In Type I simulations this cannot be studied. The laser pulse changes as a result of the pump depletion-cascading phenomena. Periodic simulations can be useful for verifying the validity of approximations made in analytical treatments. However, in this case we opt for the use of aperiodic simulations where more effects can be studied at once.

The Type II simulation studies of BWE can be primarily found in Refs. 35 and 36. The latter[36] (also the first historically) used infinite mass ions and lasers with fast rise times. Their results are in excellent agreement with single particle theory and the envelope equation for the plasma wave. We note here, for the reader's benefit, that Sullivan and Godfrey[36] state that in their simulations the plasma wave does not saturate at the value given by Rosenbluth and Liu.[8] However, the formula given in Ref. 8 and quoted in Ref. 32 is in error because of an algebraic mistake. The simulations of Sullivan and Godfrey give results that agree with predictions from the correct formula.

The former[35] included simulations in which mobile ions and

lasers with longer rise times were used. Again, where comparison was permissible, agreement with single particle theory and the theory of relativistic saturation was observed. Additionally, it was shown that the predictions of the rise time theory given in Sec. IIB3 are borne out in the simulations. In what follows, for completeness, we review some of the 1-D simulations similar to those presented in Ref. 35 and also present other 1-D simulations that have frequency mismatches and/or density gradients and/or mobile ions.

In this section all variables are plotted in dimension units. For reference, these units are c/ω_p for position, ω_p^{-1} for time, $mc\omega_p/e$ for fields, and $\bar{n}_o$ for density.

IIIB. Results

IIIB1. Short Rise Time $\tau \leq t_s$

We begin with a simulation in which the lasers' rise time is negligible compared to the plasma wave's growth time. This is simulation I1 in Table I. The relevant parameters for beat wave excitation are $\frac{v_{os1}}{c} = \frac{v_{os2}}{c} = .03$ and $\omega_o = \omega_p$. The lasers' rise time is 25 ω_p^{-1} and the growth time is $\simeq 1.2x(4/F^2C)^{1/3} = 900\ \omega_p^{-1}$; so the rise time is a negligible fraction of the growth time. The time dependence for the lasers $\frac{v_{os}}{c}$ in the simulations is given for reference and it is

$$\frac{v_{os}}{c}(t) = \frac{v_{os}}{c}\left(\frac{6t^5}{\tau^5} - \frac{15t^4}{\tau^4} + \frac{10t^3}{\tau^3}\right) \equiv \frac{v_{os}}{c}\, h(t) \qquad (142)$$

where τ is the lasers' "rise time." Note that h(t) satisfies the properties that $h(\tau) = 1$, $h\left(\frac{\tau}{2}\right) = \frac{1}{2}$, and $\frac{dh}{dt}(\tau) = 0$. In Fig. 3a we present a plot of the the longitudinal electric field, E_x for the chosen coordinate convention, vs. position, x, at $\omega_p t = 320$. Since the laser packet, i.e., the driving force, propagates at the group velocity of light in a plasma, the envelope of all fields will predominantly be functions of the expression $x - v_g t \simeq x - ct$. The dependence of a field on positions at a fixed time is consequently straightforwardly related to the dependence of a field on time at a fixed position. As a result, from plots such as that given in Fig. 3a the growth rate for beat wave excitation may be inferred directly. The growth rate inferred from Fig. 3a is 2.02×10^{-4}, and this is close to the theoretical value of $(.03)^2/4 = 2.25 \times 10^{-4}$.

In Fig. 3b, E_x vs. x is plotted at a later time, $\omega_p t = 960$. In this figure the field is observed to saturate near the left-hand side of the simulation box. The peak amplitude of E_x in Fig. 3b is seen to be $\simeq .17(mc\omega_p/e)$, and this is very close to the theoretical value of

$$\left[\frac{16}{3}(.03)^2\right]^{1/3} = .168.$$

The theoretical value quoted refers to saturation from the relativistic nonlinear frequency shift, so we conclude that in the simulation relativistic effects dominate the saturation. That is, convection and collisions do not play much of a role. Furthermore,

TABLE I - 1-D

Name	$\alpha_1=\alpha_2$	$\omega_{1,2}$	τ	$\left(\frac{2\kappa T}{mc^2}\right)^{1/2}$	$\frac{M_i}{m_e}$	L_x	$\left(\frac{dN}{dx}\right)/N$	$\frac{T_i}{T_e}$
I 1	.03	10.9	50	.1	∞	410	∞	0
I 2	.1	5,4	120	.1	∞	120	∞	0
I 3	.1	5.2,4	120	.1	∞	25	∞	0
I 4	.1	5,4	120	.1	∞	25	∞	0
I 5	.1	4.98,4	120	.1	∞	100	∞	0
I 6	.1	4.98,4	120	.1	∞	25	∞	0
I 7	.1	5.4,5	120	.1	∞	120	∞	0
I 8	.14	5,4	300	.1	∞	100	∞	0
I 9	.4	5,4	300	.1	∞	100	∞	0
I 10	.56	5,4	300	.1	∞	100	∞	0
I 11	.56	5,4	300	.1	1836	60	∞	0
I 12	.03	10,9	1000	.1	1836	410	∞	1.3
I 13	.03	5,4	50	.06	100	120	600	.2
I 14	.03	5,4	50	.06	∞	120	600	.2
I 15	.1	5,4	300	.03	∞	100	∞	0
I 16	.1	5,4	300	.03	1836	100	∞	0
I 17	.1	5,4	300	.03	400	100	∞	0
I 18	.05	5,4	150	.03	1836	100	∞	0
I 19	.1	5,4	300	.03	1836	100	∞	0
I 20	.03	5,4	50	.06	100	120	∞	.2
I 21	.03	5,4	50	.06	100	120	∞	.05
I 22	.03	5,4	50	.06	1836	120	∞	0

I 23	.1	5,4	25	0	∞	100	ripple	0
I 24	.03	5,4	1000	.06	1836	410	∞	1.3

TABLE II - 2-D

Name	α	L_o	$\omega_{1,2}$	τ	$\left(\frac{2\kappa T}{mc^2}\right)^{1/2}$	$\frac{T_i}{T_e}$	$\frac{M_i}{m_e}$	L_x	L_y
II 1	.1	∞	3,3	240	.06	1	∞	100	20
II 2	.1	∞	3,3	240	.06	1	1836	100	20
II 3	.4	∞	4,4	120	.1	1	∞	120	20
II 4	.4	∞	5.4	120	.1	1	∞	120	20
II 5	.7	∞	3.8,3.8	1000	.1	1	∞	200	10
II 6	1	∞	4.29,3.29	1000	.1	1	∞	200	10
II 7	.56	20	5,4	300	.1	1	∞	60	60
II 8	.56	20	5,4	300	.1	1	1836	60	60
II 9	.56	20	5,4	300	.1	1	1836	120	30
II 10	.56	30	5,4	300	.1	1	∞	60	60
II 11	.56	40	5,4	300	.1	1	1836	60	60
II 12	.56	40	5,4	800	.1	1	1836	60	60
II 13	.28	40	5,5	800	.1	1	1836	60	60
II 14	.56	40	5,5	800	.1	1	1836	60	60
II 15	.56	40	5,5	150	.03	1	1836	60	60
II 16	.56	40	5,4	150	.03	1	1836	60	60
II 17	.14	40	5,4	300	.1	1	1836	60	60
II 18	.14	40	5,4	pulse	.1	1	1836	60	60

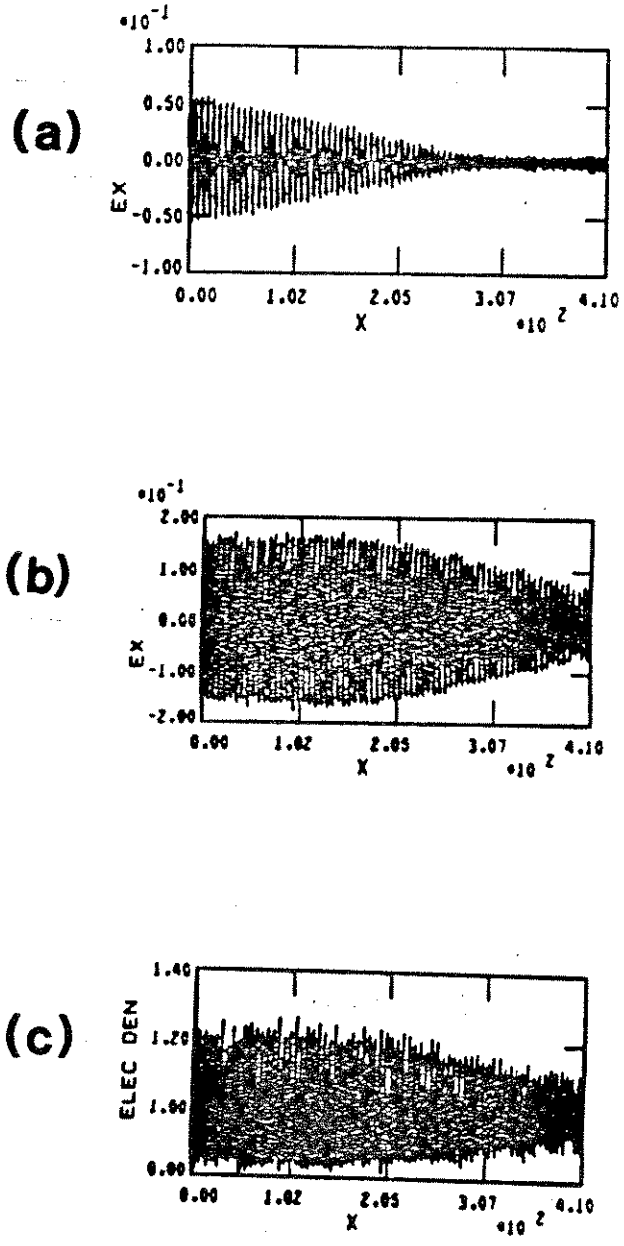

Figure 3. The longitudinal electric field E_x vs. position x for $\alpha_1 = \alpha_2 = .03$ at (a) $\omega_p t = 320$ and (b) $\omega_p t = 960$. (c) The electron density N vs. x at $\omega_p t = 960$.

by inferring the time dependence of E_x from the spatial dependence given in Fig. 3b, we estimate the time at which saturation occurred to be $\simeq 850\ \omega_p^{-1}$. To obtain a reasonable estimate of the saturation time, we subtract half the lasers' rise time from the time of saturation, and this is 840 ω_p^{-1}. This compares favorably to the analytical estimate of 915 ω_p^{-1} obtained earlier. The envelope equations when integrated yield a saturation value of .163 at $\omega_p t_s \simeq 940$. The saturation time measured from the simulation is smaller than the theoretical and numerical values. We believe a plausible explanation for this discrepancy is as follows. The derivation for the saturation time given in Ref. 9 neglects, among other things, cascading. If cascading does occur, then the first lower (higher) frequency cascaded light wave together with the high (low) frequency pump could, as shown in Appendix B, contribute an additional driving force for the plasma wave. This, in addition to the conventional cascaded modes, may cause $\dot{\phi}$ to increase faster (convection seems negligible).

We also plot the Fourier $\vec{\kappa}$ spectrum for the longitudinal electric field energy $\frac{E_x^2}{8\pi}$ at $\omega_p t = 960$ and this is shown in Fig. 4. At this point in time the field is reasonably uniform in space. We can, therefore, draw conclusions from Fig. 4 about the ratio of the various harmonics of the plasma wave. The ratio between the second and first harmonics inferred from Fig. 4 is 8×10^{-2}. Recall from Sec. IIB5 that the theoretical ratio is $e_1/e_0 = (1/2)e_0$, which for this case is $\simeq 8.4 \times 10^{-2}$ (the E fields are normalized to $mc\omega_p/e$), so there is once again excellent agreement between the simulations and

the analytic work. The theoretical ratio of the second and first harmonics for the electron density is $n_1/n_0 = e_0$ (densities are normalized to the background density $\bar{n}_0$), which implies that harmonics are more prevalent in the density than in the electric field. Although not shown, the ratio of n_1/n_0 in the simulation is indeed e_0. As discussed in Sec. IIB5, this and the fact that the first and second harmonics are in phase means that the nonlinearity of a wave is more noticeable visually in a real space density plot than a real space electric field plot. We present in Fig. 3c a plot of the density vs. x for future reference. The wave looks sinusoidal since the wave amplitude is small. In a moment, on the other hand, we will present results from a run where the electric field appears sinusoidal while the density is clearly not (for real space plots).

We next present results from simulation I2 in Table I, in which

$$\frac{v_{os1}}{c} = \frac{v_{os2}}{c} = .1, \quad \frac{\omega_{1,2}}{\omega_p} = 5, \ 4, \text{ and } \left(\frac{2\kappa T_e}{mc^2}\right)^{1/2} \equiv a_e = .1.$$

The lasers' rise time is 120 ω_p^{-1} while the growth time is

$$> 1.2\left(\frac{4}{F^2 c}\right)^{1/3} = 180\ \omega_p^{-1}.$$

The greater-than inequality used in the previous sentence is used because the quoted formula was derived assuming there was no rise time. Whereas in the simulation discussed previously the rise time was negligible when compared to the beat wave growth time, in

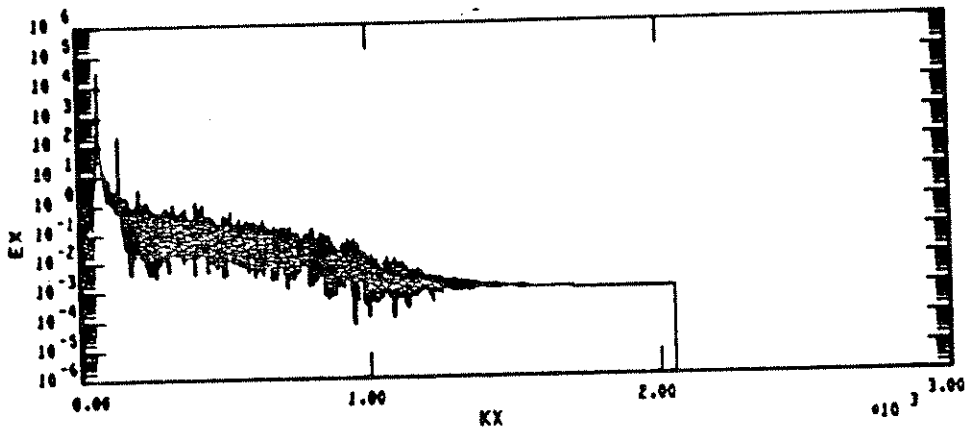

Figure 4. The Fourier spectrum of the longitudinal field energy $E_x^2/8\pi(\vec{\kappa})$ at $\omega_p t = 960$. κ is in units of mode number, $2\pi/L_x$.

this simulation the lasers' rise time is a considerable fraction of the growth time. We will show, nevertheless, that for this case the peak amplitude is basically only a function of the F at the time of saturation, as argued in Sec. IIB3.

We first integrate Eqs. (59) and (60) for the simulation parameters. The time evolution for the plasma wave amplitude e_o is shown in Fig. 5a. The peak amplitude is .424. Since $\omega_o = \omega_p$ and not $\omega_{BG} \equiv \left(\omega_p^2 + \frac{3}{2}\kappa^2 a_g^2\right)^{1/2}$, then $\Delta_o \simeq -\frac{3}{4}a_g^2 = -.0075$. Using Eq. (30), which is derived assuming a constant F, we find an $e_m = .423$. Clearly, the existence of a rise time has had a negligible effect on e_m as argued in Sec. IIB3. The saturation time in Fig. 5a is seen to be $\simeq 270\omega_p^{-1}$. As expected, this is slightly larger than t_s found from $.423 = \int_o^{t_s} dt\ f(t)$.

We now compare the PIC simulation results to the analytical and numerical results. The longitudinal field E_x is plotted vs. x in Fig. 5b at $\omega_p t = 240$. Although plotted vs. x, as before, we discuss the figure as though the axis is time. The lasers are at their peak amplitude over the entire plot since the lasers' rise time is $120\omega_p^{-1}$ and $L_x = 120\frac{c}{\omega_p}$. It then follows that, since at $\omega_p t = 120$ the ponderomotive force and the plasma wave are still in phase ($\sin\phi \simeq 1$), linear growth should be observed from the right-hand side of the plot. The measured growth rate is $\simeq \frac{.30}{120} = .0025$, which is precisely the analytical value $\frac{\alpha_1\alpha_2}{4}$. Furthermore, the envelope equations predict that $\dot{e}_o = F \sin\phi$; so as the mismatch (ϕ) gets larger the growth rate should decrease as observed in Fig. 5a. However, in Fig. 5b it is clear that near the center of the

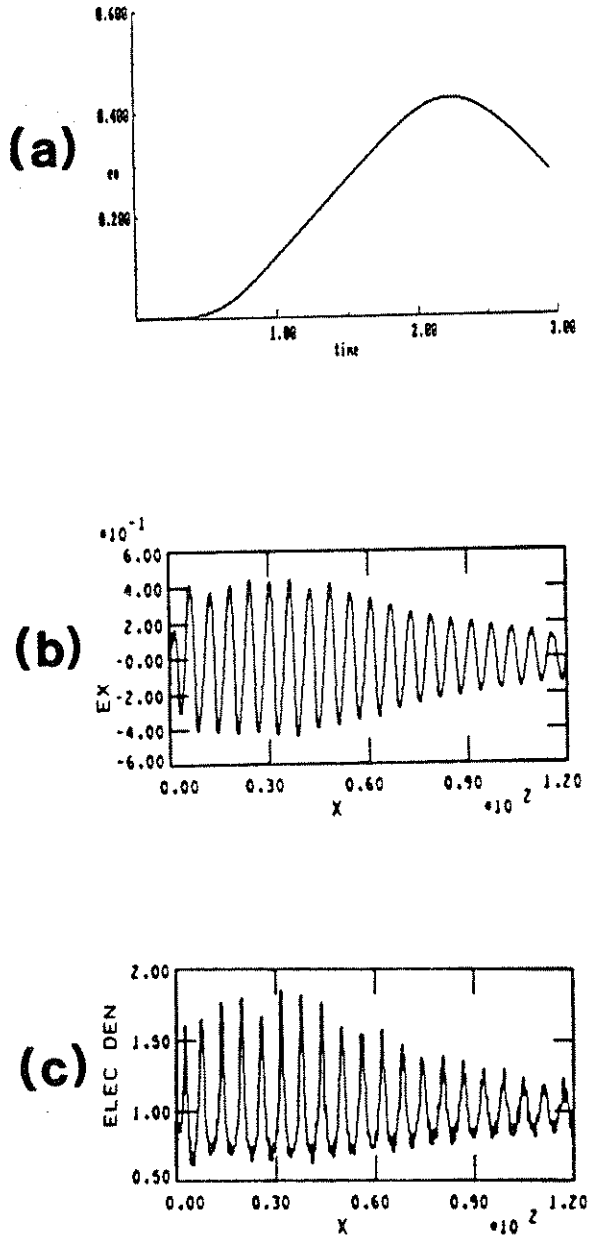

Figure 5. (a) The value of $e_o(t)$ obtained from the envelope equations for $\alpha_1 = \alpha_2 = .1$, $\Delta_o = -.0075$, and $\tau = 120\omega_p^{-1}$. Time is measured in units of τ. The (b) electric field E_x vs. x and the (c) electron density N vs. x for the same parameters at $\omega_p t = 240$.

simualtion box, or $\omega_p t \simeq 180$, the observed growth rate actually begins to increase.

There are several possible causes for the increase of the growth rate. The first, and in this case we believe the most important, is the modification of the driving force from cascading including the $\Delta\omega = 2\omega_p$ instability alluded to earlier (Appendix B). At the left-hand boundary (the boundary where the lasers enter) no pump depletion and no cascading occur so the beat wave growth occurs according to the input F. As the light propagates into the plasma, it cascades into upper and lower sidebands, thereby modifying the driving force at a fixed position. The growth rate inferred from the spatial plot will therefore not follow the growth rate of E_x at the left-hand boundary. From Fig. 5b we speculate that cascading, including the $\Delta\omega = 2\omega_p$ terms, can at times increase the driving force.

The second possibility results from the harmonics of the plasma wave. The amplitude derived in Sec. IIB5 when harmonics are included is

$$E \simeq e_0\left(1 + \frac{23}{64}\, e_0^2\right).$$

It then follows that

$$\frac{dE_x}{dt} = \frac{de_0}{dt}\left(1 + \frac{69}{64}\, e_0^2\right) .$$

Therefore, the growth rate will appear larger by the factor

$\left(1 + \frac{69}{64} e_0^2\right)$, which for the parameters of the simulation is ≃1.1. The 10 percent increase is small compared to the observed increase of ≃100 percent in this simulation.

The numerical work is also not in agreement with the PIC results for the saturation time. The simulations give $\omega_p t_s$ = 210, which is much less than the $\omega_p t_s$ = 270 obtained from the numerical result. This discrepancy is qualitatively consistent with an effective increase in the driving force resulting from cascading, including the $\Delta\omega = 2\omega_p$ terms.

On the other hand, the peak values for the electric field obtained from the envelope equations and the PIC simulation are in agreement. For the e_m obtained from the envelope equations the predicted value of E_m is $\simeq e_m\left(1 + \frac{23}{64} e_m^2\right)$ = .46. From the simulation the peak E_x seen in Fig. 5b is .44, which is in excellent agreement with the numerical results.

In Fig. 5c we plot the electron density vs. x to demonstrate the importance of the second harmonics to the electron density. The second harmonics produce an asymmetry in the density with respect to the background density. This is to be compared with Fig. 3c where the density still appears sinusoidal. Note that the minimum value of N is larger than $-\bar{n}_0/2$ as predicted in Sec. IIB5.

IIIB2. Long Rise Time $\tau \gg t_s$

In this section we present results obtained from simulations with parameters that result in saturation during the rise time of the lasers. As it turns out, this is the more relevant case for

current experimental situations.

We begin with simulation I8 from Table I in which

$$\frac{v_{os2}}{c} = \frac{v_{os2}}{c} = .4, \quad \frac{\omega_{1,2}}{\omega_p} = 5,4(\Delta\omega = 1), \quad \left(\frac{2\kappa T_e}{mc^2}\right)^{1/2} = .1, \text{ and the}$$

lasers' rise time is $\tau = 120\ \omega_p^{-1}$. Once again for comparison to the PIC results we integrate Eqs. (59) and (60) and the resulting plot for e_o vs. t is given in Fig. 6a. The first peak occurs at $\omega_p t = 91$ with a value of $e_o = .768$. The analytical expressions (78a) and (78b) predict an $e_o = .723$ at $t_s = 92\omega_p^{-1}$. This is in remarkable agreement considering that expressions (78a) and (78b) were derived with $\Delta = 0$ and an approximate form for F(t). If Eq. (75) is solved directly, then as expected even better agreement between the analytical and numerical work is obtained.

The corresponding E_x vs. x plot at $\omega_p t = 120$ from the PIC simulation is presented in Fig. 6b. Since E_x not e_o is being plotted, the peak value for E_x in Fig. 6b as predicted from the numerical and analytical work should be $E_x \simeq .923$. However, the peak value attained in Fig. 6b is $\simeq .75$, substantially below the theoretical value. This is probably due to the fact that for such large values of F and e_o the expansion in v^2/c^2 in Part I breaks down. The inclusion of the higher-order terms would lead to smaller driving forces. In addition, wave particle interactions (beam loading) and pump depletion also lower the value of e_m.

We also plot the electron density N vs. x at the same time in Fig. 6c. Once again we emphasize the asymmetry in the density

(a)

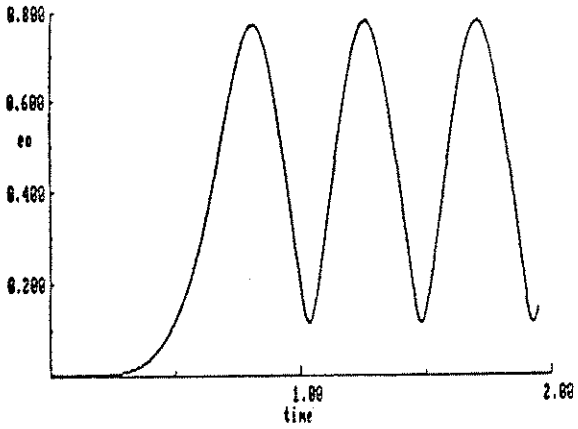

(b)

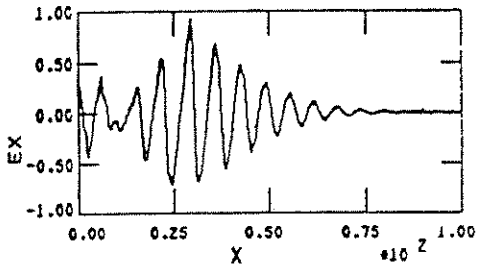

(c)

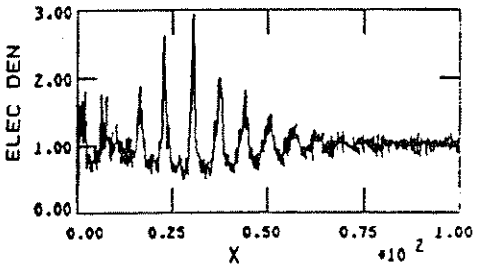

Figure 6. (a) The integration of the envelope for $\alpha_1 = \alpha_2 = .4$, $\Delta_o = -.0075$, and $\tau = 120\ \omega_p^{-1}$. Time is measured in units of τ. The (b) electric field E_x vs. x and the (c) electron density N vs. x for the same parameters at $\omega_p t = 120$.

about $\bar{n}_o = 1$. If we sum the first four harmonics of N for $n_o = e_o = .73$ we obtain

$$N = 1 + e_o + e_o^2 + \frac{27}{64} e_o^3 = 2.42. \tag{143}$$

This is below the value of 2.7 found from the simulations. The difference points out the necessity of using Nobles asymptotic treatment[22] for large plasma wave amplitudes. The value for N obtained from expansion (143) is sensitive to the value of e_o for large fields. This makes comparison difficult when the value of e_o cannot be determined accurately.

Rather than discuss the other 1-D simulations in Table I for which $\omega_o = 1$ in regards to beat excitation, we just mention that in each case the analytical work agreed with the numerical work; while in the simulations the presence of cascading, pump depletion, and particle trapping and harmonics did not lead to any striking differences.

IIIB3. $\underline{\Delta \neq 0}$

It was shown in Sec. IB2 that if the frequency difference of the two lasers $\omega_1 - \omega_2 \equiv \omega_o \neq 1$, then the peak amplitude e_m of the plasma wave is altered from $(4F/C)^{1/3}$. This was first described by Tang et al.[9] and it was reviewed in Sec. IB2. When $\omega_o - \omega_{BG} \equiv \Delta < 0$ (but not too negative) the peak amplitude can be larger than $(4F/C)^{1/3}$ since, as discussed in detail in Appendix A, the nonlinear frequency shift is negative. The converse is also true,

that if $\Delta > 0$ then $e_m < \left(\frac{4F}{C}\right)^{1/3}$. In the previous section simulation results were already presented for $|\Delta| << |\Delta_c| \equiv \left(\frac{27}{2}F^2C\right)^{1/3}$. (Those Δ's are due to the Bohm Gross correction.) We next present results from simulations that further support the conclusions of Tang et al.

To isolate the mismatch effects, we let the laser rise time τ be smaller than the saturated time t_s. In Fig. 7b we plot E_x vs. x at $\omega_p t = 240$ from simulation I3 in Table I. The relevant parameters are

$$\frac{v_{o1}}{c} = \frac{v_{o2}}{c} = .1,\ a_e \equiv \left(\frac{2\kappa T_e}{mc^2}\right)^{1/2} = .1,\ \omega_{1,2} = 5.02,4,\ \text{and}\ \tau = 120.$$

Note that except for ω_1 the parameters are identical to those of simulation I2. We infer from the same plot at other times that the electric field in Fig. 7b has already attained its peak amplitude. The maximum value for E_x in Fig. 7b is $\simeq .24$. We ignore the large anomolous peak at the right-hand boundary since it is probably the result of the boundary condition. At this value of E_x, the importance of the harmonics is negligible. If in formula (30) we use $\Delta = \omega_o - \omega_{BG} + F = .015$, then we find $e_m = .25$. Furthermore, if Eqs. (59) and (60) are integrated we find $e_m = .238$ as shown in Fig. 7a. The saturation time in Fig. 7a is slightly less than 240 ω_p^{-1} and this agrees with the particle simulation. Clearly, all three methods are in excellent agreement.

We next present results from simulation I5 in Table I where the parameters are identical to those of simulation I2 except $\omega_1 = 4.98$. In this simulation there is now a negative frequency mis-

(a)

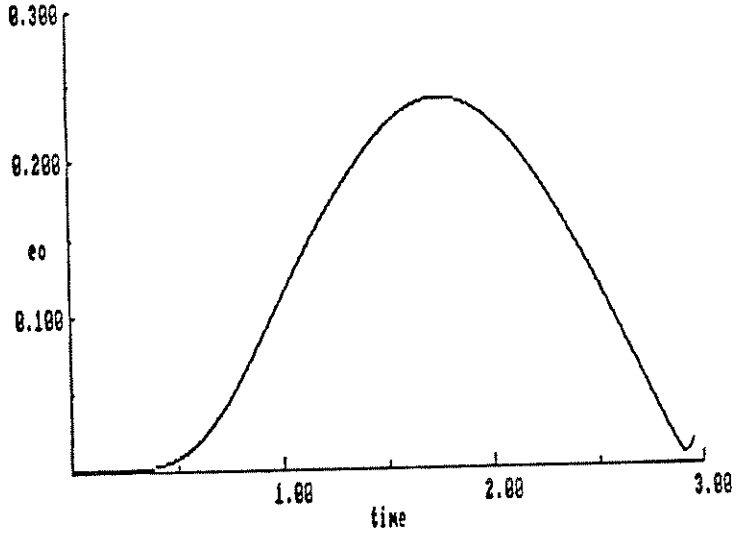

(b)

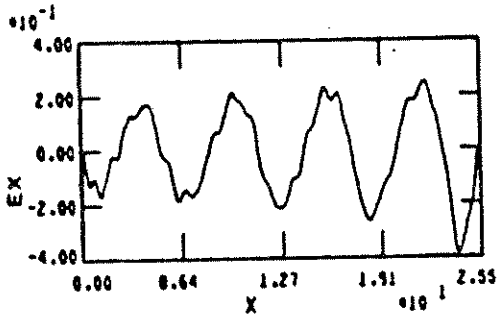

Figure 7. (a) The value of $e_0(t)$ obtained from the envelope equations for $\alpha_1 = \alpha_2 = .1$, $\Delta_0 = .0125$, and $\tau = 120\omega_p^{-1}$. Time is measured in units of τ. (b) The electric field E_x vs. x for the same parameters at $\omega_p t = 240$.

match. The value of $\Delta_o = -.0275$ (the Bohm Gross shift is $-.0075$); and the value for Δ at saturation, if it occurs after the rise time, will be $\Delta = \Delta_o + F \simeq -.025$. This case is interesting because if we integrate Eqs. (59) and (60) with $\Delta_o = .0275$ we find $e_m \simeq .28$. This is shown in Fig. 8a. This indicates that the mismatch is too negative. The simulations contradict this, as shown in Fig. 8c where we plot E_x vs. x at $\omega_p t = 320$. The amplitude at this time is $\simeq .55$. We note that the electric field is flatter for the negative peaks. This is due to the trapped electrons extracting energy from the plasma wave (beam loading). With this additional complication, it is difficult to determine the actual value for the peak electric field. Furthermore, the wave is still growing at this time and later in time it becomes even more difficult to determine a definitive value for e_m. Clearly though, the wave evolution is consistent with a negative nonlinear frequency shift. The amplitude is initially smaller and is eventually larger than for the zero mismatch case.

We plot in Fig. 8b the evolution of e_o obtained by integrating Eqs. (59) and (60) for $\Delta_o = -.025$. We plot e_o for this value of Δ_o since it yields good agreement. The peak value is $e_m \simeq .58$ and it corresponds to $\omega_p t = 390$. The rise time is evidently important since it alters the optimum value of Δ_o, albeit slightly. Although the simulation and the numerical work do not agree quantitatively, they do agree qualitatively in that the E_m is larger for a negative mismatch (but not too negative).

We have also carried out simulations with a larger positive fre-

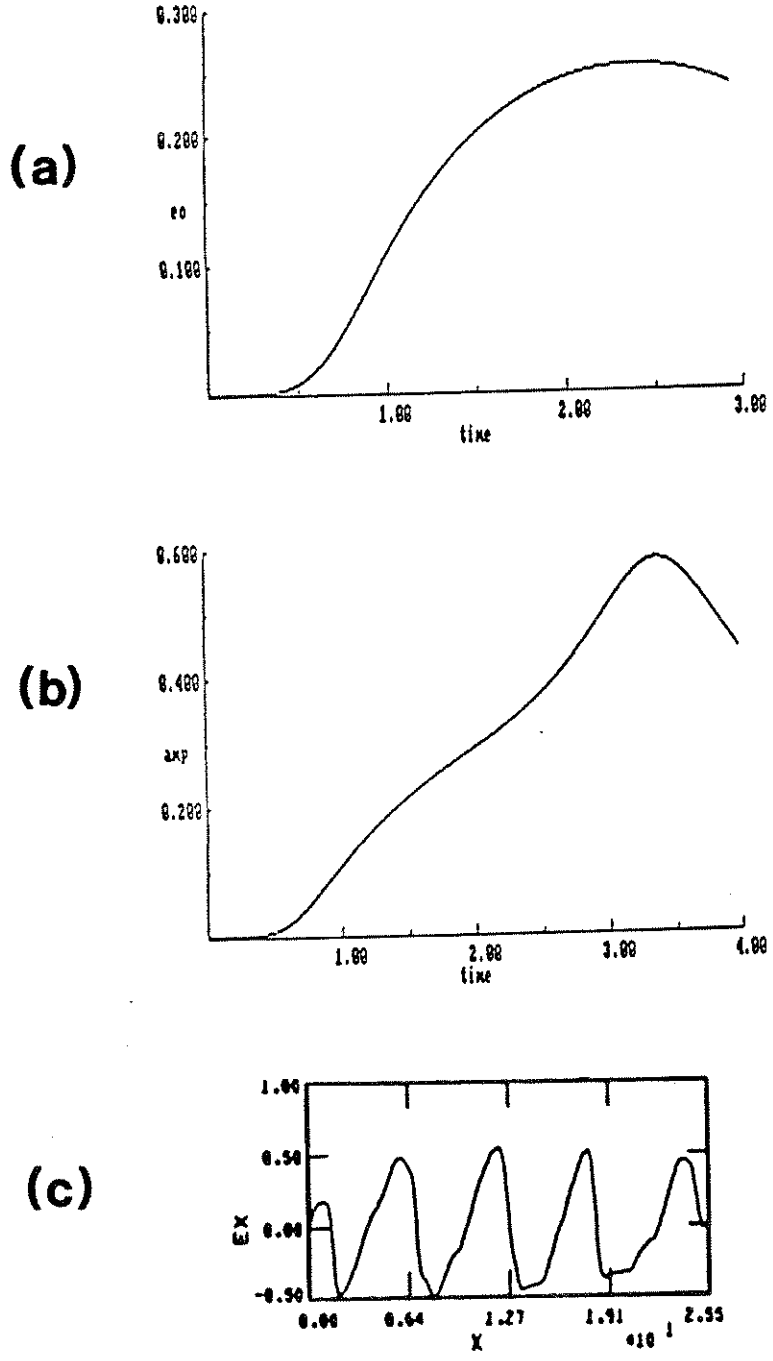

Figure 8. The value of $e_o(t)$ obtained from the envelope equations for $\alpha_1 = \alpha_2 = .1$, $\tau = 120\omega_p^{-1}$, and (a) $\Delta_o = -.0275$ and (b) $\Delta_o = -.025$. Time is measured in units of τ. (c) The electric field E_x vs. x for the same parameters at $\omega_p t = 320$.

quency mismatch $\Delta \simeq .3\omega_p$. This is simulation I7 in Table I. The results are not presented here since agreement with the tuning curve of Tang et al. is essentially observed.

IIIB4. Density Gradient

In Section IIB7 we investigated the effects of plasma inhomogeneity analytically. In this section we present results from complementary simulations. We begin with a simulation of a plasma with a long scalelength density gradient. The parameters for simulation I12 in Table I are

$$\frac{v_{os1}}{c} = \frac{v_{os2}}{c} = .03,\ \omega_{1,2} = 5,4,\ \left(\frac{2\kappa T_e}{mc^2}\right)^{1/2} = .0625,\ \tau = 50, \text{ and } \left(\frac{dn}{dx}/n\right)^{-1} = 600\ \frac{c}{\omega_o} \text{ at the point where } \omega_o = \omega_p.$$

The density rises from .036 to .044 of the critical density of the high-frequency laser in a distance $120\ \frac{c}{\omega_o}$.

We plot the electron density N vs. x at $\omega_p t = 468$ in Fig. 9a and the associated electric field E_x vs. x at $\omega_p t = 468$ in Fig. 9b to show that, as expected qualitatively, the plasma wave is localized around the resonant region. The density is plotted in units of $\frac{\omega_p^2(x)}{\omega_o^2}$. In this simulation the resonant region, i.e., where $\omega_p(x) = \omega_{BG} \simeq \omega_o$, is near the center of the simulation box. For reference the position where $\Delta = 0$ is $x = 56.6\ \frac{c}{\omega_o}$ and the position where $\Delta = -\left(\frac{27}{2}\ F^2 c\right)^{1/3}$ is $x = 66\ \frac{c}{\omega_o}$. The resonant point $\Delta = 0$ is marked in Fig. 9.

In Sec. IIB7 it was shown that if $\xi \ll L_S \equiv [(dN/dx)/N]^{-1}$ then

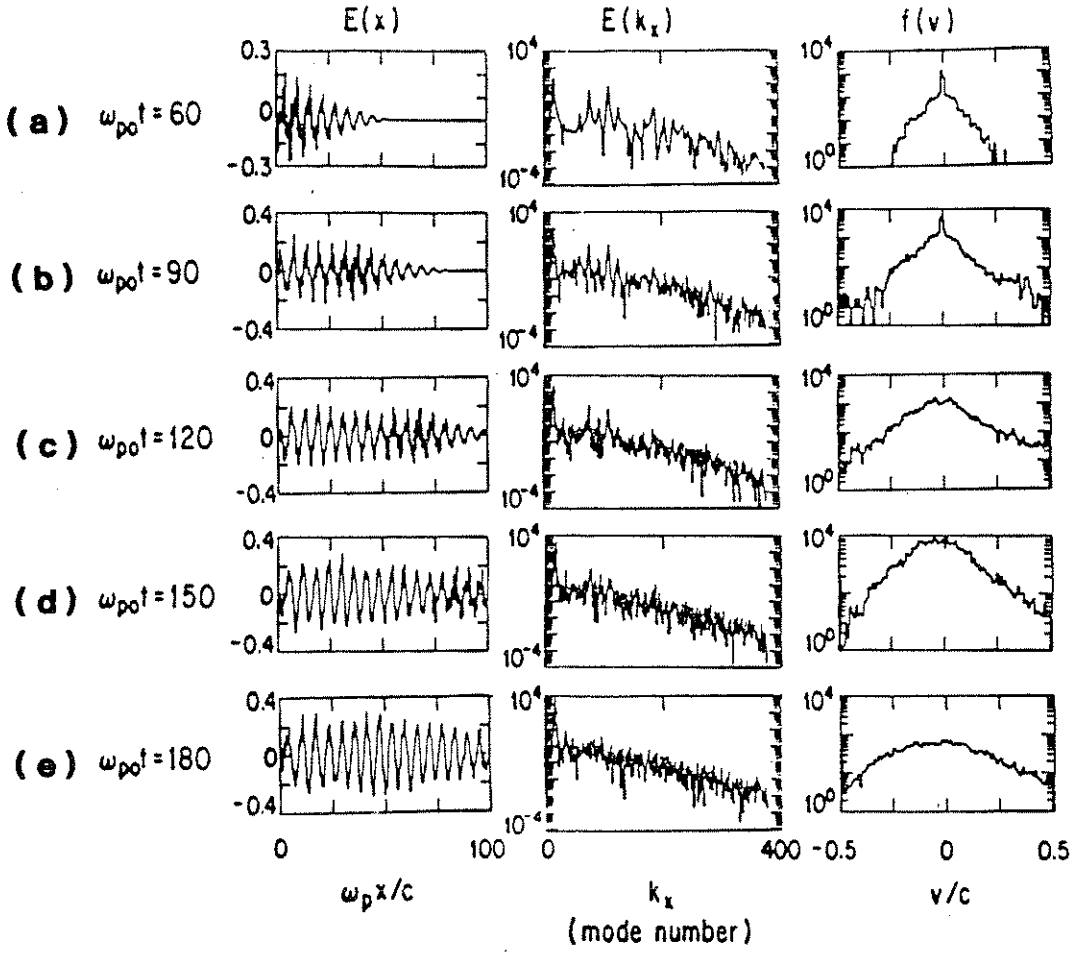

Figure 9. (a) The electron density N vs. x at $\omega_p t$ = 468. The absolute value of the electric field E_x vs. x at (b) $\omega_p t$ = 468, (c) $\omega_p t$ = 720, and (d) $\omega_p t$ = 960.

the excitation could be treated locally. For this simulation L_s is $\frac{120}{.2} = 600\ \frac{c}{\omega_o}$. Since ξ is bounded by $\frac{c}{\omega_o}$ (for $\xi\ \frac{\omega_o}{c} > 1$ wavebreaking occurs), then $\frac{\xi}{L_s} < \frac{1}{600} << 1$. The excitation process should, therefore, occur locally enabling some quantitative comparisons with the tuning curves of Tang et al. The convection terms arising because of the finite temperature will become important when the plasma wave evolves in time into a more localized structure in space. It also follows that a determination of the sign of the nonlinear frequency shift can be made by observing on which side (in x) of the resonant point $\omega_p(x) = \omega_o$ the plasma wave amplitude is eventually largest.

The plasma wave amplitude is asymmetric with respect to $x = 60\ \frac{c}{\omega_o}$ at $\omega_o t = 468$ as shown in Fig. 9b. At this early time relativistic detuning is ineffectual. The change in sin ϕ from 1 (ϕ from $\frac{\pi}{2}$) is consequently determined solely by the initial mismatch. Since the initial mismatch is an odd function with respect to the resonant point and sin ϕ is an even function about $\phi = \frac{\pi}{2}$, the plasma wave amplitude is symmetric about the resonant point. At later times, however, relativistic detuning leads to an asymmetrical dependence of sin $\phi(x)$ about $x = 60\ \frac{c}{\omega_o}$. This is shown in Fig. 9c where the absolute value of the longitudinal electric field is plotted for $\omega_o t = 720$. At this time the peak value for E_x is $\approx .16$ and it exists at a position to the right of $x = 60\frac{c}{\omega_o}$. Hence, the plasma wave is getting out of phase with the pump fastest at positions where $\omega_p < \omega_o$ ($\Delta > 0$). We conclude, therefore, that the nonlinear frequency shift is negative for the reasons given earlier.

As the plasma wave continues to evolve in time it becomes more localized in space. Eventually a time occurs when at a given position the electric field reaches its maximum value and then begins to decrease. These positions of instantaneous saturation gradually move toward the Tang et al. resonant point both from the high density and low density side while the center of the packet continues to grow. This scenario results in the evolution to the narrow localized structure.

This is depicted in Figs. 9b, 9c, and 9d where the absolute value of E_x is plotted vs. x at three times: $\omega_o t = 468$, $\omega_o t = 720$, and $\omega_o t = 960$. The maximum E_x at $\omega_o t = 960$ is $\simeq .1875$. The amplitude above the Rosenbluth and Liu value of $\left(\frac{4F}{C}\right)^{1/3}$, and the time $\omega_o t = 960$ is less than the saturation time $\omega_p t_s \simeq 1.2 \left(\frac{4}{F^2 C}\right)^{1/3}$ for a rise time of $50\omega_p^{-1}$ and a delay time of $60\omega_o^{-1}$. This means that ϕ has been nearly $\frac{\pi}{2}$ for the entire run at this position. It is not possible to make further quantitative comparisons because convection losses are now becoming important. The convection term is $v_g \frac{\partial}{\partial x} \simeq \frac{3}{2} a_e^2 \frac{e_o}{\Delta L}$ where ΔL is a typical scalelength for e_o. At $\omega_p t = 960$, $\langle e_o \rangle \simeq .1$, and $\Delta L \simeq 5 \frac{c}{\omega_o}$, so $v_g \frac{\partial e_o}{\partial x} \simeq 1.26 \times 10^{-4}$ while $F \sin \phi \simeq 2.25 \times 10^{-4}$. Consequently, convection terms are on the same order as the driving force. So, as the wave increases the approximation of treating the problem locally breaks down not because of a nonlinear effect but because of linear convection.

Last, we note that the qualitative shape of the tuning curve of Tang et al.[9] is evident in the plots of Figs. 9b through 9d. The wave's envelope falls off more sharply on the high density side

than on the low density side. The high density side corresponds to negative mismatches.

IIIB5. Density Ripple

It was shown in Sec. IIB7 that in the presence of a coherent density ripple the maximum amplitude of the plasma wave can be reduced below the Rosenbluth and Liu value. The plasma was assumed to have zero temperature. We have presented theory and numerical work elsewhere[40,41] to describe the modifications to the cold theory when a finite temperature fluid plasma is considered. In this section we describe a particle simulation that illustrates how kinetic effects alter the conclusions of the cold and warm fluid theories. Several simulations were made and the complete description can be found in Ref. 41.

We report on simulation I24 in Table I. The relevant parameters are $\frac{v_{os}}{c} = .05$, $\frac{\omega_{1,2}}{\omega_p} = 5,4$, and $N = \bar{n}_0[1 + .1 \sin(1.2 \kappa x)]$ where κ is the wave number of the density ripple. The electrons are initialized with no thermal motion. The wavenumber of the ripple was chosen so that it would not be the same as any Raman Scattered modes. The laser rise time is short and the plasma heats up quickly before the grid instability can grow. An upper bound for this numerical instability is $\sim .015\omega_p$.[52] The results are depicted in Fig. 10 where a sequence of E_x vs. x, $\frac{E_x^2}{8\pi}$ vs. k_x, and $f(p_x)$ are presented. As the plasma wave is excited, there is evidence of the first two coupled modes ($\kappa_o \pm \kappa$, $\kappa_o \pm 2\kappa$). This is seen in both the E_x vs. x and $\frac{E_x^2}{8\pi}$ vs. k_x plots at $\omega_p t = 60$. The

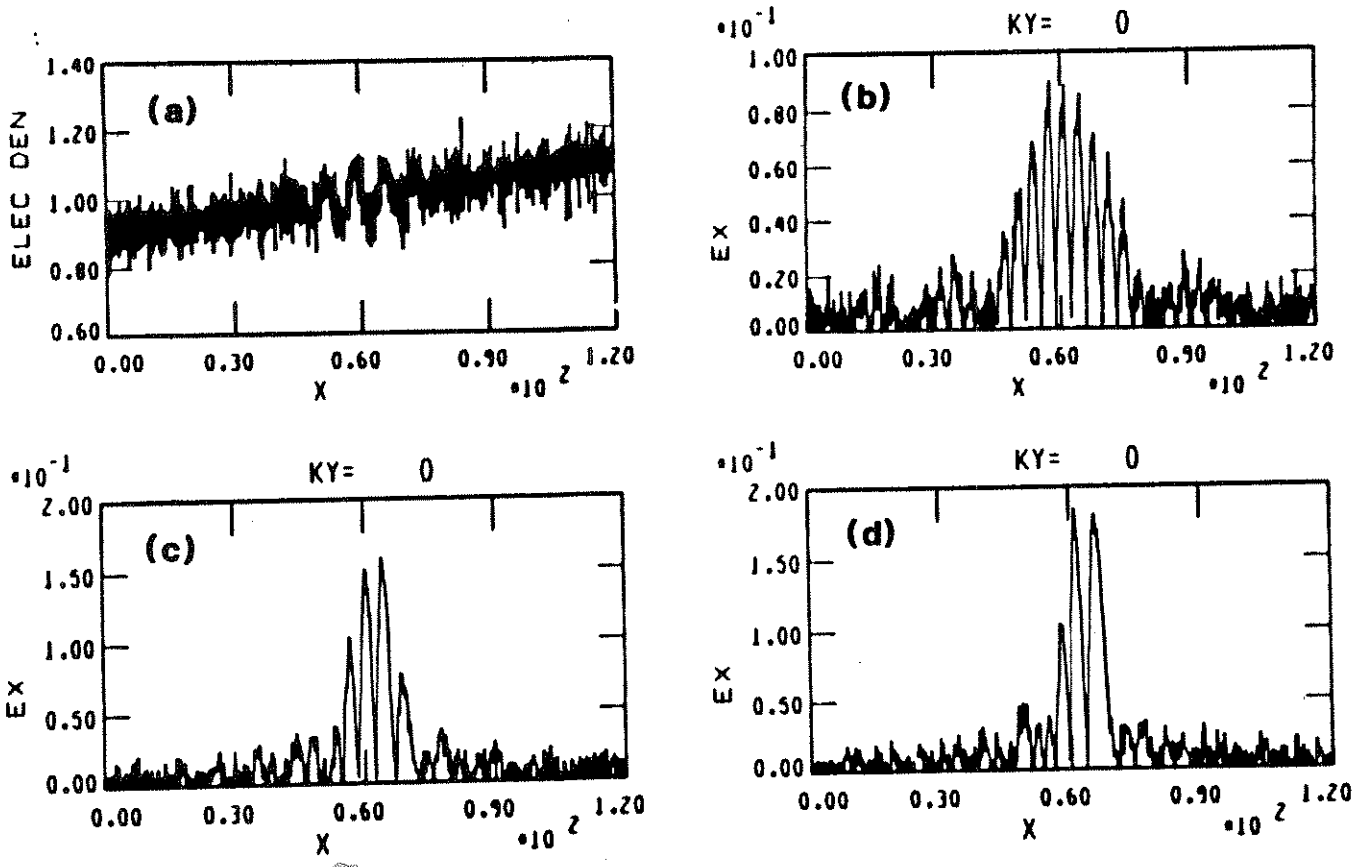

Figure 10. Plots of $E_x(x)$, $(E_x^2/8\pi)k$, and $f(p_x)$ at (a) $\omega_p t = 60$, (b) $\omega_p t = 90$, (c) $\omega_p t = 120$, (d) $\omega_p t = 150$, and (e) $\omega_p t = 180$ from a simulation with $\alpha_1 = \alpha_2 = .05$, and $N = \bar{n}_o \{1 + .1 \sin[1.2(24)^{1/2}x]\}$. The electrons were initialized with no thermal motion.

electric field looks hashy toward the left-hand boundary at both times. At $\omega_p t = 90$, the plasma wave looks smooth toward the left while it is still hashy in the center of the simulation box. This is accompanied by electron heating as illustrated in the $f(p_x)$ plot at the same time. The heating is mostly on the left and is the result of wavebreaking of the highest κ modes and damping from wave-particle interactions of the intermediate κ modes. As time progresses further, the hashy part propagates to the right leaving behind a hot plasma as evidenced by the continued expansion in $f(p_x)$. This is seen in Fig. 10c where $E_x(x)$, $\frac{E_x^2}{8\pi}(k)$, and $f(p_x)$ are presented at $\omega_p t = 120$. Eventually the entire plasma is heated and the mode coupling ceases. The quenching of the mode coupling can be described with the inclusion of the finite temperature terms.[41] This is illustrated in Fig. 10d and 10e where the same plots are shown at $\omega_p t = 150$ and 180. The plasma wave eventually resembles that from uniform density simulations after the disappearance of mode coupling. The heating of the plasma from the higher k mode-coupled modes appears to be a self-stabilization method.

More details and discussion of this and other simulations can be found in Darrow et al.[41] The effects of electron transport in more realistic geometries and ion inertia need more study. Recently, Dubois et al.[55] have examined the role of collapse in BWE; however, their work is still preliminary. Last, we mention that mode coupling has been observed in the recent beat wave experiments and details can be found in Refs. 40, 41, and 56.

IIIB6. Discrete Ions

In the previously discussed simulations the ions constituted a smooth fixed background of neutralizing charge. If instead the ions are particles, then the excitation process can be altered in two ways.

The first is due to the ions' discreteness, while the second is due to their dynamics. The latter point will be addressed in Chapter V where the instabilities arising from ion dynamics are examined using simulations. We next briefly report on simulation results that investigate the former.

The results are qualitative. A more quantitative analysis will be given at a later date. In the simulations when the ions are fixed, they constitute a smooth background density. When they are mobile, they are also discrete and this gives rise to larger background density fluctuations. The amplitude of the fluctuations depends on the number of particles per cell and their temperature. The effect of ion fluctuations has been examined analytically by Dawson and Oberman[43] and by Horton and Tajima.[46] This was briefly discussed in Sec. IIB7. In this section we describe simulations with differing ion temperatures and ion mass in which the plasma wave sometimes does not grow. It appears that sometimes the ion inertia is not a factor, just the amplitude of the background noise. If this is the case, then the final expression for the damping given by Horton and Tajima[46] needs to be reevaluated since they assumed the damping rate was smaller than the ion wave

frequency.

The simulations to be described are I1, I12, I22, and I23 in Table I. Simulation I1 was presented earlier to illustrate BWE. The ions were a smooth neutralizing background in this simulation. In simulation I22 the parameters are similar except the ions are discrete with $\frac{M_i}{m_e} = 100$. In this simulation a plasma wave is never excited. A plot of the electric field E_x vs. x is given in Fig. 11a at $\omega_p t = 450$. In this simulation ion dynamics are eventually important since Stimulated Brillouim Scattering (SBS) does occur. Simulation I23 is identical to the I22 except the mass ratio is now 1836 and temperature ratio is now 0. In simulation I23 the ion noise is lower by roughly an order of magnitude. The plasma wave is excited as expected, and it is plotted in Fig. 11b at the identical time $\omega_p t = 450$ for convenient comparison. As before, SBS occurs and its effects will be discussed later in Chapter V. Last, in simulation I12 a plasma wave was also never excited. This simulation was previously discussed in Ref. 31. We summarize by remarking that, if ion dynamics are neglected, the typical background noise does not appear to be detrimental when the pump power is above some threshold value. For example, in the simulations if the noise level is less than 10^{-2}, then for $\frac{v_o}{c} \geq .05$ the plasma wave is still excited. The noise level in the simulations is probably larger than that expected in future experiments.

IIIB7. Two Dimensions

The previously discussed simulations were all one-dimensional.

(a)

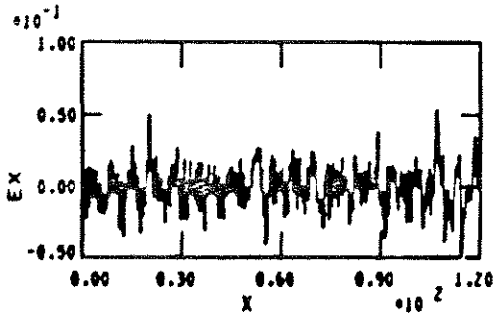

(b)

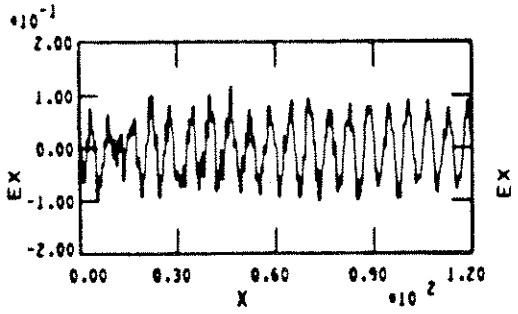

Figure 11. The electric field E_x vs. x at $\omega_p t$ = 450 for a mass ratio of (a) 100 and (b) 1836.

These simulations were in agreement with the reduced envelope equations of the cold plasma fluid theory. The simulations demonstrated that large-amplitude coherent plasma waves can be excited in one dimension. In this section we present the first two-dimensional simulations of beat wave excitation. The results will be compared to the theory of Sec. IIB8 where transverse derivatives were neglected. Furthermore, these simulations provide yet another check of the sign of the nonlinear frequency shift. This is not just a pedantic exercise, since $\vec{V}\times\vec{B}$ need not vanish in 2-D, thereby allowing a possible amplitude-dependent dc current. The sign of the frequency shift is important since for a positive frequency shift, waves are modulationally stable; while for a negative shift they are unstable. A two-dimensional[51] analysis in slab geometry similar to that in Appendix A for one dimensions indicates the extra dimension does not lead to any appreciable amplitude-dependent frequency shift in BWE. We remark that some of these simulations have been briefly discussed elsewhere[5,15]; however, in this discussion more details will be given.

A complete list of the two-dimensional simulations is given in Table II. In the first simulations the laser beams had an infinite cross-section, i.e., they were plane waves; while in the rest the laser beams had finite cross-sections with $\cos^2 \frac{\pi y}{L_o}$ profiles for the electric field. When the laser beams' cross-sections are infinite, i.e., $L_o \to \infty$, the only difference between these and the 1-D cases is the occurrences of transverse (2-D) instabilities. This subject will be discussed in Part B where competing processes are

addressed. In this section only those simulations with finite L_o are presented.

In Fig. 12 we plot the longitudinal electric field E_x vs. x for the center of the beam, $y = 30 \frac{c}{\omega_p}$, at $\omega_p t = 150$ from simulations with different L_o's. The L's are 20, 30, 40, and ∞ c/ω_p, respectively. The simulations were II7, II8, II10, II11, and I10. In all five cases $\tau = 300$ and $v_o/c = .56$. In II7, II10, and I10 the ions were immobile while in the other two they were mobile. In addition, in II10 the lasers were polarized in the 2-D simulation plane. However, at this early time and these high intensities the ions do not play a significant role as will be argued later in Chapter IV. There are only slight differences between the five plots and these differences seem to be related to the plane of polarization. We conclude, therefore, that the longitudinal electric field along the axis of the laser beam is insensitive to L_o, the laser beams width, for early times.

The precise forms for E_x, E_y, and n depend on the lasers' profile. In the linear approximation these fields are straightforwardly obtained from the ponderomotive potential, and this was done in the paper by Fedele et al.[50] in cylindrical coordinates. For comparison to the simulation results we give the linear theory in slab geometry for the transverse profile used in the simulations. In dimensionless units the linear fields are

$$\phi = t \frac{\alpha_1 \alpha_2}{4} \cos^4 k_\perp y \sin (x - t) \qquad (144a)$$

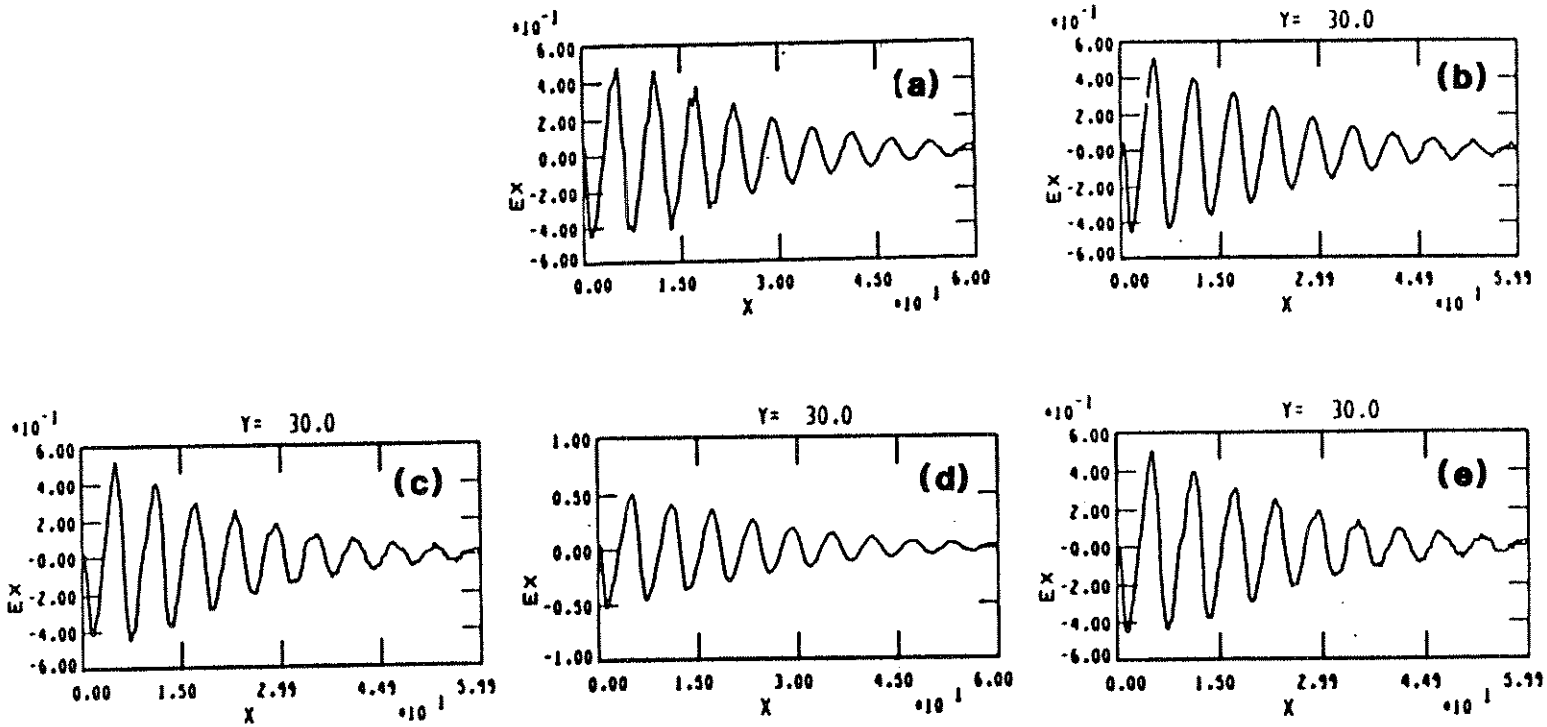

Figure 12. The electric field E_x vs. x along the laser axis at $\omega_p t = 150$ for (a) $L_o = \infty$, (b) $L_o = 20$, $M_i/m_e = \infty$, (c) $L_o = 20$, $M_i/m_e = 1836$, (d) $L_o = 30$, $M_i/m_e = \infty$, (e) $L_o = 40$, $M_i/m_e = 1836$. In all cases $\tau = 300\omega_p^{-1}$.

$$E_x = -t\,\frac{\alpha_1\alpha_2}{4}\cos^4 k_\perp y \cos(x - t) \tag{144b}$$

$$E_y = t\,\alpha_1\alpha_2\, k_\perp \cos^3 k_\perp y \sin k_\perp y \sin(x - t) \tag{144c}$$

$$n = -t\,\alpha_1\alpha_2 \cos^2 k_\perp y \sin(x - t)\left(\frac{1}{4}\cos^2 k_\perp y + k_\perp^2 \cos^2 k_\perp y - 3k_\perp^2 \sin^2 k_\perp y\right) \tag{144d}$$

where $k_\perp = \frac{\pi}{L_o}$. The ratio for maximum E_y to the maximum E_x is

$$\frac{E_{ym}}{E_{xm}} = \sqrt{3}\,\frac{3}{4}\,k_\perp = \sqrt{3}\,\frac{3}{4}\,\frac{\pi}{L_o} \tag{145}$$

where E_{xm} occurs for $k_\perp y = 0$ and E_{ym} occurs for $k_\perp y = \frac{\pi}{6}$. It is also worth noting that the excited plasma wave is actually confined to a smaller region than the lasers. This is shown in Fig. 13a and 13b where the lasers and the longitudinal field transverse profiles are plotted from simulation II11 at $\omega_p t = 150$. Most of the plasma wave energy is confined more closely to the axis than a width of $L_o = 20$ would indicate. This is seen from above, since $E_x \alpha \cos^4 k_\perp y$ while $E_z \alpha \cos^2 k_\perp y$. This point is valid for other geometries since for the linear fields $E_x \alpha E_z^2$ in general.

The contour plots of the scalar potential ϕ and the associated electrostatic fields E_x and E_y are presented in order to understand the transverse field structure. We mention that the fields created from beat wave excitation are not electrostatic when the evolution of E_y is coupled to that of E_x, i.e., transverse derivatives are

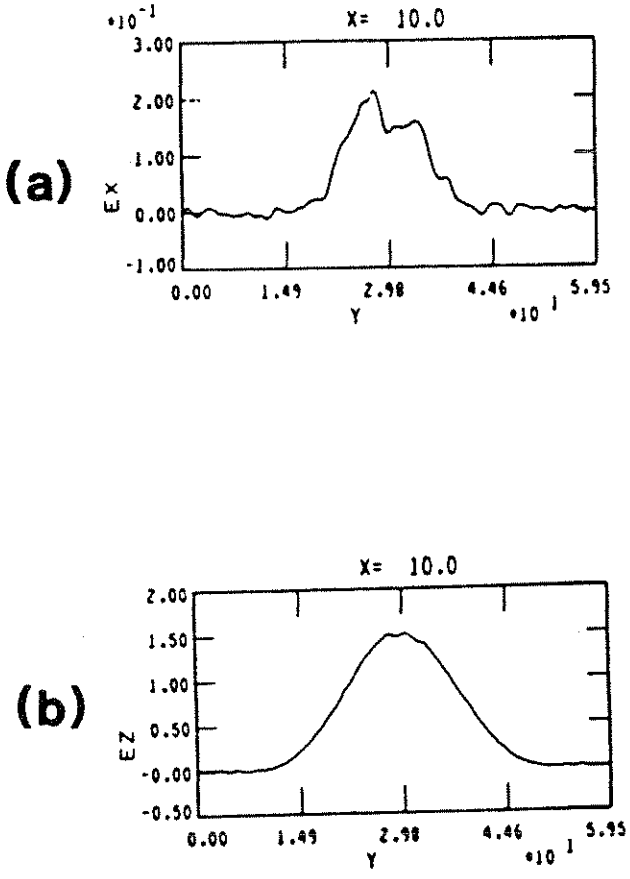

Figure 13. The transverse profile of (a) the plasma wave and (b) the lasers at $\omega_p t = 150$. These were taken at $x = 10\ c/\omega_p$ with $L_o = 20$ and $\tau = 300\ \omega_p^{-1}$.

included.[51] In Fig. 14 we present contour plots of ϕ, E_x, and E_y at $\omega_p t$ = 150 from simulation II8. This simulation is chosen since it has the smallest L_o providing the largest E_y and the best test for using the 1-D equation with y as a parameter. We observe that ϕ is smoother and this is because E being equal to $-\nabla\phi = -\kappa\phi$ naturally gives more importance to the to the higher κ modes.

From Fig. 14 it is evident that for $\omega_p t$ = 150 the wavefronts are coherent and as planar as possible for the narrow spot size used. The ratio of $E_{ym}/E_{xm} \simeq .25$, which is close to .2, the value obtained from Eq. (145) for $L_o = 20\,\frac{c}{\omega_p}$. We also point out that E_y and E_x are $\frac{\pi}{2}$ out of phase as predicted from Eqs. (144b) and (144c). In other words, the E_x and E_y fields are consistent with those that result from only a scalar potential ϕ. We infer that the wave is predominantly electrostatic. The E_y field is what gives rise to what are referred to as focusing and defocusing forces on the accelerated particles.

As expected, in the simulations with larger L_o's the ratio E_{ym}/E_{xm} decreases. When $L_o = \frac{40c}{\omega_p}$, the ratio $E_{ym}/E_{xm} \simeq .16$. This is larger than half the value for $L_o = \frac{20c}{\omega_p}$. However, the E_y field for this case is very incoherent and it is just above the noise level. For this reason, the value of E_{ym} may not necessarily be representative of the wave. In the simulations with $L_o = \frac{30c}{\omega_p}$ the laser was polarized in the y direction making it impossible to determine the E_y associated with the plasma wave.

The results presented until now were for times when the linear theory was still valid. As time progresses the nonlinear frequency

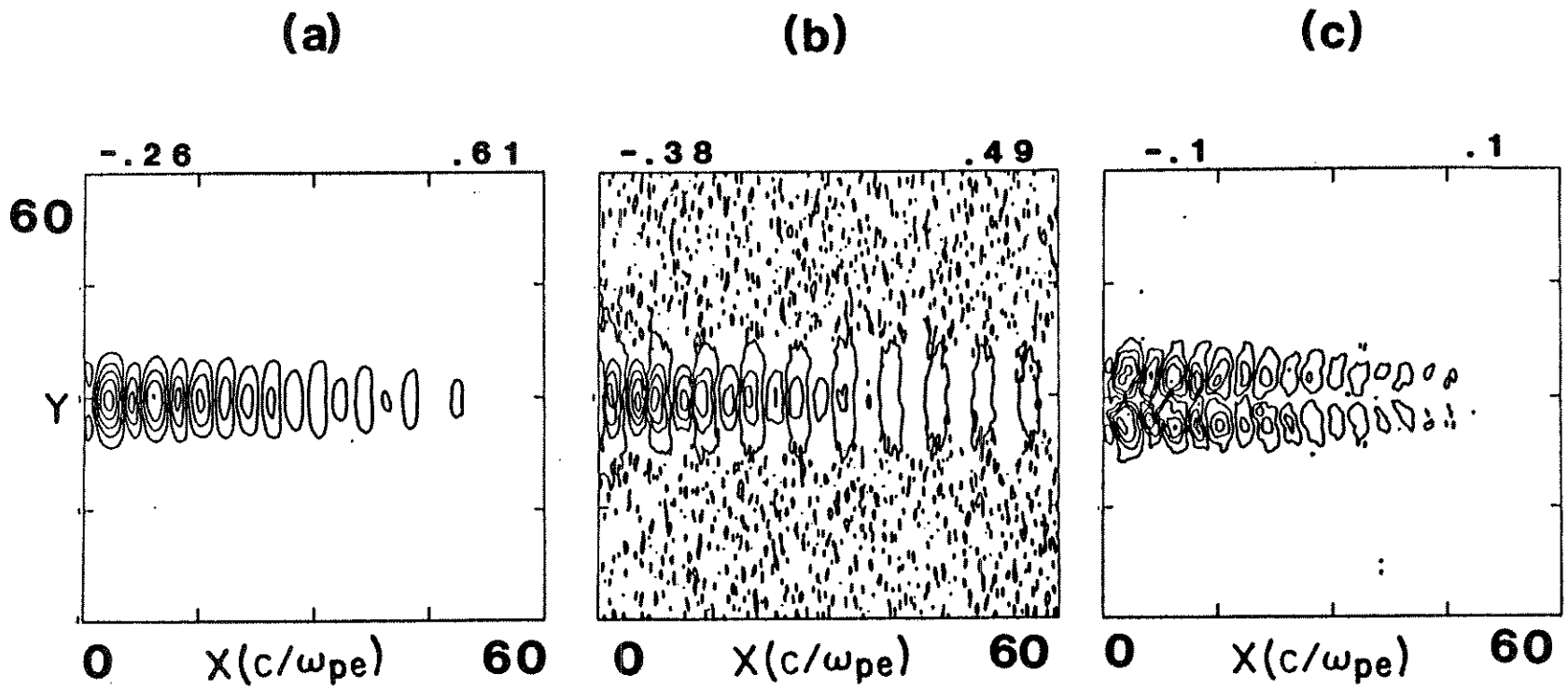

Figure 14. Contour plots of (a) the scalar potential, (b) E_x, the accelerating field, and (c) E_y, the focusing and defocusing field at $\omega_p t = 150$. The laser's spot size was $L_o = 20$, $\tau = 300\ \omega_p^{-1}$, and $M_i/m_e = 1836$. The vlaues of the minimum and maximum contours are given.

shift manifests itself. This is most easily seen from the evolution in time of the contour plot of ϕ. In Fig. 15 we plot the contours of ϕ at $\omega_p t$ = 150, 180, and 210 from simulation II8. The plot at $\omega_p t$ = 150 was also shown in Fig. 14 and is presented here for a comparison with the other two plots. Unlike the case at $\omega_p t$ = 150, the potential at $\omega_p t$ = 180 no longer has planar wavefronts on the left-hand side of the simulation box. The wavefronts appear to be breaking up. As in the 1-D case the variables x and t can be used interchangeably to the extent that quantities are functions only of $t - \frac{x}{v_g}$. The transverse splitting of the wavefronts can then be explained as follows. It was shown earlier in Sec. IIB2 that in 1-D the saturation time scales inversely with F to some power. The scaling being $t_s \alpha F^{-2/3}$ with no rise time and $t_s \alpha F_o^{-2/7}$ with a quadratic rise time for F. Consequently, the plasma wave will saturate at an earlier time for larger F. If F is a function of y and the equation for the evolution of E_x is absent of any transverse derivatives, then y can be treated as a parameter, then E_x will saturate first for the values of y where F is largest. We have assumed that $F = f(y)g(t - \frac{x}{v_g})$. In the simulation, therefore, where the y dependence of F is $\cos^4 \frac{\pi \Delta y}{L_o}$ for $|\Delta y| < \frac{L_o}{2}$ and 0 for $|\Delta y| > \frac{L_o}{2}$, E_x should reach its peak amplitude first at $\Delta y = 0$. We have defined $\Delta y \equiv y - y_o$. The field E_x will then begin to decrease at $\Delta y = 0$ while for the neighboring Δy's it will continue to increase. Then for these Δy's it will begin to decrease while it continues to increase for still larger Δy's and so on. This behavior will manifest itself as the splitting struc-

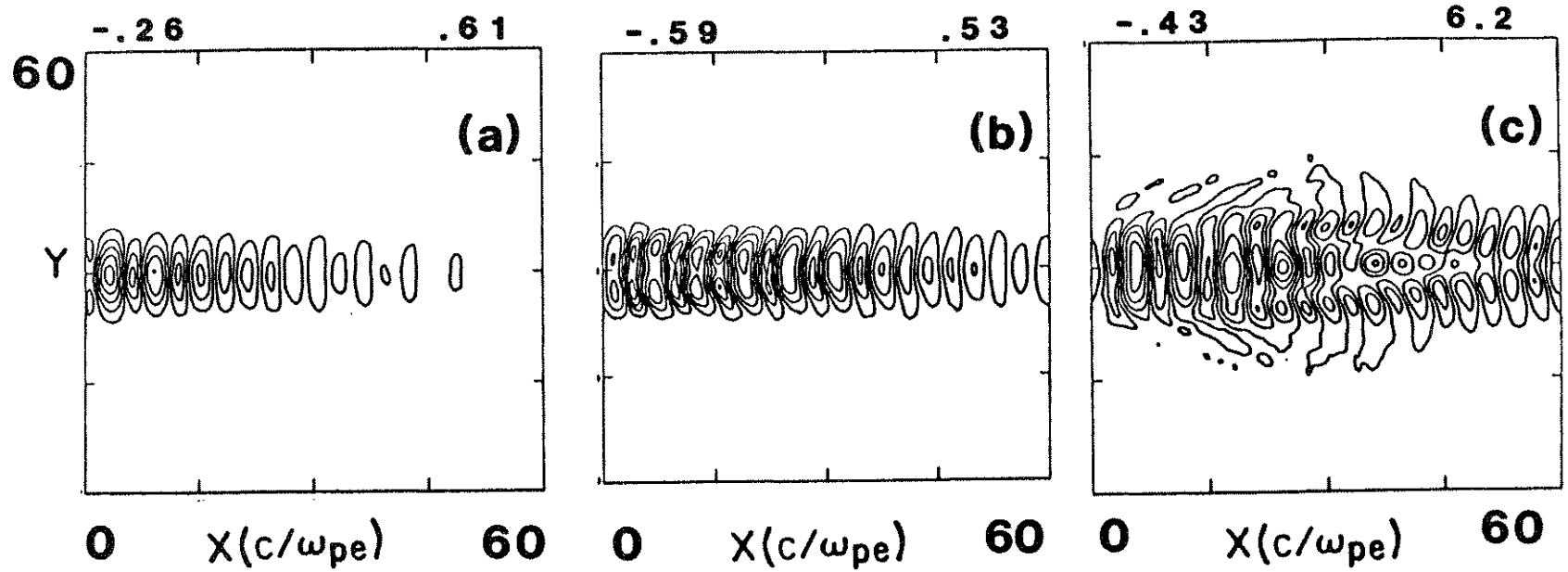

Figure 15. Contour plots of the scalar potential at (a) $\omega_p t$ = 150, (b) $\omega_p t$ = 180, and (c) $\omega_p t$ = 210. The laser spot size was L_o = 20 c/ω_p and $\tau = 300\omega_p^{-1}$. The values of the minimum and maximum contours are given.

ture seen in the contour plot of E_x. If the transverse derivatives can be neglected, then ϕ and E_x basically satisfy the same equation. Therefore, the contour plot of ϕ, which is actually presented, is similar to that of E_x. The splitting structure leads to both larger and more complicated focusing and defocusing (E_y field for our geometry) forces. This was argued in Sec. IIB8. The contour plots of E_x and E_y are shown in Fig. 16 at $\omega_p t = 180$ for simulation II8. The ratio of $\frac{E_{ym}}{E_{xm}}$ is now .44, which is approximately twice that at $\omega_p t = 150$. While E_x is similar in magnitude, E_y is larger since the distance over which ϕ varies in the transverse y direction is shorter (~1/3 shorter).

Furthermore, at this time when ϕ and E_x have a dip on axis, E_y changes sign two times rather than once across the wavefront. Therefore, at a position x where an accelerating field exists there is always some y for which a focusing force also exists. This structure of E_y is seen as four islands at some x in the contour plot of E_y shown in Fig. 16b. This is probably not useful for particle acceleration since each bunch in successive wavefronts would not be aligned in y. However, we have not ruled out the possibility that these fields may have some other application. The importance of the above is that, although the transverse derivatives are signficant ($E_y \simeq E_x$), the conclusions of Sec. IIB8 where they are neglected are borne out qualitatively in the simulations.

As time progresses still further, ϕ will begin to increase again on the axis, and this is seen in Fig. 15c ($\omega_p t = 210$). For this case, the peak amplitude in this second cycle will actually be

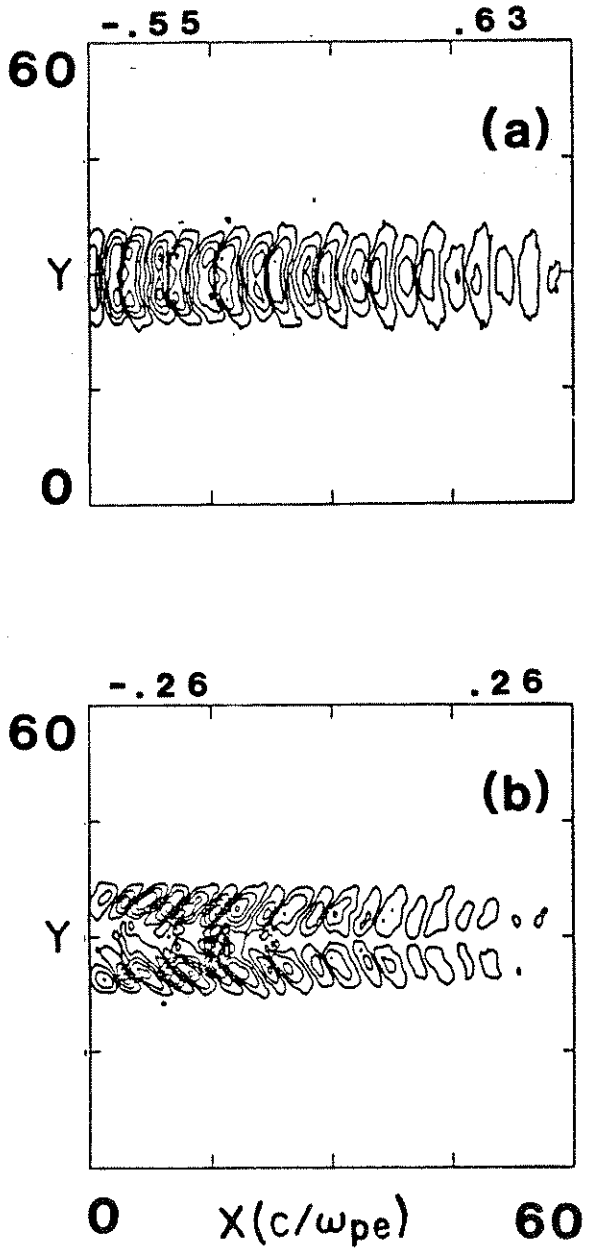

Figure 16. Contour plots of (a) E_x the accelerating field and (b) E_y the focusing and defocusing field at $\omega_p t = 180$. The laser spot size was 20 c/ω_p and $\tau = 300\omega_p^{-1}$. The values of the minimum and maximum contours are given.

larger than that in the first cycle. This was also seen in the solution to the envelope equations. The waves' width is also narrower, so the treatment of y as a parameter is no longer permissible.

The wavefronts not only split but bend forward so that they resemble the letter C. This is due to the fact that the nonlinear frequency shift is negative. If it was positive, the wavefronts would bend backwards. To argue this we recall that it was shown in Sec. IIB8 that if all variables were predominantly functions of $t - \frac{x}{v_g}$, then the phase velocity of the plasma wave is relatively constant irrespective of the sign of the nonlinear frequency shift. Therefore, if a detector was situated at a fixed position and if the wavefronts moved at the same velocity, then in order to measure a negative frequency shift the space between each wavefront would need to get larger.

In other words, a nonlinear wavelength shift of the opposite sign and appropriate magnitude arises to keep V_ϕ relatively constant. The wavefronts evolve into C's because the frequency shift is largest where the wave amplitude is largest, which is initially on the laser axis. In addition, as the amplitude on axis begins to decrease, after it reaches its peak amplitude, the frequency shift begins to decrease. The wavefront on axis should appear to come forward and indeed this is observed on the left-hand side of Fig. 15c.

When the peak ampliltude is first reached, by definition ϕ, the phase difference between the plasma wave and the driving

force, has shifted by $\frac{\pi}{2}$ from its initial value. The outside region of one wavefront never develops a frequency shift since the amplitude is always small. Along the axis where the nonlinear frequency shift is largest initially, the electrostatic field's phase eventually will lag that on the outside of the beam by $\frac{\pi}{2}$. Consequently, the electric field at a particular x is eventually due to two wavefronts. (Wavefronts refer to regions of either positive or negative potential.) When this occurs the negative peak of one wavefront will line up in x with the outside of a positive wavefront. This occurs only at t_s when, by definition, ϕ has shifted by $\frac{\pi}{2}$. This phenomena is observed in Fig. 15b near $x = 20c/\omega_p$.

In order to illustrate the dependence of the transverse structure on L_o, the laser spot size, we show in Fig. 17 contour plots of ϕ at $\omega_{pt} = 150$ for $L_o = 20$, 30, and 40. In Fig. 18 the same sequence of plots is given at $\omega_p t = 180$ for $y = 30c/\omega_p$. For $L_o = 20\ \frac{c}{\omega_p}$, results are presented for both mobile and immobile ions and when $L_o = 30\ \frac{c}{\omega_p}$ the laser is polarized in the simulation plane. At $\omega_p t = 150$, the wavefronts are planar for all three values of L_o. Neither the use of mobile ions nor the change in the polarization plane seems to make much difference at this time. This similarity was also reflected in the axial plots presented earlier in Fig. 12. The contour plots become progressively more incoherent and asymmetrical with increasing L_o at $\omega_p t = 180$. When comparing the two $L_o = 20\ \frac{c}{\omega_p}$ plots, it is evident that with mobile ions ϕ is only slightly affected. These differences are probably due to the increased noise level that accompanies the use of dis-

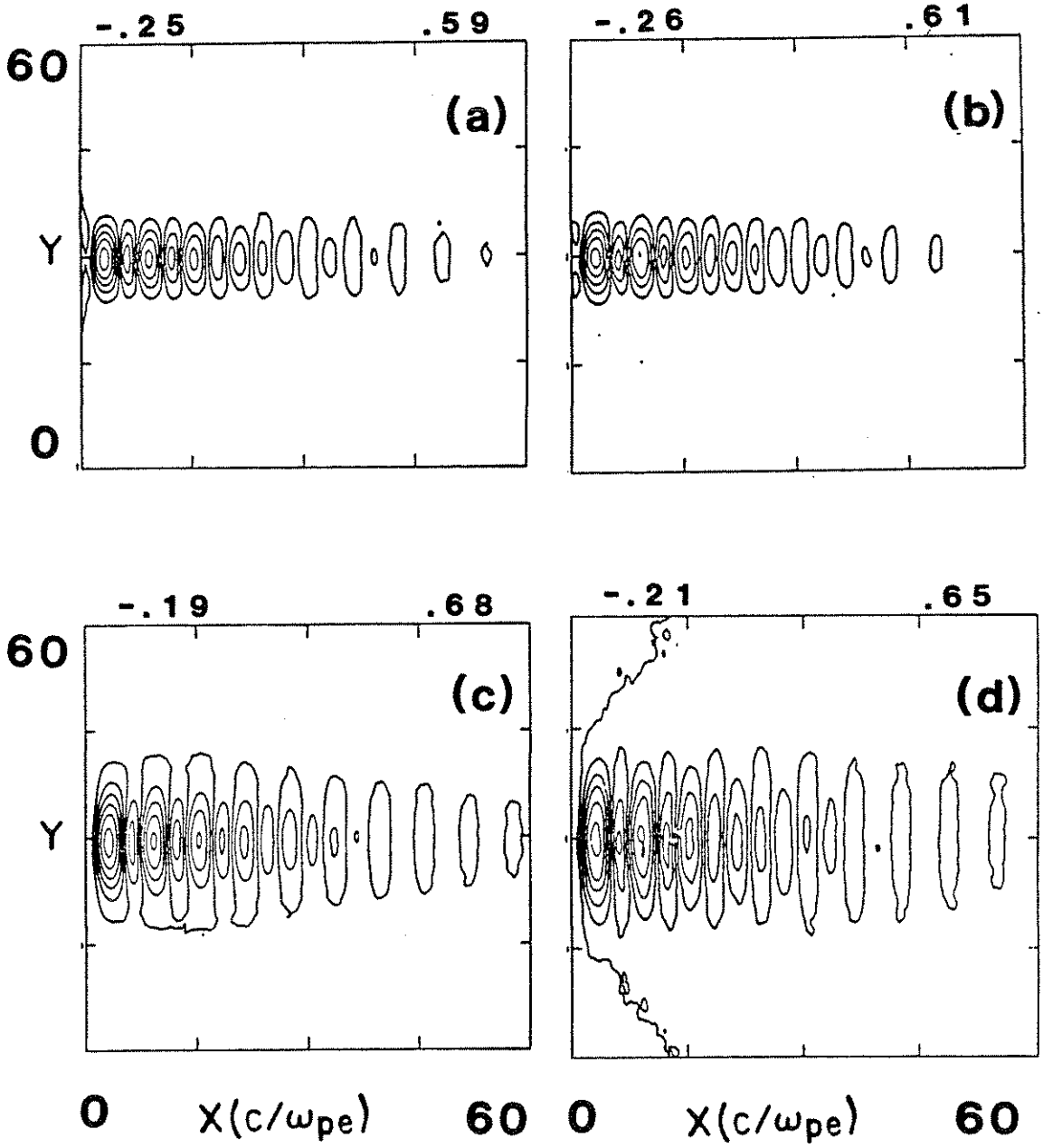

Figure 17. Contour plots of the scalar potential ϕ at $\omega_p t = 150$ for (a) $L_o = 20\ c/\omega_p$, $M_i/m_e = \infty$, (b) $L_o = 20\ c/\omega_p$, $M_i/m_e = 1836$, (c) $L_o = 30\ c/\omega_p$, $M_i/m_e = \infty$, and (d) $L_o = 40\ c/\omega_p$, $M_i/m_e = 1836$. The values of the minimum and maximum contours are given.

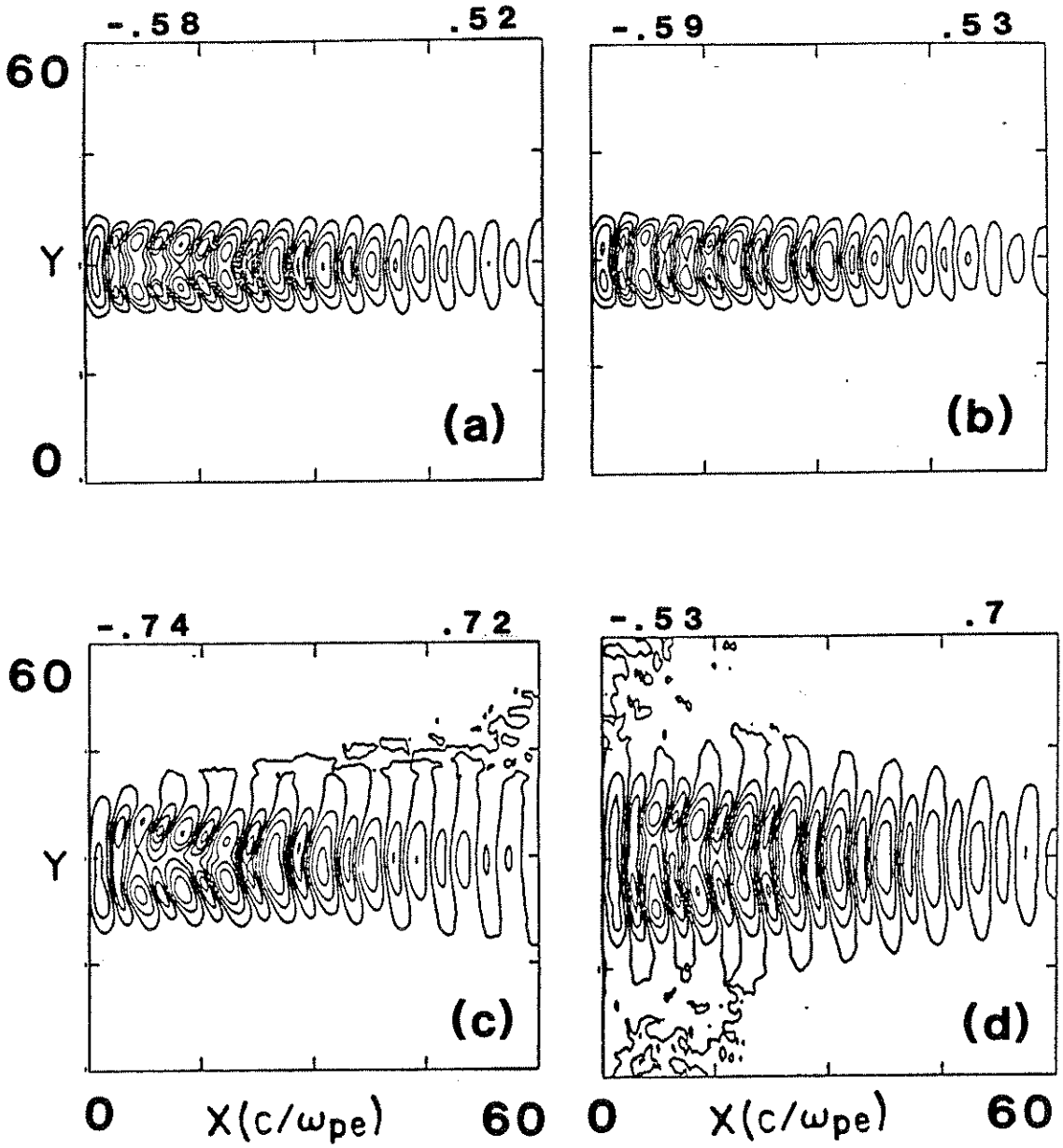

Figure 18. Contour plots of the scalar potential ϕ at $\omega_p t = 180$ for (a) $L_o = 20\ c/\omega_p$, $M_i/m_e = \infty$, (b) $L_o = 20\ c/\omega_p$, $M_i/m_e = 1836$, (c) $L_o = 30\ c/\omega_p$, $M_i/m_e = \infty$, and (d) $L_o = 40\ c/\omega_p$, $M_i/m_e = 1836$.

crete ions. At later times $\omega_p t = 210$, the difference between the various simulation results are even more pronounced. We believe this is due to competing processes. More detail and explanation will be forthcoming in Part B.

The plots of E_x vs. x along the axis do not exhibit the same degree of disparity for $\omega_p t = 180$. In Fig. 19 we plot E_x vs. x along $y = 30 \frac{c}{\omega_p}$ at $\omega_p t = 180$ for the five cases in Fig. 12. The most notable differences are between the immobile and mobile ion cases. With immobile ions the field saturates at a larger amplitude and it drops off more rapidly behind the point where the peak amplitude is obtained. The sharp dropoff is caused by the damping from the trapped electrons. It may very well be that this peak would actually be the largest peak in the absence of trapped electrons. There are more trapped electrons in the immobile ion runs because the field is larger. The field is larger because the discrete ions (or equivalently the increased noise level) give rise to an effective damping or scattering of energy and of the beat wave. This was alluded to in Sec. IIB7.

We also integrated the envelope equations for the simulation parameters of $F = .08$, $\Delta_o = -.0075$, and $\tau = 300\omega_p^{-1}$ and the result is presented in Fig. 19a. The peak amplitude occurs at $\omega_p t_s = 160$ for $e_m = .7$ from which we infer $E_m = .82$. The amplitude differs from the simulation results, where $\omega_p t_s \simeq 160$ and $E_m = .73$, predominantly because the envelope equations were derived to lowest order in $\frac{v_x^2}{c^2}$ and with particle trapping neglected. For these high intensity cases, more terms must be kept or, following Noble,[22] the

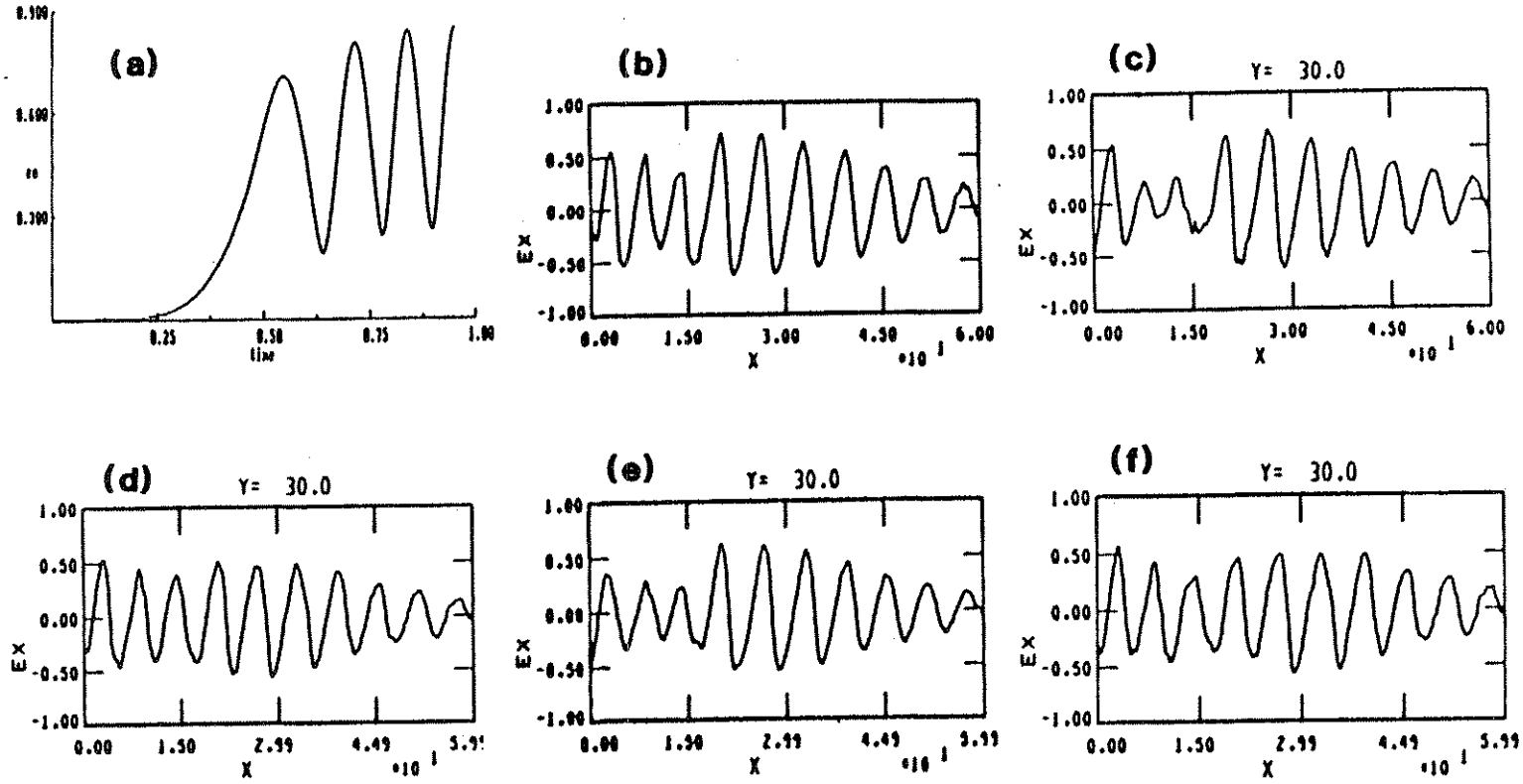

Figure 19. (a) The solution to the envelope equations $e_o(t)$ for $\alpha_1 = \alpha_2 = .56$, $a_e = .1$ and, $\tau = 300\omega_p^{-1}$ at $\omega_p t = 180$. Time is measured in units of τ. The electric field E_x vs. x along the laser axis for (b) $L_o = \infty$, $M_i/m_e = \infty$, (c) $L_o = 20c/\omega_p$, $M_i/m_e = \infty$, (d) $L_o = 20c/\omega_p$, $M_i/m_e = 1836$, (e) $L_o = 30c/\omega_p$, $M_i/m_e = \infty$, and (f) $L_o = 40c/\omega_p$, $M_i/m_e = 1836$.

envelope equations of the exact undriven system need to be used. Nevertheless, the differences are not too great, so even when E_m = .8 the envelope equations provide useful results. The numerical result shows that e_o will decrease to .2 by $\omega_p t$ = 187.5 so that at $\omega_p t \simeq 180$ the value of e_o is ~.4. Although the value of e_o does not decrease as much as predicted from the envelope equations after saturation, there is qualitative agreement. The same plots at $\omega_p t$ = 210 are in better agreement if the predicted temporal dependence is translated to an equivalent spatial dependence.

As time progresses still further, y can no longer be treated as a parameter. In places, E_y becomes on the order of E_x, so the spatial transverse scale becomes comparable to $\frac{c}{\omega_p}$. Furthermore, the plasma wave begins to influence how the laser evolves. This will be taken up later in Chapter V. At this time except in the narrow beam cases the plasma wave is no longer useful for particle acceleration.

In order to study the role of the laser rise time, simulations identical to II11, except for the magnitude τ, were done. The rise time was changed from $300\omega_p^{-1}$ to either $150\omega_p^{-1}$ or $800\omega_p^{-1}$. The results are summarized in Figs. 20 and 21 where contour plots of ϕ are given at $\omega_p t$ = 90 and 150 for II16 and $\omega_p t$ = 300 and 420 for II12.

For the short rise time simulation, the plasma wave is initially very planar and coherent as shown in Fig. 20a. Soon afterward, as seen in Fig. 20b, however, the plasma wave becomes very incoherent. This is partly due to wave-particle interactions. The same quali-

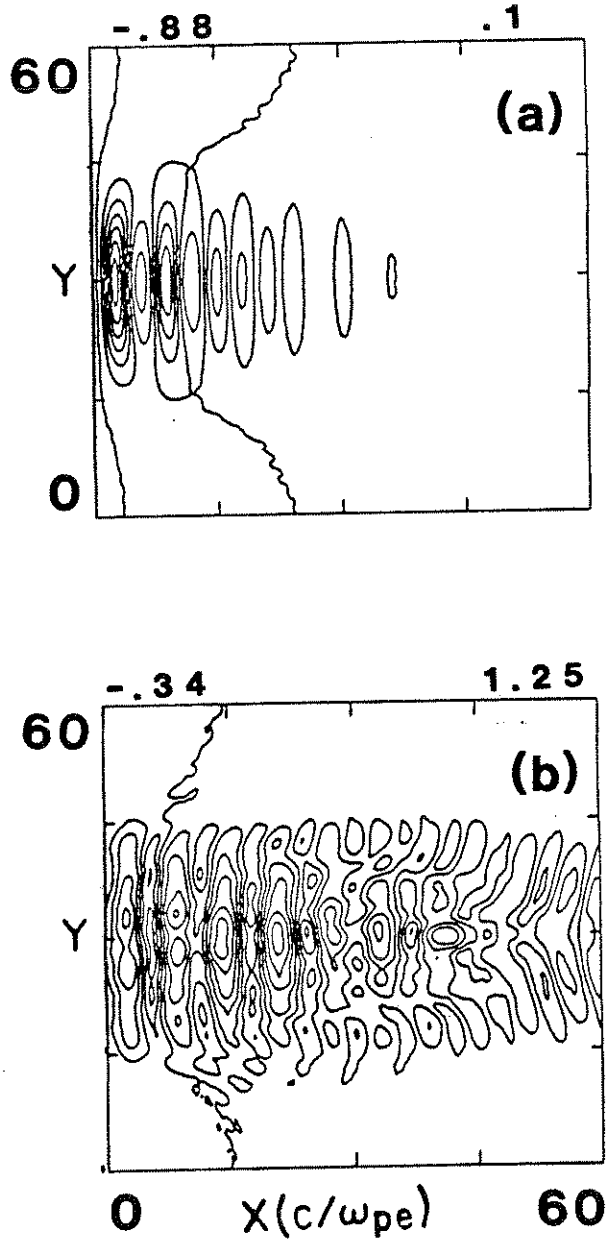

Figure 20. Contour plots of the scalar potential ϕ at (a) $\omega_p t$ = 90 and (b) $\omega_p t$ = 150. The laser spot size is L_o = 40 c/ω_p and $\tau = 150\omega_p^{-1}$. The values of the minimum and maximum contours are given.

tative features concerning the split structure of the fields is also observed. This simulation also permits another chance to check the formula for $\frac{E_{ym}}{E_{xm}}$ predicted from linear theory. This is because the fields arise before any competing instabilities and the fields are significantly above the noise. We find $\frac{E_{ym}}{E_{xm}} = .16$ at $\omega_p t = 90$, which is in reasonable agreement with the predicted value of .1 for $L_o = 40$.

For the long rise time simulations, the plasma wave is reasonably coherent at the earlier time $\omega_p t = 300$. It is not as coherent as in the shorter rise time simulations for times when the wave amplitude was comparable. At $\omega_p t = 420$ the plasma wave is very incoherent. This is shown in Fig. 21a and 21b. By this time competing processes are occurring. In fact, ion dynamics have even become important and this will be shown later in Chapter V.

The 2-D simulations previously discussed all used the same laser intensity. To study the effect of laser intensity in 2-D, simulation II17 was carried out. The parameters were identical to II11 except that $\frac{v_o}{c} = .14$ for each beam. The plasma wave evolution is displayed in Fig. 22 where the contour plot of ϕ is given for both $\omega_p t = 240$ and 300. For comparison, plots of E_x vs. x from the 2-D simulations and an identical 1-D run with fixed ions are presented in Fig. 23. Even as early as $\omega_p t = 240$, the plasma wave is less coherent in the 2-D case. This is seen in both the axial and contour plots. The phase fronts are not planar as well. The differences between the 1-D and 2-D simulations are the result of both the increased noise level in the 2-D case and the competing

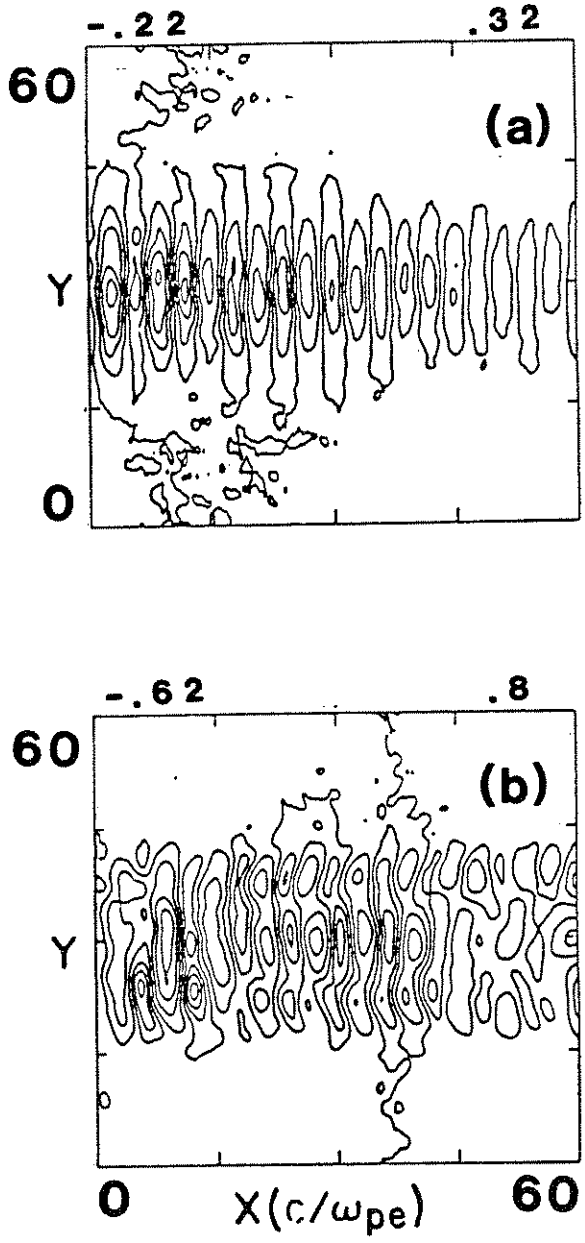

Figure 21. Contour plots of the scalar potential ϕ at (a) $\omega_p t$ = 300 and (b) $\omega_p t$ = 420. The laser spot size is L_o 40 c/ω_p and $\tau = 800\omega_p^{-1}$. The values of the minimum and maximum contours are given.

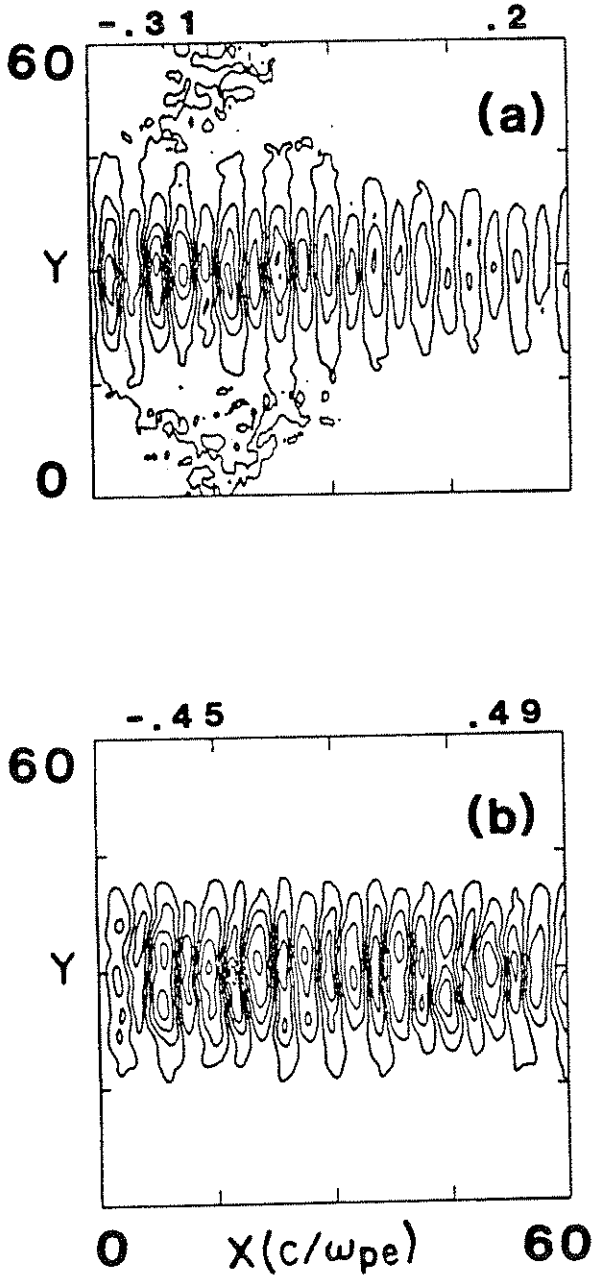

Figure 22. Contour plots of the scalar potential ϕ at (a) $\omega_p t$ = 240 and $\omega_p t$ = 300. The laser spot size is L_o = 40 c/ω_p, $\alpha_1 = \alpha_2$ = .28, and $\tau = 300\omega_p^{-1}$. The values of the minimum and maximum contours are given.

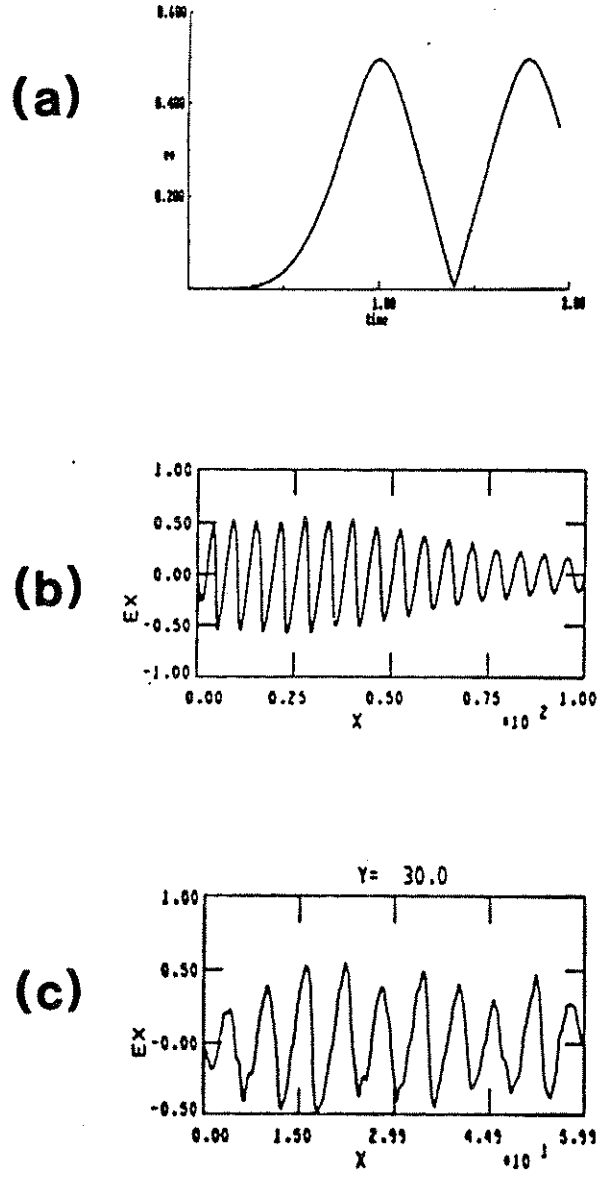

Figure 23. (a) The solution to the envelope equations $e_o(t)$ for $\alpha_1 = \alpha_2 = .14$, $a_e = .1$, and $\tau = 300\omega_p^{-1}$. The electric field E_x vs. x down the laser axis at $\omega_p t = 300$ for (b) $L_o = \infty$, $M_i/m_e = \infty$ and (c) $L_o = 40$, $M_i/m_e = 1836$.

transverse instabilities. The plasma wave does not saturate during the rise time for this low-intensity case. This is seen in Fig. 23a where the envelope of the plasma wave is plotted. The 1-D simulation results are in reasonable agreement with the envelope equations. The 2-D simulation agrees only in a qualitative sense. Last, we remark that the ratio $\frac{E_{ym}}{E_{xn}} \simeq .22$, which is above the predicted value. However, the E_y field is not very much above the background noise level and consequently is not coherent. Exact agreement is therefore not expected.

In summary, we remark that these first 2-D simulations demonstrate that a coherent wave with the necessary properties can be excited if both the rise time is short enough, the laser intensity is high enough, and the laser spot size is narrow enough. These requirements are partly tied to the requirements that competing instabilities be avoided. This will be discussed in Chapter V. In future experiments the laser profile cannot be expected to be as smooth, but the background plasma noise is expected to be much lower.

IIIC. Summary

We have attempted to determine the validity of the theory in Sec. IIB through numerical and kinetic simulations. In the process, those areas in which future work is necessary are identified. The envelope equations agree with the simulations in the following respects: When the pump strength F is smaller than $\simeq .02$, the saturated amplitude is accurately described by the fluid equations

with the cubic nonlinearity. When the rise time effects are relevant, agreement also exists for the saturation amplitude.

The saturation time and, in some cases, the growth rate are not in as good agreement with the envelope equations. In the simulations, saturation occurs earlier than the fluid equations predict. The growth rate in some cases increases dramatically during the initial growth cycle and this causes the earlier saturation. The increase in the growth rate is believed to be caused by cascading including the $\Delta\omega = 2\omega_p$ coupling. The simulations were for relatively small values of $\frac{\omega_o}{\omega_p}(\simeq 10)$. The larger the ratio $\frac{\omega_o}{\omega_p}$ the longer it takes for cascading to occur. However, the acceleration distance also increases. The issue of 1-D cascading, pump depletion, and efficiency is, therefore, an area that deserves diligent effort. Proper numerical efforts are necessary. The disagreements are the result of fluid not kinetic effects.

The ratio of the harmonics for both the electric field and the density is in agreement with Sec. IIB5. The inclusion of the first three harmonics gives reasonable waveforms for small field amplitudes. When the pump strength is larger than $\simeq .04$, more terms need to be kept or the treatment of Noble[22] needs to be used. For example, when $E_x \simeq .75$, the peak density given by keeping the first three harmonics was 2.4 while the observed density was 2.7-3.0.

We observe both qualitative and quantitative agreement with the tuning curves of Tang et al.[9] We find that the simulations, therefore, are consistent with a negative frequency shift. The agreement was observed in both homogeneous and inhomogeneous plasmas.

In the homogeneous cases, when Δ_0 was positive (Δ_0 + F was also positive) the saturation amplitude was smaller than the $\Delta_0 \simeq 0$ case. On the other hand, when Δ_0 was negative the eventual saturated amplitude was larger. However, in the latter case there was disagreement between the numerical and the PIC simulation results as regards to the optimum Δ_0. When the plasma had a linear density gradient, the plasma wave eventually became larger on the positive density side (negative frequency mismatch). This is consistent with Tang et al.[9] and a negative nonlinear frequency shift.

Mode coupling of the beat-excited plasma waves to slower phase velocity plasma wave from a pre-existing density ripple was observed. The plasma was initially cold. The slower phase velocity modes heat the plasma first from wave breaking and second from wave-particle interactions. As the plasma heats up, the mode coupling ceases since the coupled modes are no longer normal modes because of the linear temperature frequency shifts. Thus, the mode-coupling process appears to be self-stabilized. More details, including mode-coupling in a warm plasma (quasi-resonant mode-coupling), can be found in Refs. 40 and 41. Thermal effects are basically important when $\kappa^2\lambda_d^2 \gtrsim \epsilon$.

Simulations were presented that circumstantially showed that a large enough noise level can suppress BWE. The results are qualitative and a more quantitative description is in progress. The simlations indicate that the damping results from the ion noise due to discrete ion effects not ion inertia.

The 2-D simulations indicate that plasma waves with planar

wavefronts can be excited by BWE. We find that the accelerating electric field down the lasers' axis is similar to that in 1-D simulations for times up to the initial saturation. This 1-D behavior is insensitive to the laser spot size. The simulations demonstrate that using the 1-D envelope equations with y treated as a parameter provides a reasonable description even for the narrow laser beams. From the shape of the wavefronts, we can therefore infer that the nonlinear frequency shift is negative if treating y as a parameter is valid. Eventually, this description is not valid; but by this time the wave is no longer useful for acceleration. The plasma wave was less coherent in regard to both the accelerating and the focusing and defocusing fields for the largest rise times. This is because competing processes have time to develop. The laser intensity needs to be larger when the laser rise time is made shorter in order to excite the most coherent plasma wave.

PART B. COMPETING INSTABILITIES

Chapter IV. Descriptions of Competing Instabilities

IVA. Introduction

In Chapters II and III the subject of Beat Wave Excitation was examined both analytically and computationally in the absence of any competing instabilities. The instabilities of both light waves and the excited plasma wave are important because they can scatter energy out of the laser beam and they can lead to the break up of both laser beams and the plasma wave. The instabilities are the result of both three wave decay (resonant) and four wave modulational (nonresonant instabilities).

Instabilities that scatter light are the Stimulated Brillouin Scatter[10,11,57] (SBS) and Stimulated Raman Scatter[10,11,13] (SRS) instabilities. These instabilities are resonant parametric three wave instabilities. That is, all three waves are normal modes that satisfy their respective dispersion relations.

In SBS a light wave decays into a backward traveling light wave and a forward propagating ion acoustic wave. In SRS a light wave decays into another light wave and a plasma wave. These instabilities have received enormous attention during the previous 15 years owing to their profound importance to laser fusion. SBS reflects light while SRS reflects light and generates "energetic" electrons. In laser fusion the energetic electrons are deleterious since they preheat the D-T fuel preventing the compression neces-

sary for fusion.[58] In this case the term energetic refers to the 10-1000 KeV range, which is not of interest for particle accelerators. We will refer to the voluminous[7,10,11,13,57] amount of previous work on these instabilities to argue when these instabilities will be important and how they may be avoided. We point out that most of the previous work treats the instabilities separately and only recently has there been a concerted[59] effort to examine the competition between them.

The instabilities that lead to the breakup of the light are four-wave nonresonant modulational instabilities. These are relativistic[48] and ponderomotive filamentation[57] of light. Raman Forward Scatter[7,13] can also be considered in this category. Those instabilities that lead to the breakup of plasma waves are both resonant and nonresonant instabilities. The nonresonant instabilities are self-modulation and filamentation from both relativistic[47] and ponderomotive[60] nonlinearities. The resonant instability is parametric decay. Furthermore, the evolution of the light wave affects the evolution of the plasma wave and vice versa.

In Sec. IVB for completeness we rederive the growth rate and range of unstable k's for the relativistic self-modulation and filamentation of both light and plasma waves following the work of Max et al.[48] This is done because these processes are not as well-known as their ponderomotive counterparts. Additional theoretical[61,62] work on relativistic self-focusing has recently appeared in the literature. We prefer instead to use the work of Max et al.,[48] since it is a stability analysis and it is done in slab

geometry. The power thresholds given in Refs. 61 and 62 can be obtained from the threshold criteria for stability. The stability analysis is easily generalized to plasma waves. Therefore, for our purposes Max et al.[48] is adequate. However, to treat whole-beam self-focusing in cylindrical coordinates a procedure along the lines of Sprangle and Tang[61] is required. Furthermore, we discuss how the instabilities of the plasma wave and the light waves are coupled. This phenomenon was coined resonant self-focusing when it was first observed for ponderomotive process.[63] We also quote the growth rates for the ponderomotive processes since they are more commonly found in the literature.

In Chapter V the usefulness of growth rates and unstable k's of the competing instabilities, both relativistic and ponderomotive, is examined via kinetic simulations. The interplay between the various processes is emphasized. Last, in Chapter VI we comment on the relevance of the simulations to recent experiments.

IVB. Growth Rates

Section IVB is organized as follows. To begin, in Sec. IVB1 the growth rate and unstable k's for self-modulation and filamentation due to the relativistic correction to the electron mass for plasma waves and light waves are reviewed. Possible higher order coupling between the light waves and the plasma wave is also discussed. We classify the higher order couplings as resonant self-focusing.[63]

The voluminous literature of other competing instabilities is

reviewed. Processes that affect the light waves are discussed in Sec. IVB2. These are ponderomotive self-focusing and filamentation, SBS, and SRS. In Sec. IVB3 ponderomotive effects on the plasma waves are reviewed. These include parametric decay, modulational instability, and the OTSI. For all cases, growth rates and unstable k's are given along with discussions on the relative importance of each instability.

IVB1. Relativistic Instabilities

To describe relativistic filamentation and self-modulation, we begin with the generalized nonlinear wave equation for either the transverse or longitudinal normalized electric field.

$$\left[\left(\frac{\partial^2}{\partial t^2} - c_j^2\nabla^2\right) + \omega_p^2\left(1 - \epsilon_j\,|E|^2\right)\right]E = 0 \qquad (146)$$

where $c_j = c$ and $\epsilon_j = \frac{1}{2}\left(\frac{3}{4} - \frac{\omega_1^2 - \omega_p^2}{4\omega_1^2 - \omega_p^2}\right)$ for linearly polarized light waves and $c_j = \left(3\kappa T/m\right)^{1/2}$ and $\epsilon_j = \frac{3}{8}$ for plasma waves. The fields are normalized to $\frac{mc\omega_j}{e}$. A derivation of Eq. (146) for light waves is in Ref. 28 and for plasma waves in Appendix A. In deriving the wave equation in Eq. (146), only the lowest order nonlinearities were kept. When E_o approaches unity, then the higher order nonlinearities need to be retained. (However, it can be shown that the higher order corrections from relativistic effects are not that important for values near $E_o = .8$.)

The mechanism for filamentation and self-focusing can be described qualitatively as follows. The dielectric function corres-

ponding to the wave equation in Eq. (146) is

$$\epsilon = \left(1 - \frac{\omega_p^2}{\omega_0^2} + \frac{\epsilon_j}{\omega_0^2}\,|E|^2\right). \tag{147}$$

The phase velocity of a wave is largest where ϵ is smallest. Where $|E|$ is large, ϵ is also large and the phase velocity is therefore small. So for a finite size light beam or a filament, the phase velocity is largest toward the outside of the beam. The result is that the wavefronts curve to form a C, which means that light is directed toward the axis. This will eventually cause nonplanar wavefronts for the beat-excited plasma wave. The C shape of the plasma wave seen in Chapter III was not the result of this.

In order to be more quantitative, we determine the stability of a plane wave by assuming that

$$E = \frac{1}{2}\left(E_0 e^{i\psi_0} + E_+ e^{i\psi_+} + E_- e^{i\psi_-} + cc\right) \tag{148}$$

where $\psi_0 = k_0 x - \omega_0 t$ and $\psi_\pm = \left(\vec{k} \pm \vec{k}_0\right)\cdot\vec{r} - (\omega \pm \omega_0)t$. Linearizing Eq. (146) about E_0 by leads to the two coupled equations

$$(-\omega_-^2 + c_j^2 k_-^2 + \omega_p^2)E_- = 2\omega_p^2 \epsilon_j |E_0|^2 E_- + \omega_p^2 \epsilon_j E_0^2 E_+ \tag{149a}$$

$$(-\omega_+^2 + c_j^2 k_+^2 + \omega_p^2)E_+ = 2\omega_p^2 \epsilon_j |E_0|^2 E_+ + \omega_p^2 \epsilon_j E_0^2 E_-. \tag{149b}$$

The expressions

$$\omega_{\pm}^2 - \omega_p^2 - c_j^2 k_{\pm}^2 \tag{150}$$

reduce to

$$\omega^2 \pm 2\omega\omega_o - c_j^2 k^2 \pm 2c_j^2 \vec{k} \cdot \vec{k}_o + \omega_p^2 \epsilon_j |E_o|^2 \tag{151}$$

by using the dispersion relation for the pump

$$\omega_o^2 - \omega_p^2 - c_j^2 k_o^2 = -\omega_p^2 \epsilon_j |E_o|^2. \tag{152}$$

It is further assumed that $E_o = E_o^*$ so that Eqs. (149a) and (149b) reduce to

$$\left[-\left(\omega^2 - c_j^2 k^2\right) - 2\left(\omega\omega_o - c_j^2 \vec{k} \cdot \vec{k}_o\right) - \omega_p^2 \epsilon_j |E_o|^2\right] E_-$$

$$- \omega_p^2 \epsilon_j |E_o|^2 E_+^* = 0 \tag{153a}$$

$$\left[-\left(\omega^2 - c_j^2 k^2\right) + 2\left(\omega\omega_o - c_j^2 \vec{k} \cdot \vec{k}_o\right) - \omega_p^2 \epsilon_j |E_o|^2\right] E_+^*$$

$$- \omega_p^2 \epsilon_j |E_o|^2 E_- = 0 \tag{153b}$$

These equations provide the dispersion relation

$$0 = (\omega^2 - c_j^2 k^2)^2 - 4(\omega\omega_o - c_j^2 \vec{k} \cdot \vec{k}_o)^2 + (2\omega_p^2 \epsilon_j |E_o|^2)(\omega^2 - c_j^2 k^2). \tag{154}$$

If $c_j \to c$ and $\epsilon_j \to \frac{1}{2}q$, this is the dispersion relation given by Max et al. in Eq. (7) of their paper.

For filamentation, $\vec{k}_o \cdot \vec{k} = 0$ and if we assume that $\omega << c_j k$ we find

$$\omega = \frac{ic_j k}{2\omega_o} \left(2\omega_p^2 \epsilon_j |E_o|^2 - k^2 c_k^2\right)^{1/2}. \tag{155}$$

Therefore, the threshold k for stability is

$$kc_j < \sqrt{2}\ \omega_p \epsilon_j^{1/2} |E_o| \tag{156}$$

while the maximum growth rate is

$$\omega = \frac{i\omega_p^2 \epsilon_j |E_o|^2}{2\omega_o} \tag{157}$$

and it occurs for

$$kc_j = \omega_p \epsilon_j^{1/2} |E_o|. \tag{158}$$

The assumption $\omega << c_j k$ is easily verified a posteriori. On the other hand, the situation is more complicated for the modulational instability since $k \cdot k_o = kk_o$. For this case, $\omega \equiv k \cdot v_g + \delta\omega$ where $v_g \equiv c_j^2 \frac{k_o}{\omega_o}$. We now assume that $\delta\omega << kc$ to obtain the dispersion relation

$$\left(\frac{\omega_p^2}{\omega_\delta^2} k^2 c_j^2\right)^2 - 4(\delta\omega\ \omega_o)^2 + 2\omega_p^2 \epsilon_j |E_o|^2 \frac{\omega_p^2}{\omega_\delta^2} k^2 c^2 = 0 \tag{159}$$

so

$$\delta\omega = \frac{i\omega_p}{\omega_o}\frac{kc}{2}\left(2\omega_p^2\epsilon_j|E_o|^2 - \frac{\omega_p^2}{\omega_o^2}k^2c^2\right)^{1/2}. \tag{160}$$

The threshold k is now

$$kc < \sqrt{2}\,\omega_o\epsilon_j^{1/2}|E_o| \tag{161}$$

a factor $\frac{\omega_o}{\omega_p}$ larger than for filamentation. The maximum growth rate is still

$$\omega = \frac{i\omega_p^2}{2\omega_o}\epsilon_j|E_o|^2$$

and it occurs for

$$kc = \omega_o\epsilon_j^{1/2}|E_o|, \tag{162}$$

which, just as the threshold k, is a factor $\frac{\omega_o}{\omega_p}$ larger.

For plasma waves and light waves near the critical density $\left(\frac{\omega_p}{\omega_o} \simeq 1\right)$, the $\delta\omega$ for the modulational instability is identical to the ω for filamentation. This could have been predicted simply by noticing that $v_g << c_j$ for these cases so that the inequality $\omega^2 << k^2c_j^2$ still holds for modulational instability.

Hidden in the analysis given above, when done for light waves, are several assumptions. These become explicit in the analysis of

Max et al.[48] First, it is assumed that the electron density is driven by the $\vec{v} \times \vec{B}$ force of the pump and the decay light wave. This $\vec{v} \times \vec{B}$ force has a low-frequency (ω) component and a high-frequency component $\omega \pm 2\omega_o$. The derivation implicitly neglects the former in preference for the latter. When the former dominates, the process is called Forward Raman Scatter and the density perturbation is a normal mode, i.e., $\omega = \omega_p$. This can be summarized by the inequality

$$1 << \frac{\omega_p^2}{k^2c^2} . \tag{163}$$

When this is satisfied, a distinction between Forward Raman is valid and relativistic self-modulation exists. When it is not satisfied the original assumption was invalid and therefore only Forward Raman exists. Substituting the k corresponding to the mode with maximum growth rate, given in Eq. (162), into Eq. (163) leads to the inequality

$$|E_o|^2 << \frac{\omega_p^2}{\sqrt{2}\ \omega^2 \epsilon_j} . \tag{164}$$

This inequality is not satisfied for parameters of interest to the PBWA. Therefore, relativistic self-modulation of light waves will not occur. Second, a complete derivation[48] assumes that $\omega < \frac{\omega_p^2}{\omega_o}$ in order to obtain the dispersion relation in the form of Eq. (154). For self-modulation $\omega \simeq kv_g \simeq kc$ so this inequality can be rewritten as

$$k < \frac{\omega_p^2}{\omega_o c} \Rightarrow \alpha_o < \frac{\omega_p^2}{\omega_o^2} \tag{165}$$

which is an even stronger constraint. When this inequality is not satisfied, then the growth rate needs to be recalculated from the fuller dispersion relation[48] and then Eq. (163) needs to be checked. On the other hand, inequality (163), for filamentation, is

$$|E_o|^2 << \frac{1}{\sqrt{2}\epsilon_j} , \tag{166}$$

which is valid for parameters of interest.

Typically, the unstable wave number for plasma wave filamentation is less thant ω_p/c. Hence, as the instability evolves, components of the electric field in the transverse (y for slab geometry) directions become important. When this occurs, the full set of coupled wave equations describing electrostatic waves needs to be used.

We close this discussion by noting that a power threshold can be inferred from the threshold condition. If the transverse profile is assumed to be $|\cos \pi \frac{x_\perp}{L}|$ for $|x_\perp| < \frac{1}{2}$ and the system is periodic in L, then the $k_\perp = 0$ mode is unstable into the $k_\perp = \frac{2\pi}{L}$ mode if

$$\frac{c^3}{2\omega_p^2 \epsilon} < \frac{c|\frac{2}{\pi} E_o|^2}{\left(\frac{2\pi}{L}\right)^2} \tag{167}$$

The right-hand side is proportional to the power flux in a fila-

ment. Changing back from the normalized units for E_o gives the power threshold condition

$$P > \frac{\pi^3}{16} c\left(\frac{mc^2}{e}\right)^2 \frac{\omega_o^2}{\omega_p^2} = 16.9 \frac{\omega_o^2}{\omega_p^2} \text{ GW} \tag{168}$$

for linearly polarized light waves. This power threshold is identical to the conclusions of the work by Horton and Schmidt[62] and Sprangle and Tang[61] except for a small numerical factor. This is not surprising since, after all, the physical mechanism is the same for whole beam self-focusing and filamentation.[64]

In collinear optical mixing at least two light waves are present. To lowest order the simultaneous self-focusing of two light waves can be described by the following coupled wave equations.

$$\left[\frac{\partial^2}{\partial t^2} - c^2\nabla^2 + \omega_p^2\left(1 - \varepsilon_1|E_1|^2 - \varepsilon_2|E_2|^2\right)\right]E_1 \tag{169}$$

$$\left[\frac{\partial^2}{\partial t^2} - c^2\nabla^2 + \omega_p^2\left(1 - \varepsilon_2|E_1|^2 - \varepsilon_1|E_2|^2\right)\right]E_2 \tag{170}$$

where $\varepsilon_1 = \frac{1}{2}\left(\frac{3}{4} - \frac{\omega_1^2 - \omega_p^2}{4\omega_1^2 - \omega_p^2}\right)$ for linearly polarized light waves and $\varepsilon_2 = \frac{3}{4}$. We simplify the problem by assuming that initially the magnitudes are equal, $E_1 = E_2$, and that $\omega_{1,2} >> \omega_p$. For this situation the light waves will evolve almost identically. The two coupled equations can, consequently, be merged into the single equation

$$\left\{\frac{\partial^2}{\partial t^2} - c^2\nabla^2 + \omega_p^2\left[1 - \left(\epsilon_1 + \epsilon_2\right)|E_1|^2\right]\right\}E_1. \qquad (171)$$

By replacing $\epsilon_j \rightarrow \epsilon_1 + \epsilon_2$ in Eq. (146), we immediately obtain the threshold k condition for filamentation as

$$k^2c^2 < \sqrt{2}\,\omega_p|E_o|^2\left(\epsilon_1 + \epsilon_2\right). \qquad (172)$$

The growth rate and most unstable k are also analogously obtained.

The presence of a plasma wave can enhance self-focusing of light. The plasma wave influences the light wave through the relativistic motion of the electron in the plasma wave. To see this we write down the wave equation for one light wave in the presence of another light wave and a plasma wave. The full wave equation is now

$$\left[\frac{\partial^2}{\partial t} - c\nabla^2 + \omega_p^2\left(1 - \epsilon_1|E_1|^2 - \epsilon_2|E_2|^2 - \epsilon_p|E_p|^2\right)\right]E_1 \qquad (173)$$

where E_p is the normalized electric field of the plasma wave and $\epsilon_p = 1/4$. Following the procedure of Kaw, Schmidt, and Wilcox,[63] the spatial scale of an equilibrium laser profile is then

$$\frac{c}{\omega_p}\left[\left(\epsilon_1 + \epsilon_2\right)|E_1|^2 + \epsilon_p|E_p|^2\right]^{-1/2} \qquad (174)$$

The inclusion of E_p into the filamentation derivation is more difficult since it is necessary to include the dependence of E_p on E_1 into the coupled equations. There are several ways E_p and E_1 are

coupled. The first is the result of BWE. Early in time, before relativistic detuning (for laser beams with no rise time) $E_p = \frac{\bar{t}E_1E_2^*}{4} = \frac{\bar{t}|E_1|^2}{4}$ where $\bar{t}$ is the time measured from the head of the laser pulse. Substituting this into the wave equation and undertaking the same stability analysis given earlier gives the modified threshold condition

$$\frac{ck}{\omega_p} < \left(\epsilon_1 + \epsilon_2\right)|E_1|^2 + \frac{\epsilon_p \bar{t}^2}{8}|E_1|^4\Big)^{1/2} \qquad (175)$$

for a given k. BWE can also filament the laser light when it breaks up into filaments as the result of relativistic detuning. The breakup of the plasma wave was illustrated in Sec. IIIB7 where 2-D BWE from finite size pumps was discussed.

The second is Raman Side Scatter (RSS). This instability will be discussed shortly. It is the decay of a light wave (ω_1, k_1) into another light wave of frequency ($\omega_1 - \omega_p$, $\vec{k}_1 - \vec{k}_p$) and a plasma wave. Therefore, the high-frequency (ω_2) pump can decay into a plasma wave with $k = \vec{k}_p + \delta\vec{k}_\perp$ and $\omega \simeq \omega_p$. This can beat with the lower frequency pump (ω_2) to generate a light wave at $\omega_2 + \omega_p \simeq \omega_1$ and $\vec{k}_2 + \vec{k}_p + \delta\vec{k}_\perp \simeq k_1 + \delta\vec{k}_\perp$. In addition, the daughter light wave can beat with the beat plasma wave and produce a light wave of ω_1, $k_1 + \delta\vec{k}_\perp$. This is precisely what filamentation of light would produce. Furthermore, if $\delta\vec{k}_\perp$ corresponds to an unstable mode for filamentation it can be further amplified.

The third way that the plasma wave influences the light waves is that the plasma wave itself can go unstable and the region of

unstable $k_\perp$'s overlaps that of the light wave(especially in a warm plasma). This is further complicated by the fact that RSS may create plasma waves that seed plasma wave filamentation. We stop here with the reader hopefully believing that this problem is extremely complicated.

We close this section with the comment that although the stability analysis was done for plane wave pumps, it can still be useful for nonplanar pumps. For example, if as is done in some simulations the laser beam is modeled as one system with an infinite number of image systems (periodic boundary conditions in the tranverse dimension), then it could be constructed from only a few discrete perpendicular k modes. If the ratio of the beam size to the system size is small enough, then the k = 0 mode will be largest. When the other modes are unstable for the k = 0 modes pump strength, then they can be viewed as enhanced noise sources. This description was successful earlier to obtain a self-focusing threshold.

IVB2. Ponderomotive Force Driven Instabilities of Electromagnetic Waves

In this section we briefly discuss instabilities that are driven by the ponderomotive force of electromagnetic waves. The instabilities to be discussed are SBS, SRS, and filamentation.

IVB2a. SRS

Stimulated Brillouin Scattering is the resonant decay of a

light wave into another light wave and an ion acoustic wave. The situation of most interest is when the second light wave moves in the opposite direction to the incident wave and this is called Brillouin backscatter. The ion acoustic wave moves in the direction of the incident wave--the forward direction. SBS is of concern for several reasons. First, it can reflect a large fraction of the incident light, thereby decreasing the efficiency. Much of the past research[10,11,57] on SBS was concerned with this very problem as it related to laser fusion. Second, the resulting ion acoustic wave acting as a density ripple can reduce the peak plasma wave amplitude as discussed in Sec. IIB7. Furthermore, the process gives rise to shorter wavelength mode coupled plasma waves that heat the plasma through wave particle interaction. Third, the backscattered light of one pump and the incident light from the other pump can excite a plasma wave through counterpropagating optical mixing. The phase velocity of this plasma wave is $c\ \frac{\omega_p}{\omega_1}$ which in general is slow and large enough to interact with the background plasma. All three of these effects have already been observed in current long pulse optical mixing experiments. It is assumed that these processes are deleterious to the realization of a high energy accelerator that provides good beam quality.

For reference, we quote the well-known growth rates for SBS.[10,57] It is assumed that the instability of each light wave is independent of the other light wave. The ω and k without subscripts are the frequency and wavenumber of the ion mode. If

$$\frac{T_i}{ZT_e} << 1 \text{ and } \left(\frac{v_o^2}{a_e^2}\frac{\omega_p^2}{\omega_1^2}\frac{1}{8}\frac{c}{c_s}\right)^{1/3} << 1,$$

then

$$\frac{Im\omega}{\omega_p} = \frac{1}{2}\left(\frac{c_s}{c}\right)^{1/2}\frac{v_o}{a_e} . \tag{176}$$

This is referred to as the weakly coupled regime. If the second inequality is not satisfied or, in other words,

$$\left(\frac{v_o^2}{v_{th}^2}\frac{\omega_p^2}{\omega_1^2}\frac{1}{16}\frac{c}{c_s}\right)^{1/3} >> 1$$

then

$$\frac{Im\omega}{\omega_p} = \frac{\sqrt{3}}{2}\left(\frac{m}{M}\frac{\omega_1}{\omega_p}\frac{v_o^2}{c^2}\frac{1}{2}\right)^{1/3} \tag{177}$$

and this is referred to as the strongly coupled regime. In the weakly coupled regime, if $\frac{T_i}{ZT_e} \simeq 1$, then the ion wave is heavily Landau damped since $\omega \simeq kc_s \simeq kv_i$. On the other hand, in the strongly coupled regime ω is determined by the pump and since $\omega >> kc_s$ the ion mode (quasi-mode) is not affected as much when $\frac{T_i}{ZT_e} \simeq 1$. Simulations do indicate, however, that when $\frac{T_i}{ZT_e} \simeq 1$, even strongly coupled SBS is suppressed.

The Brillouin instability can be absolute, and the absolute growth rate is

$$Im\omega_a = \frac{1}{2\sqrt{2}}\frac{v_o}{c}\omega_{pi} . \tag{178}$$

This formula holds even for $\frac{T_e}{ZT_i} \simeq 1$. This is valid for pump strengths such that

$$\frac{Im\omega_a}{2k_o c_s} < 1 \quad \text{or} \quad \frac{1}{4}\frac{v_o}{c}\frac{\omega_p}{\omega_o}\frac{c}{a_e} < 1.$$

We also note, since it is a relevant point for accelerator parameters, that the growth rate tends toward zero when $k^2\lambda_d^2 >> 1$.

The simulation results to be presented later are in agreement with the linear theory when proper comparison could be made. Although in the current experiments SBS plays a major role, we believe it can be avoided by using short laser pulses and/or by making $k^2\lambda_d^2 >> 1$ and/or by making $\frac{T_e}{ZT_i} \geq 1$. Since the convective growth rate is larger than the absolute growth, it dominates initially. Asymptotically, the absolute mode dominates but we are interested in relatively short times. The laser pulse duration times the convective growth rate (for either strong or weak coupling) gives an upper bound on the number of e-foldings of growth. This is true, since the instability pulse convects at a velocity << c. If the instability pulse moved at c, then, the acceleration time rather than the pulse duration, should be used to determine the number of e-foldings. If the number of e-foldings is 0(1) or less, then SBS will not be very important. Another way to avoid SBS is to make $k^2\lambda_d^2 = 4k_o^2\lambda_d^2 \simeq \sqrt{2}\,\frac{\omega_o^2}{\omega_p^2}\frac{a_e^2}{c^2} >> 1$. If $\frac{\omega_o^2}{\omega_p^2} \geq 1000$, then $\frac{a_e^2}{c^2} >> \frac{1}{1000}$ or $T_e >> 25$ eV will satisfy this condition. This is a reasonable electron temperature.

IVB2b. SRS

Stimulated Raman Scattering is the decay of a light wave into another light wave and a plasma wave. When the scattered light is backscattered (RBS), the instability is a resonant three-wave decay process. However, for forward scattered light (RFS) it is a four-wave (nonresonant) modulational type instability in very underdense plasmas. Raman forward scatter has the same physical origin as BWE. The light can also be scattered sideways and this is called side scatter (RSS).

SRS is also important for several reasons. RBS can reflect laser light, although not as efficiently as SBS; and it will generate a plasma wave with a phase velocity $\sim \frac{c\omega_p}{\omega_1}$ that is slow enough to trap background electrons. The trapped electrons can filament from the Weibel instability and this in turn can cause the incoming light to filament.[64] RSS is important because it scatters light out of the interaction regime. It also generates plasma waves that trap the background electrons. RFS is not desired since it broadens the spectrum of the plasma wave moving at c. By RFS we also mean scattering at small angles from the forward direction (SRS which generates plasma waves with $v_\phi \approx c$). It also broadens the light spectrum giving rise to light filamentation. A proper 2-D treatment of cascading in effect studies this very problem.

Below we quote the well-known growth rates for SRS.[10,13] The ω and k without subscripts refer to the frequency and wave number of the low-frequency plasma mode. The growth rate for RBS is

$$\frac{Im\omega}{\omega_p} = \frac{1}{2}\left(\frac{\omega_1}{\omega_p}\right)^{1/2} \frac{v_o}{c} \tag{179}$$

if $\frac{1}{2}\left(\frac{\omega_1}{\omega_p}\right)^{1/2} \frac{v_o}{c} << 1$ and

$$\frac{\omega}{\omega_p} = \frac{1}{2}\left(1 + i\sqrt{3}\right)\left(\frac{v_o^2}{2c^2} \frac{\omega_1}{\omega_p}\right)^{1/3} \tag{180}$$

if $\frac{1}{2}\left(\frac{\omega_1}{\omega_p}\right)^{1/2} \frac{v_o}{c} >> 1.$

RBS can be an absolute instability with the growth rate

$$\frac{Im\omega}{\omega_p} = \frac{\sqrt{3}}{2} \frac{a_e}{c} \frac{v_o}{c} \frac{\omega_1}{\omega_p} . \tag{181}$$

We emphasize these growth rates assume

$$k^2\lambda_d^2 << 1 \text{ or equivalently } \frac{2\omega_1^2}{\omega_p^2} \frac{a_e^2}{c^2} << 1.$$

When this condition is not satisfied, the instability becomes Induced Compton Scattering, which has a much reduced growth rate.

The growth rate for RFS in a very underdense plasma is

$$\frac{Im\omega}{\omega_p} = \frac{1}{2\sqrt{2}} \frac{\omega_p}{\omega_1} \frac{v_o}{c} . \tag{182}$$

There is no absolute instability for this case since $v_{gp} \cdot v_{go} > 0$.

The growth rates for RSS is comparable to those for RBS or RFS depending on the angle of scattering. For most directions it is a

three wave resonant process and its growth rate is reduced from that of RBS by the factor $\frac{2k_o + 2\vec{k}_o \cdot \vec{k}_-}{4k_o^2}$ where $\vec{k}_o$ is the wave number of the pump and $\vec{k}_-$ is the wave number of the decay light wave. For scattering almost in the forward direction the growth rate is the same as for RFS. This process needs to be included in any 2-D treatment of cascading.

The potential importance of SRS can be seen by estimating how many e-foldings occur in a beat wave growth time. The growth time is $\sim\left[\frac{3}{1024}\left(\frac{v_o}{c}\right)^4\right]^{-1/3}\omega_p^{-1}$, while the RBS growth rate is $\frac{\omega_p}{2}\left(\frac{\omega_1}{\omega_p}\right)^{1/2}\frac{v_o}{c}$ so the number of e-foldings is $\left(\frac{1024}{24}\right)^{1/3}\left(\frac{\omega_1}{\omega_p}\right)^{1/2}\left(\frac{v_o}{c}\right)^{-1/3}$. We have neglected any rise time considerations. This gives an upper bound on the number of e-foldings, since the weakly coupled growth rate was used. This number can easily be 0(1-10). Simulations show that indeed this gives a reasonable estimate. However, when RBS occurs the resultant plasma wave quickly traps electrons and breaks. The plasma heats up and RBS goes into the Compton regime. The front of the plasma wave moves across the simulation box at roughly the speed of light. This scenario means that RBS is evolving from various noise sources rather than from a single one. The importance of RBS appears to be how the residual plasma spectrum perturbs the accelerated particles.

RBS can be avoided since typically $k_p^2\lambda_d^2 = 2\left(\frac{\omega_1}{\omega_p}\right)^2\frac{a_e^2}{c^2} >> 1$. We have already shown for $\frac{\omega_1}{\omega_p} = 30$ this only requires $T_e > 20eV$. The growth rate for Induced Compton Scattering is low enough that in general BWE can dominate it. The growth rate of RFS decreases as the laser frequency increases. The importance of RFS will, how-

ever, only really be known when a proper treatment of cascading is done.

IVB2c. Self-Focusing and Filamentation

Previous treatments of whole-beam self-focusing assume that a steady-state density channel has already formed. The simulations demonstrate that this is not a reasonable assumption for large laser power for times of interest. The development of the density channel is strongly influenced by the evolution of relativistic self-focusing and this will be illustrated in the forthcoming simulations. We should mention that recently Sprangle and Tang[61] have examined whole-beam self-focusing of short laser pulses for long propagating distances while keeping the ions fixed.

Filamentation of light waves, as already discussed, is of concern because it will alter the transverse profile of the plasma wave unpredictably. We start from the well-known growth rates.[57]

In the weakly coupled regime, $\frac{1}{2}\frac{\omega_{pi}^2}{\omega_1^2}\frac{v_o^2}{c_s^2}\frac{c^2}{c_s^2} << 1$, the threshold condition for $k_\perp$ is $\frac{ck_\perp}{\omega_1} < \frac{v_o}{a_e}$ and

$$\frac{Im\omega}{\omega_{pi}} = \frac{1}{2}\frac{\omega_{pi}}{\omega_1}\frac{v_o^2}{c_s^2} . \qquad (183)$$

The threshold condition is the same in the strongly coupled regime, $\frac{1}{2}\frac{\omega_{pi}^2}{\omega_1^2}\frac{v_o^2}{c_s^2}\frac{c^2}{c_s^2} >> 1$, and the growth is

$$\frac{Im\omega}{\omega_{pi}} = \frac{1}{\sqrt{2}}\frac{v_o}{c} . \qquad (184)$$

The instability is never absolute. The steady-state spatial growth length is

$$\mathrm{Im}k_{\parallel} = \frac{\mathrm{Im}\omega}{v_{go}} \simeq \frac{\mathrm{Im}\omega}{c} \tag{185}$$

so long as $\frac{v_o}{4v_e}\frac{\omega_p}{\omega_1} << 1$ where $\mathrm{Im}\omega$ is the weakly coupled growth rate. If this inequality is not satisfied, then the expression for the spatial growth length becomes more complicated. Steady state may not necessarily be reached during the acceleration process.

Although it occurs on ion time scales, the temporal growth rate of ponderomotive filamentation can be larager than that of relativistic filamentation, especially at low pump strengths. The ratio of the growth rates for ponderomotive and relativistic filamentation is

$$\frac{4}{\sqrt{2}}\frac{\omega_{pi}}{\omega_p}\frac{\omega_o}{\omega_p}\frac{c}{v_o} \quad . \tag{186}$$

This is small for simulation parameters. However, for current experiments this ratio is larger than unity. For example, for $\frac{\omega_{pi}}{\omega_p} = \frac{1}{43}$, $\frac{\omega_o}{\omega_p} = 10$, and $\frac{v_o}{c} = .03$ the ratio is ~40. This ratio will most probably be near unity for accelerator parameters.

In general though, the PBWA relativistic filamentation is of more concern since in that case an unstable pulse moves at c and, therefore, has the laser pulse propagation distance in which to grow.

Another consideration is that the threshold k for instability

is different in the two instabilities. For relativistic filamentation $\frac{k_\perp c}{\omega_p} < \frac{\sqrt{2}}{2}\frac{v_o}{c}$ while for ponderomotive filamentation $\frac{k_\perp c}{\omega_p} < \frac{v_o}{a_e}$. Even if the beam is narrow enough so that relativistic filamentation cannot occur, it is possible that ponderomotive filamentation could still occur since $\frac{v_o}{a_e} >> \frac{v_o}{c}$.

Previous treatments of whole-beam self-focusing assume that a steady-state density channel has already formed. The simulations demonstrate that this may not be a reasonable assumption for larger laser powers for times of interest. The development of the density channel can be strongly influenced by the evolution of relativistic self-focusing, and this will be illustrated in the forthcoming simulations. When the laser pulse enters the plasma, if it is above the relativistic threshold it will begin to self-focus immediately. On the other hand, the lasers cannot self-focus due to ponderomotive effects until the ions have moved to form a density channel. So, although the temporal filamentation growth rates can be comparable, relativistic self-focusing always occurs first when its power threshold is exceeded. We mention that recently Sprangle and Tang[61] have examined whole-beam self-focusing of short laser pulses for long propagating distances while keeping the ions fixed.

IVB3. Ponderomotive Force Driven Instabilities of Electrostatic Waves

In these sections we briefly discuss plasma wave instabilities that are driven by the ponderomotive force. The instabilities are

parametric decay and the modulational instability.[60]

IVB3a. Parametric Decay and Self-Modulation

Parametric decay is the decay of a plasma wave into another plasma wave and an ion acoustic wave. It is a resonant three-wave interaction. The fastest growing mode occurs when the daughter plasma wave propagates in the backward direction. In order that all three waves in backscatter are normal modes, it is necessary that[60] $k\lambda_d > \frac{4}{3}\left(\frac{m}{M}\right)^{1/2}$. In the weakly coupled regime, $\frac{\sqrt{2}}{4}\ \frac{v_o^2}{a_e^2}\ \frac{\omega_{1e}}{k_o a_e}\left(\frac{M}{m}\right)^{1/2} << 1$, and for $\frac{T_i}{ZT_e} << 1$ the growth rate for backscatter is

$$\frac{Im\omega}{\omega_{pi}} = \left[2\sqrt{2}\ \frac{v_o^2}{a_e^2}\left(\frac{M}{m}\right)^{1/2}\ \frac{a_e}{\omega_p}\ k_o\right]^{1/2}. \tag{187}$$

The strongly coupled growth rate is

$$\frac{Im\omega}{\omega_{pi}} = \frac{\sqrt{3}}{2}\left[\frac{v_o^2}{2}\ \frac{k_o^2}{\omega_p^2}\left(\frac{M}{m}\right)^{1/2}\right]^{1/3} = \frac{\sqrt{3}}{2}\left[\frac{v_o^2}{2c^2}\left(\frac{M}{m}\right)^{1/2}\right]^{1/3}. \tag{188}$$

If the strongly coupled threshold is not satisfied, then when $k\lambda_d < \frac{1}{3}\left(\frac{M}{m}\right)^{1/2}$, parametric decay is no longer possible. The wave is now modulationally unstable with a growth rate

$$\frac{Im\omega}{\omega_{pi}} = 0\left(\frac{\omega_p}{4\omega_{pi}}\ \frac{v_o^2}{a_e^2}\right). \tag{189}$$

When $\frac{v_o}{a_e}$ is large then

$$\frac{Im\omega}{\omega_{pi}} = 0\left[\left(\frac{v_o^2}{a_e^2}\ \frac{m}{M}\right)^{1/4}\right]. \tag{190}$$

In the PBWA, the plasma waves will easily be larger than the strongly coupled parametric decay threshold. (Therefore, we do not discuss the oscillating two-stream instability.) The ratio of its growth rate to the relativistic self-modulation growth rate is

$$\frac{16\sqrt{3}}{3}\left(\frac{2c^4}{v_o^4}\frac{m}{M}\right)^{1/3} \tag{191}$$

where we have substituted $k_o = \frac{c}{\omega_p}$. For a hydrogen plasma, this ratio is larger than unity for $v_{os}/c < 1$. In fact, simulations support this conclusion that parametric decay dominates relativistic self-modulation. Parametric decay is also not easily avoided. Raising the ion mass does not help very much due to the 1/3 power dependence. Since the ion mode is no longer a normal mode, increasing T_i/ZT_e will not affect the stability much. The implication is that significant beam loading needs to be done before strongly coupled parametric decay occurs.

The relativistic driven instability may be ineffectual since in BWE, as argued in Sec. IIB4, the plasma wave's phase velocity depends weakly on amplitude when wavelength shifts are considered. Since the amplitude dependence of the phase velocity drives the modulational instability, its effects may be minimized.

It is also worth noting that the frequency of a plasma wave excited by BWE is always below its normal mode frequency. This is seen in Eq. (26b) of Sec. IIB2a where the frequency shift ($\dot{\phi}$) is

smaller than that in Eq. (24) with F set to zero. However, because the pump is large enough the strongly coupled growth rate of Ref. 60 is still applicable.

Chapter V. SIMULATIONS OF COMPETING INSTABILITIES

VA. Introduction

In Chapter IV various competing instabilities were briefly introduced. (The list is not intended to be complete.) With so many processes it is impossible to attempt an analytical treatment that includes them all. Furthermore, most instabilities have a range of unstable k's, so modes from the same instability compete with each other. It has only been in the last few years that work has been done where even two instabilities have been studied self-consistently.[59] Computer experiments present an attractive alternative, bearing in mind their limitations. In this chapter we present simulations that in some cases isolate a few selected processes and in other cases examine the whole slew of instabilities at once. These simulations represent the first ever serious attempt to examine competing processes in the PBWA. All other published simulations[7,31,32] examined BWE only. Some of this work has been presented elsewhere,[5,15] but is given again so that this chapter is self-contained. The code WAVE was used and the simulation units are the same as before.

The outline of this chapter is as follows. In Sec. VB, simulation results of self-focusing and filamentation of light waves are presented. In Sec. VC1 the SBS instability is examined under two frequency illumination in 1-D. In Sec. VC2 the stability of the plasma wave is investigated primarily in one dimension. The SRS instability is discussed throughout as it relates to the other

instabilities.

VB. Electromagnetic Self-Focusing and Filamentation

In this part we demonstrate via PIC simulations the early and late time evolution of the laser beams for double frequency illumination. Due to computer cost constraints, the size of the simulation box is limited. In order to observe two-dimensional instabilities, it is, therefore, necessary to use large laser powers. This means that many instabilities occur simultaneously making it difficult to isolate processes. Therefore, the philosophy used is to compare simulations in pairs where only one parameter is changed. In this way statements about how the end result depends on parameters can be made, but unfortunately in some cases the reasons for the differences cannot be conclusively inferred.

In Sec. VB1 we examine filamentation and SRS of plane waves. Immobile ions were used so ponderomotive filamentation effects could not occur. In Sec. VB2 relativistic whole beam self-focusing is demonstrated using lasers with various spot sizes. Both mobile and immobile ions were used to clearly identify the ion inertia effects. We present some evidence of resonant relativistic and resonant ponderomotive self-focusing by comparing single and double frequency illumination. Last, in Sec. VB3 we investigate the long-time behavior of the laser beams in these high power simulations.

VB1. Plane Waves

The 2-D simulations in which plane waves were used are II1 through II6 in Table II. In this dissertation, only II3 and II4 will be discussed. The common parameters are $\frac{v_{o1}}{c} = \frac{v_{o2}}{c} = .4$, $T_e = 2.5$ KeV, $\frac{M_i}{m_e} = \infty$, $\tau = 120$, $L_x = 120\ \frac{c}{\omega_p}$, and $L_y = 20\ \frac{c}{\omega_p}$. We begin with the simulation in which $\frac{\omega_{1,2}}{\omega_p} = 4,4$ and $\frac{M}{m} = \infty$. Since the ions have infinite mass, then SBS and ponderomotive filamentation cannot occur. The instabilities that occur are SRS and relativistic filamentation. The pump strength is so large that SRS traps many background electrons. This gives rise to an anistropic distribution function that drives the Weibel instability. Furthermore, as the plasma heats up SRS turns into induced Compton Scattering. These two additional processes make it difficult to obtain clean results. This problem exists for all the 2-D simulations. RBS and RSS have the largest temporal growth rates so they appear before all other instabilities. The temporal growth rates for RFS and relativistic filamentation are comparable for $\frac{v_o}{c} \sim 1$.

This simulation is summarized in Fig. 24. In Fig. 24a we plot $\frac{E_z^2}{8\pi}(k_x, k_y)$ at $\omega_p t = 180$ where the pump is clearly the dominant mode. The modes with k_x smaller than that of the pump corespond to SRS, while the modes with k_x equal to that of the pump represent filamentation. Later in time, the same plot shows that SRS disappears while the filamentation modes ($k = \vec{k}_o \pm \delta\vec{k}_\perp$) persist. We plot $|E_z|$ vs. x for various k_y's in Fig. 24b at $\omega_p t = 360$. The k_y's are plotted as mode numbers where $n = \frac{L_y}{2\pi} k_y$. At this time mode 1 dominates and it grows to the right. From Eq. (158) we find the fastest growing mode for relativistic filamentation is $\frac{ck_y}{\omega_p} = .4$ or

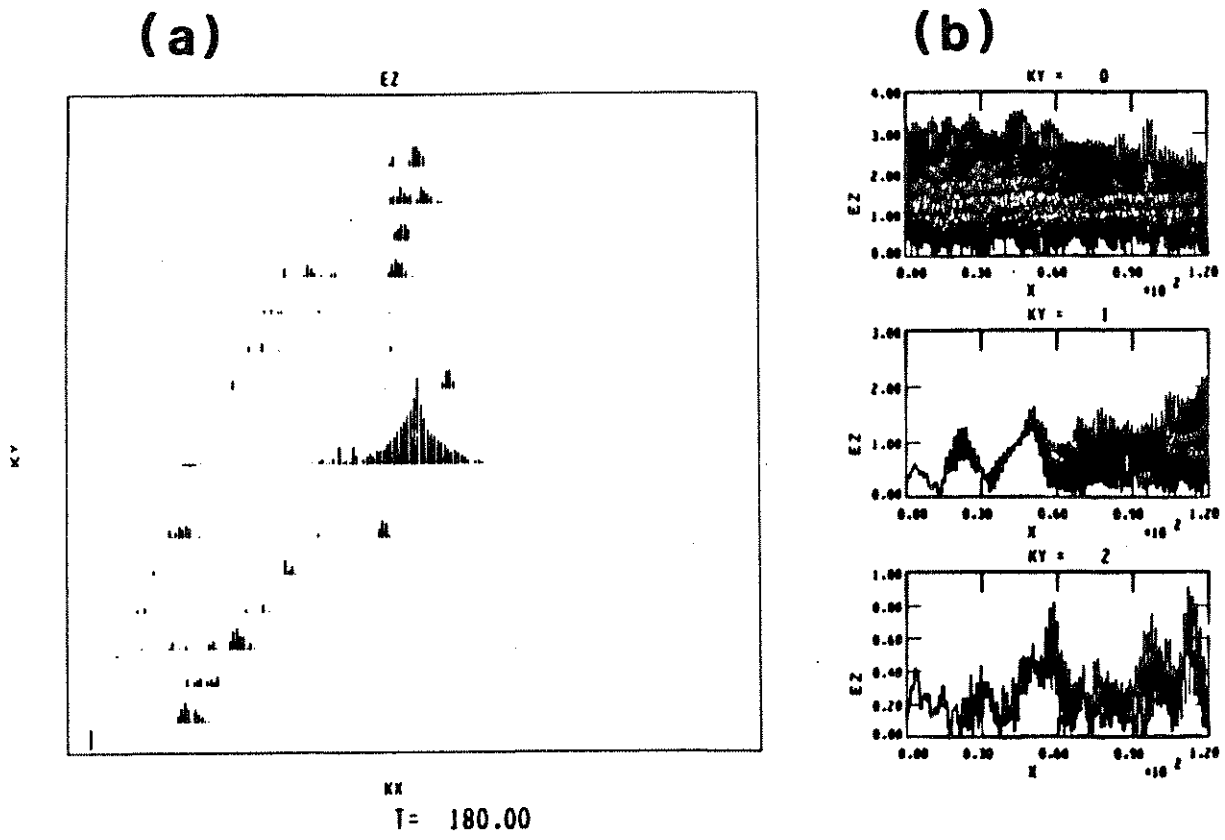

Figure 24. (a) The $\vec{k}$ spectrum of the electromagnetic field energy $E_z^2/8\pi(\vec{k})$ is presented at $\omega_p t = 180$. (b) The absolute value of E_z vs. x for various k_y's. k_x is in units of $2\pi/L_x$ and k_y is in units of $2\pi/L_y$ at $\omega_p t = 360$.

$n = 1.27$ and from Eq. (157) we find that it has a spatial growth length of 50 $\frac{c}{\omega_p}$. (The spatial growth rate is the temporal growth rate divided by the group velocity of light in this case.) We expect, therefore, a few e-foldings of growth over the length of the simulation box. For normal noise levels this would not be significant. In these high intensity simulations the noise level appears to be enhanced from the competing instabilities. We have published simulations that describe one such mechanism in more detail elsewhere.[64] In fact, in that case even though the laser intensity was below the relativistic filamentation threshold filaments were still seen. The difference is that here they could be amplified.

To clearly identify the importance of these processes to BWE, we carried out an identical simulation except that $\frac{\omega_{1,2}}{\omega_p} = 5,4$. This is simulation II4 in Table II. If we assume that the instabilities of one laser beam are independent of the other, then the growth rates will be reduced because now each beam has $\frac{v_o}{c} = .4$ while before, one beam had $\frac{v_o}{c} = .8$.

We start by examining the longitudinal field E_x at a time when it has reached its peak amplitude. We plot in Fig. 25 both E_x vs. x at $y = 10c/\omega_p$ and E_x vs. y at $x = 20c/\omega_p$ at the same time $\omega_p t = 120$. The E_x vs. x plot matches the 1-D simulation result. However, the E_x vs. y plot shows that there is significant variation across a wavefront. Note that the slice in Fig. 25b is not through the maximum or minimum of a wavefront. The perturbations are due to the background noise and SRS. The SRS instability in

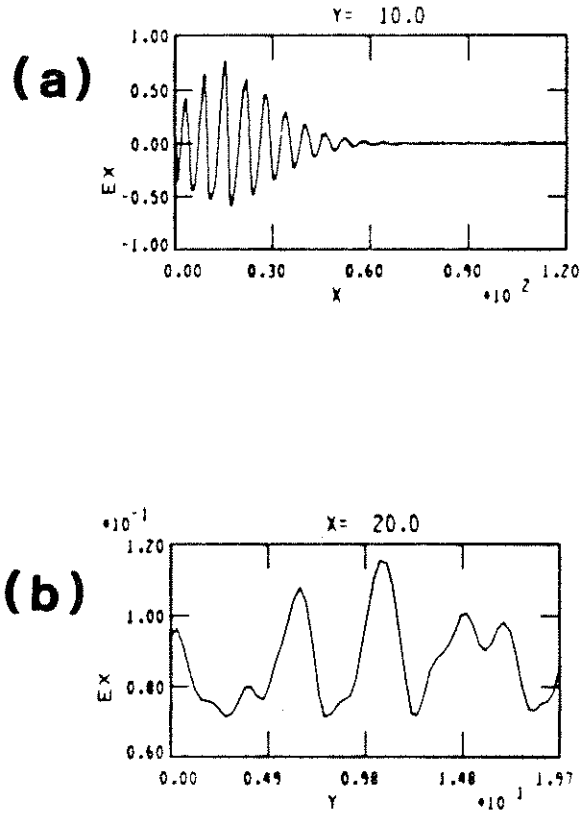

Figure 25. The longitudinal field E_x plotted vs. (a) x at y = $10c/\omega_p$ and (b) y at x = $20c/\omega_p$ at the same time $\omega_p t = 120$.

this case occurs when the E_x driven by BWE decreases from relativistic detuning.

The low-frequency pump (ω_2) and the next cascaded mode ($\omega_2 - \omega_p$) appear to Raman backscatter, while the high-frequency pump does not. Later in time SRS is predominantly in the forward direction ($\vec{k}_p + \delta\vec{k}_2$). The residual plasma waves can beat together with the cascaded mode and the low-frequency pump, or the residual light waves can beat with the beat excited plasma wave to create light waves at (ω_1, $k_1 + \delta k_\perp$) and (ω_2, $k_2 + \delta k_\perp$). This is similar to cascading but in two dimensions. This occurs more strongly than in the single frequency run because the low-frequency light wave in BWE does not grow from noise.

To compare the extent of filamentation between the single frequency and the double frequency simulations, the contour plot of the laser field E_z at $\omega_p t = 360$ is presented in Fig. 26 from each simulation. The filamentation is clearly stronger under double fre- quency illumination. The filamentation is more coherent and over a larger area of the simulation box. The perpendicular wavelength is also shorter.

The simulations demonstrate that under double frequency illumination the plasma wave initially exhibits 1-D like properties. The wavefronts are eventually perturbed by the occurrence of RSS. It is necessary, therefore, to determine how broad a spectrum of slower phase velocity waves is tolerable for the beam quality requirements of particle acceleration. Later in time filamentation is severe. The plasma wave, however, is turbulent by this

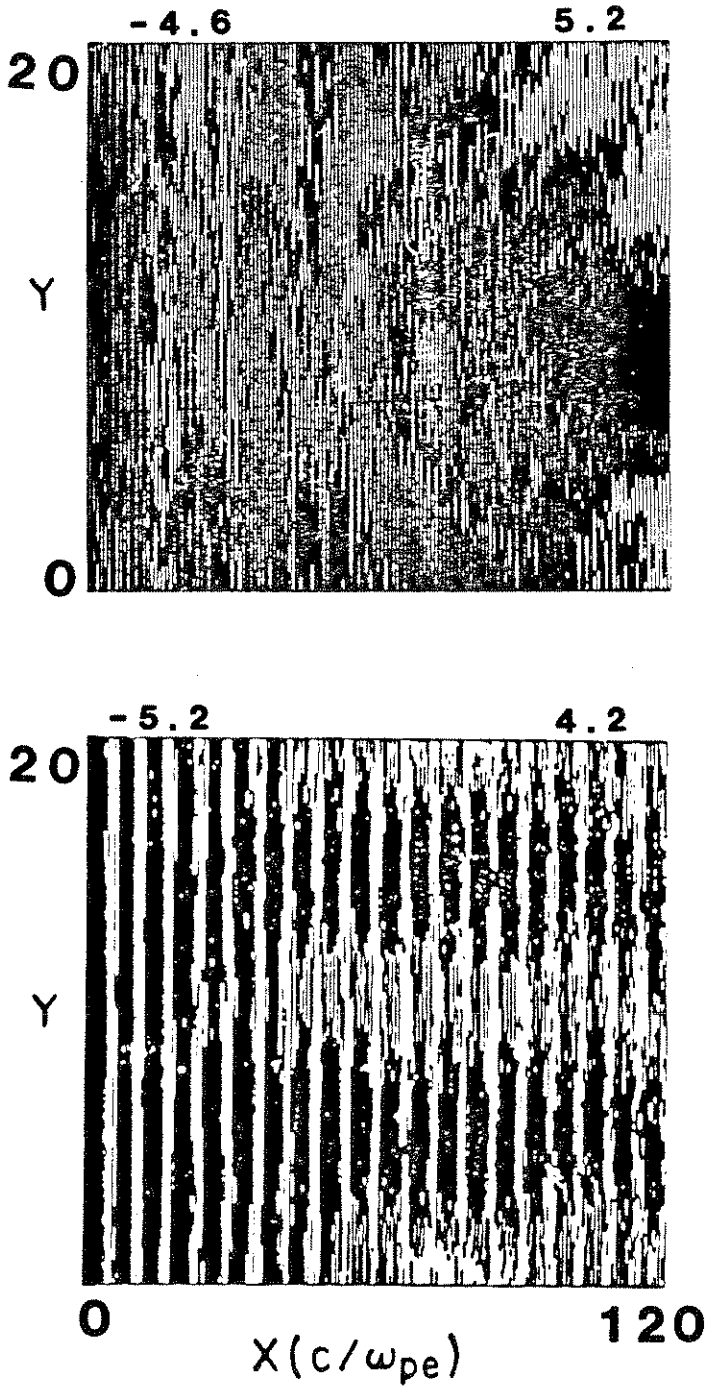

Figure 26. Contour plots of E_z at $\omega_p t$ = 360 for (a) single frequency and (b) double frequency illumination. The values of the minimum and maximum contours are given.

time. The propagation distance increases as ω_o^2/ω_o^2, while the relativistic self-focusing growth rate decreases as ω_o/ω_p. The number of e-foldings might therefore increase as ω_o/ω_p is increased. This topic, therefore, deserves more investigation for realistic laser profiles and background noise.

VB2. Finite Wave Fronts

We discuss simulations of illumination with finite wavefronts. These are simulations II7 through II18 in Table II. Common parameters are $\frac{v_{o1}}{c} = \frac{v_{o2}}{c} = .56$, $T_e = T_i = 2.5$ KeV, $L_x = L_y = 60\ \frac{c}{\omega_p}$, and each laser beam has a $\cos^2 \frac{\pi y}{L_o}$ profile. The value of L_o is varied, while the profile is the same in every finite beam simulation. We begin with simulations II7 and II8. In both simulations $\frac{\omega_{1,2}}{\omega_p} = 5,4$, $L_o = 20\ \frac{c}{\omega_p}$, and $\tau = 300\omega_p^{-1}$. The difference between these two simulations is that in one case the ions are a smooth uniform fixed background, while in the other they are discrete with $\frac{M_i}{m_e} = 1836$. The laser power used is above the relativistic self-focusing threshold. This is seen by noticing that for $\frac{v_{o1}}{c} = \frac{v_{o2}}{c} = .56$ the spatial scale given by Eq. (174) is considerably smaller than $L_o = 20\ \frac{c}{\omega_p}$. Further confirmation is that condition (167) is also satisfied.

Relativistic self-focusing is illustrated in Fig. 27 where the contour plot of the laser field E_z is shown at $\omega_p t = 330$ for fixed ions. The self-focusing first occurred near $\omega_p t \simeq 200$. The value of $\frac{E_z^2}{8\pi}$ on axis at the right is double that of the left. The laser's spot is reduced to $\sim 5\ \frac{c}{\omega_p}$ as it self-focuses. This is roughly the

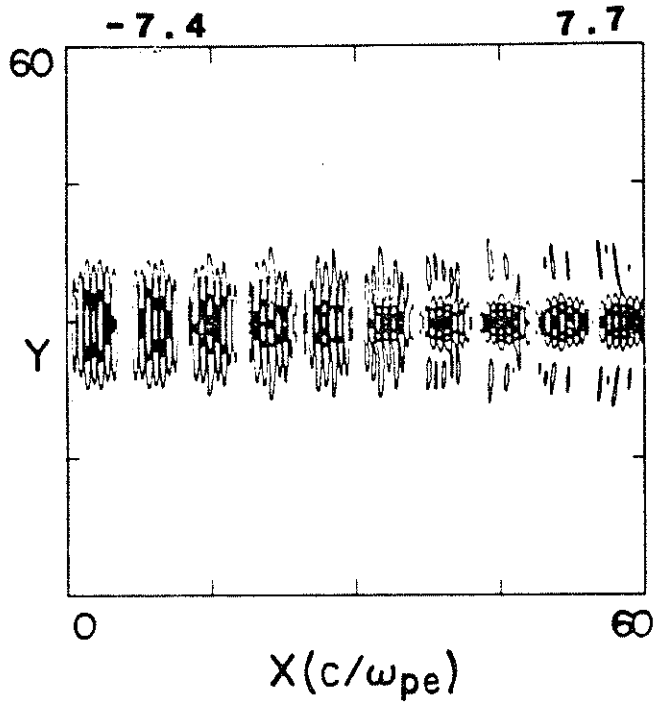

Figure 27. The contour plot of the lasers' field E_z at $\omega_p t = 330$ for fixed ions. The values of the minimum and maximum contours are given.

equilibrium radius predicted by Eq. (174). The plasma wave is neither coherent nor planar at this time. This is due in some part to wave particle interactions. The plasma wave traps the background electrons in these high intensity simulations. We also point out that toward the right-hand boundary an electron density channel exists. This occurs despite the fact that the ions are stationary. The ponderomotive force is large enough to balance the space charge attraction (electron pressure is negligible since $\frac{v_o}{a_e}$ >> 1). It will be shown shortly that with mobile ions the channel properties are qualitatively different.

At earlier times, the lasers' profile is influenced by the plasma wave. This is shown in Fig. 28 where a plot of E_x vs. x and E_z vs. x for $y = 30c/\omega_p$ are shown at $\omega_p t = 180$. The splitting structure of the plasma wave occurs first and it arises from relativistic detuning. The presence of the plasma wave scatters the incoming light due to the modification to the index of refraction from both density and relativistic effects. The net effect is that the driver gets altered and this feeds back to the plasma wave. This scenario is two-dimensional cascading.

In this simulation SRS does not appear to be important. The amount of reflected light is ≃ .1 percent. The absence of significant SRS is partially due to the narrow laser beam since RSS does not have enough distance to exponentiate.

In the mobile ion simulation there are no significant differences in the initial stages of the plasma wave growth. Since the ions are now discrete, the background fluctuation level is larger

(a)

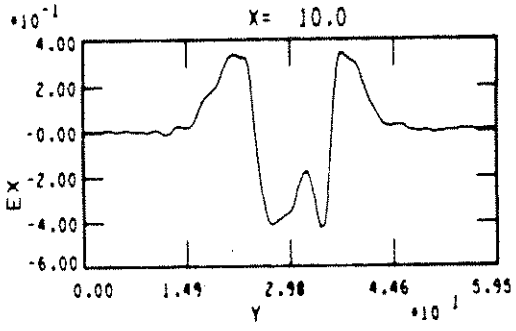

(b)

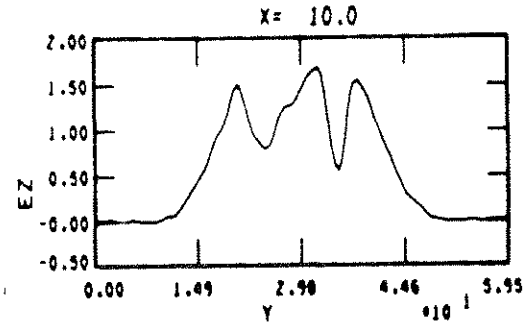

Figure 28. The (a) longitudinal field E_x vs. x and (b) the lasers' field E_z vs. x at $\omega_p t$ = 180 for y = 30 c/ω_p. The value of L_o is 40 c/ω_p.

and this can explain any differences. Later in time, an ion channel forms which initially enhances the self-focusing. This is illustrated in Fig. 29 where the x-y, V_y vs. x, and V_y vs. y ion phase space are plotted and in Fig. 39 where the E_z contour plot is plotted at $\omega_p t$ = 420. The ponderomotive force pushes the electrons out. The resulting space charge field then pulls out the ions. The space charge field is approximately equal to the ponderomotive force. As the ions are expelled and the channel width gets larger, the beam begins to expand as seen in Fig. 30. This did not occur in the fixed ion case. The position in x at which this occurs moves toward the right. This will be shown later in the long-term behavior section. The time it takes for the channel to form can be estimated by calculating how long it takes an ion to move a fraction of the beam radius under the influence of the ponderomotive force. Following this procedure we find

$$\omega_{pi}t = \frac{\alpha^{1/2} L_o}{\langle E_1^2 + E_2^2 + E_p^2 \rangle^{1/2}} \text{ and } \frac{v_i}{c} = \frac{m}{M} \frac{ct}{L_o} \frac{1}{2} \langle E_1^2 + E_2^2 + E_p^2 \rangle$$

where L_o is the beam diameter, α is the fraction of the beam radius an ion moves, and $\langle E_j^2 \rangle$ is the time average of the normalized fields intensities. Using L_o = 20, α = 1/4, and $\langle E_j^2 \rangle$ = 1/4 gives an approximate time of $\omega_{pi}t$ = 10. (This is in reasonable agreement with the simulations as seen in Fig. 29b.) The maximum velocity calculated by the same arguments is also in agreement. As the laser beam self-focuses from relativistic effects, L_o decreases and, if absorption is ignored, E_1, E_2, and E_p increase. Both

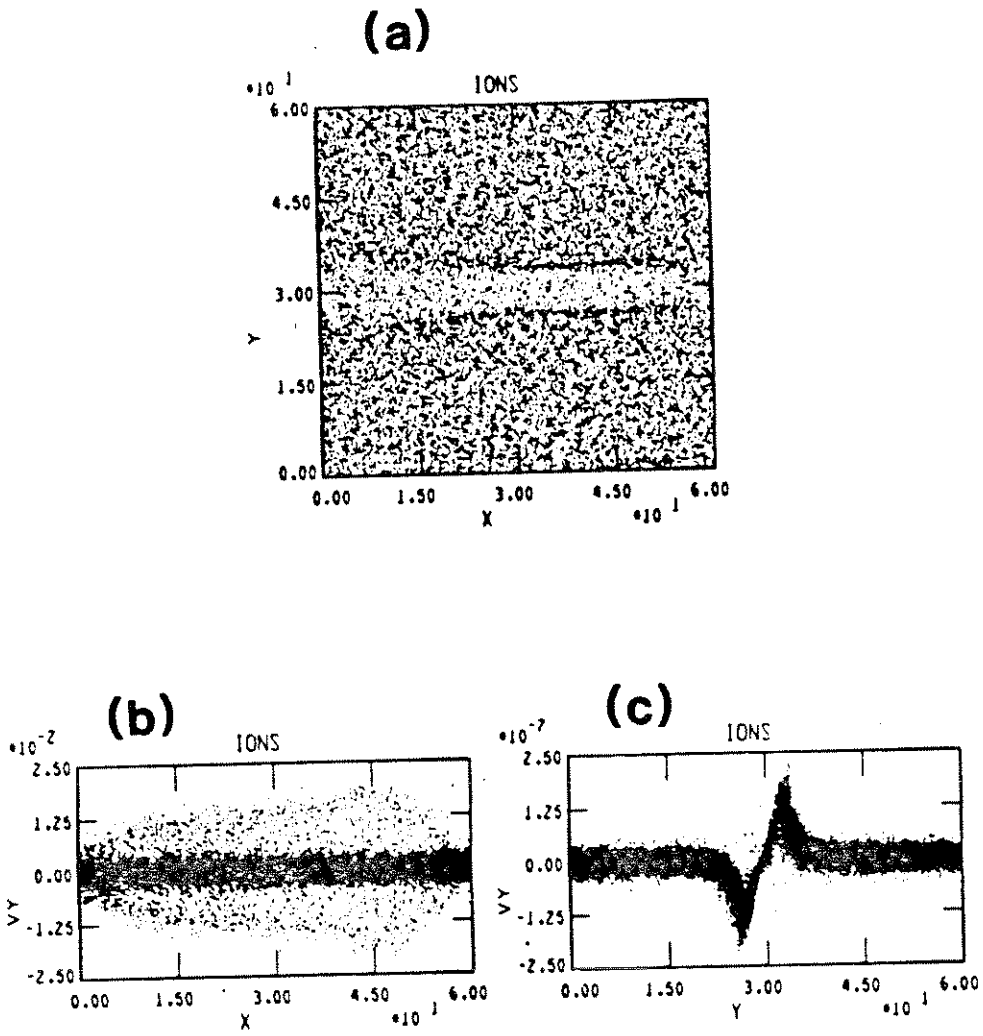

Figure 29. The (a) x-y, (b) V_y vs. x, and (c) V_y vs. y ion phase ϕ space plots of $\omega_p t = 420$. Simulation parameters are $\alpha_1 = \alpha_2 = .58$, $\tau = 300\omega_p^{-1}$, and $L_o = 20\ c/\omega_p$.

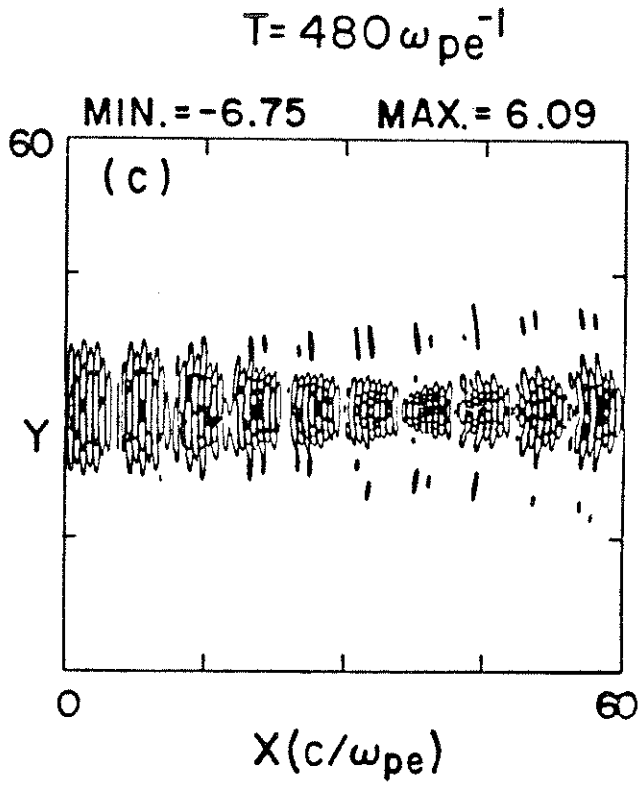

Figure 30. (a) The contour plot of the lasers' field E_z at $\omega_p t$ = 480. The value of L_o = 20 c/ω_p. The values of the minimum and maximum contours are given.

effects cause the ponderomotive force to increase and, consequently, cause the channel formation time to decrease. More will be said on this when simulations with $L_o = 40 \frac{c}{\omega_p}$ are presented. The transverse ion velocities are largest on the right because the laser beam is self-focusing. This is shown in Fig. 29b in the V_y vs. x phase space plot.

In the V_y vs. y phase space plot in Fig. 29c it is demonstrated that the ponderomotive force acts like a piston and sets up a shock front. The ion velocities are larger than the ion sound speed by roughly a factor of 5. It will consequently take a long time before any equilibrium is established. The ion channel is largest on the left. This seems to contradict the observation that the ion transverse velocities are largest on the right. The resolution is that, since the laser beam has self-focused, the beam is narrower and the electric field is larger on the right. The ponderomotive force is consequently larger, so the velocity is larger. The channel width is determined by the integral of the velocity over time. So, even though the velocity was larger on the right at this time, the integral of the velocity over time was smaller.

In simulation II11 the laser spot size is doubled. Since the laser intensity is kept constant, the laser power is further above the relativistic self-focusing threshold. The laser is amplified more than in the smaller spot size simulations. This is demonstrated in Fig. 31 where the contour plot of the light leaving the right-hand boundary is presented at $\omega_p t = 307$. This time is chosen since the ions have essentially not played a role yet, so the

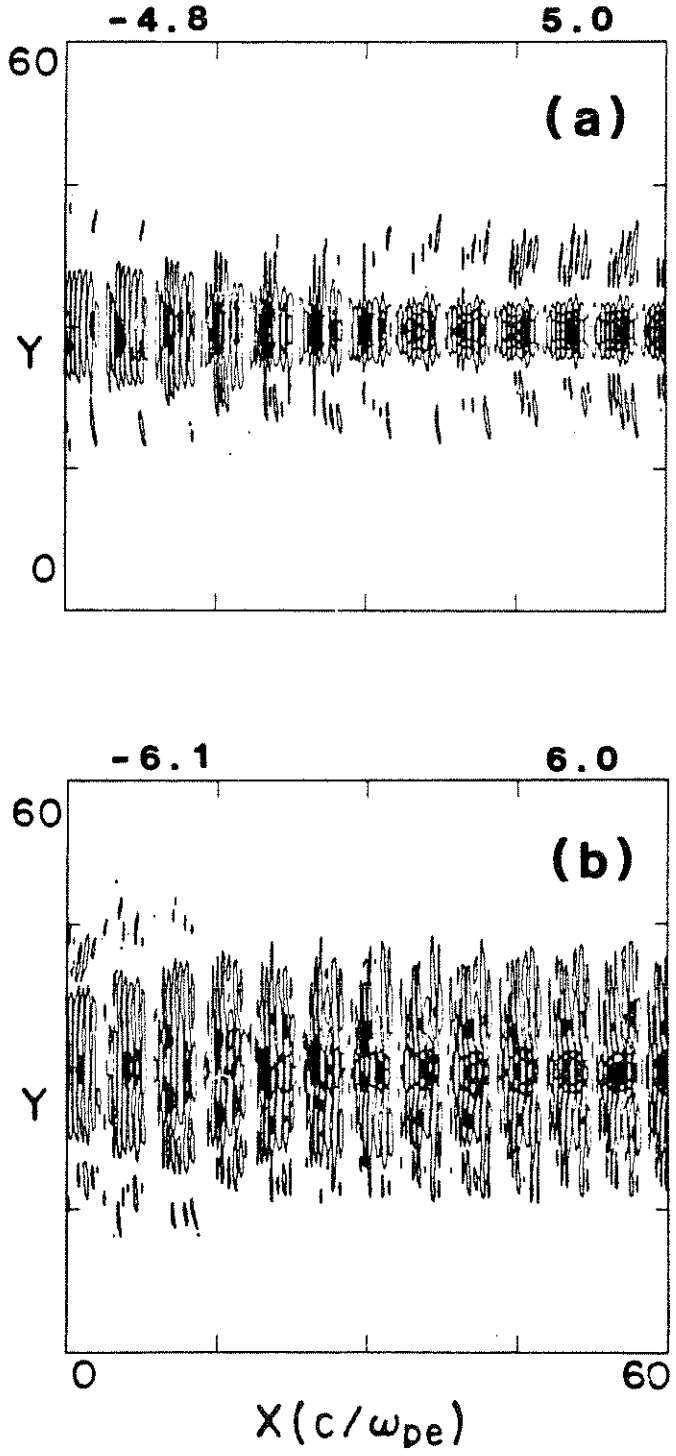

Figure 31. The contour plot of the lasers' field E_z leaving the right-hand boundary at $\omega_p t$ = 307 for (a) L_o = 20 c/ω_p and (b) L_o = 40 c/ω_p. The values of the minimum and maximum contours are given.

relativistic effects are isolated. From Fig. 31a where $L_o = 20\ \frac{c}{\omega_p}$, the peak value of E_z is determined to be 6.3. In these units the input value of E_z is 4.3. This is to be contrasted with Fig. 31b where E_z is found to be 7.7. In terms of intensity, this is a 50-percent difference. The focused radii are $\sim 5\ \frac{c}{\omega_o}$ in both cases. We also mention that the plasma wave scatters light, as before, early in the simulation when the plasma wave is large and coherent.

The increase in the laser intensity leads to larger transverse ion velocities. However, due to the larger initial beam radius, the ion channel takes longer to form. The ponderomotive force creates a shock, as before, making it impossible for any equilibrium density profile to be attained during the simulation. As the channel forms it initially leads to further amplification. In the $L_o = 40\ \frac{c}{\omega_p}$ case a factor of 4 increase in intensity over the length of the box is observed at $\omega_p t = 540$, while the laser spot reduces to $\simeq 2\ \frac{c}{\omega_p}$. This is shown in Fig. 32a.

The larger value of L_o leads to ponderomotive filamentation late in the simulation. This is evident in Fig. 32b where a contour plot of E_z leaving the right-hand boundary is given at $\omega_p t = 768$. The amplification is not as large as at either $\omega_p t = 307$ or 540 and this is because the plasma has been evacuated from the beam region. This, in effect, eliminates the dielectric properties of the plasma. Instead, the channel becomes a waveguide. However, as the ions are evacuated they initially pile up at the edge of the beam, giving rise to large spikes in the ion density. As the ion channel continues to evolve, the density spikes "radiate" ion

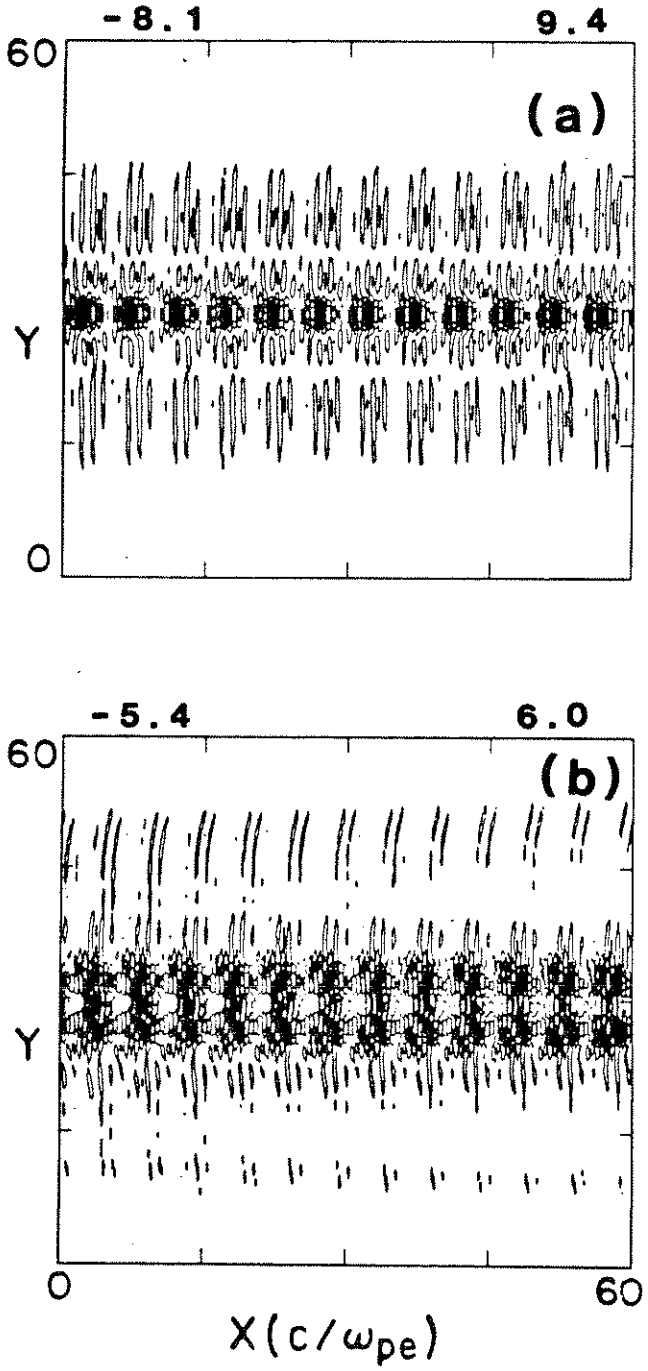

Figure 32. The contour plot of the lasers' field E_z leaving the right-hand boundary for L_o = 40 c/ω_p at (a) $\omega_p t$ = 540 and (b) $\omega_p t$ = 768. The values of the minimum and maximum contours are given.

fluctuations. These fluctuations then appear to seed ponderomotive filamentation at the edge of the beam.

When the lasers' rise time is increased from τ = 300 to τ = 800, the amount of amplification decreases. This is determined from simulation II12 where the maximum amplification was a factor of 3 in laser power. This occurred at $\omega_p t \simeq 900$. The $\frac{v_{os}}{c}$ threshold necessary for self-focusing for this beam profile is ~.3. This is roughly one-half the peak value. From the form of h(t), this does not occur until a little past $\tau/2$. In this simulation the first sign of self-focusing is near $\omega_p t$ = 450 and it is predominantly the result of relativistic effects, since the ions have hardly moved by this time. The ions do, however, move soon afterward and this will be shown shortly. It seems, from these simulations, that the amplification is largest when the onset of relativistic and ponderomotive effects are clearly separated in time. In this simulation there is no clear separation in time between the two types of self-focusing.

Late in the simulation filamentation is also observed, just as in the $\tau = 300\omega_p^{-1}$ simulation. The filamentation is observed around $\omega_p t$ = 850 or at the peak of the laser rise time. The amplification for filamentation is larger than in simulation II11. The reason is that the channel is not completely formed, so the whole beam is being amplified rather than merely being trapped while it filaments.

To clearly identify the differences between single and double frequency illumination, simulation II14 was conducted. Self-

focusing is observed in the single-frequency case at nearly the same time $\omega_p t = 500$, as in simulation II12; but it is not nearly as strong. The reason seems to be due to the existence of the large amplitude plasma wave. At this early time, ponderomotive effects are not that significant, so we argue this is evidence of resonant relativistic self-focusing. In Fig. 33 we plot the contour plot of E_z leaving the right-hand boundary from both simulations at $\omega_p t = 537$. Figure 33a is from simulation II14, while Fig. 33b is from simulation II12. There is clear evidence of self-focusing in Fig. 32b, while in Fig. 32a it is questionable that self-focusing is taking place. (Not all of the laser energy focuses toward the axis in the two frequency, $L_o = 40c/\omega_o$ simulations. This is seen in Fig. 33b where the outer contours are evident.

Since the lasers self-focus sooner under double frequency illumination, the ponderomotive force is larger and the ions are pushed out earlier. This is illustrated in Fig. 34 where the ion phase space plots are presented from both simulations at $\omega_p t = 720$. The phase space plots shown are V_y vs. x and V_y vs. y. In Fig. 34b the ions have already been accelerated to velocities five times the sound speed, while in Fig. 34d the ions are just beginning to be accelerated. A qualitative difference is that the maximum ion velocity is constant along x in Fig. 34c, while it varies in Fig. 34a. This could be due to two differences. First, the lasers self-focus causing the ponderomotive force to increase with position; and second, the plasma wave contributes to the ponderomotive force in the double frequency case. We do not have a model that

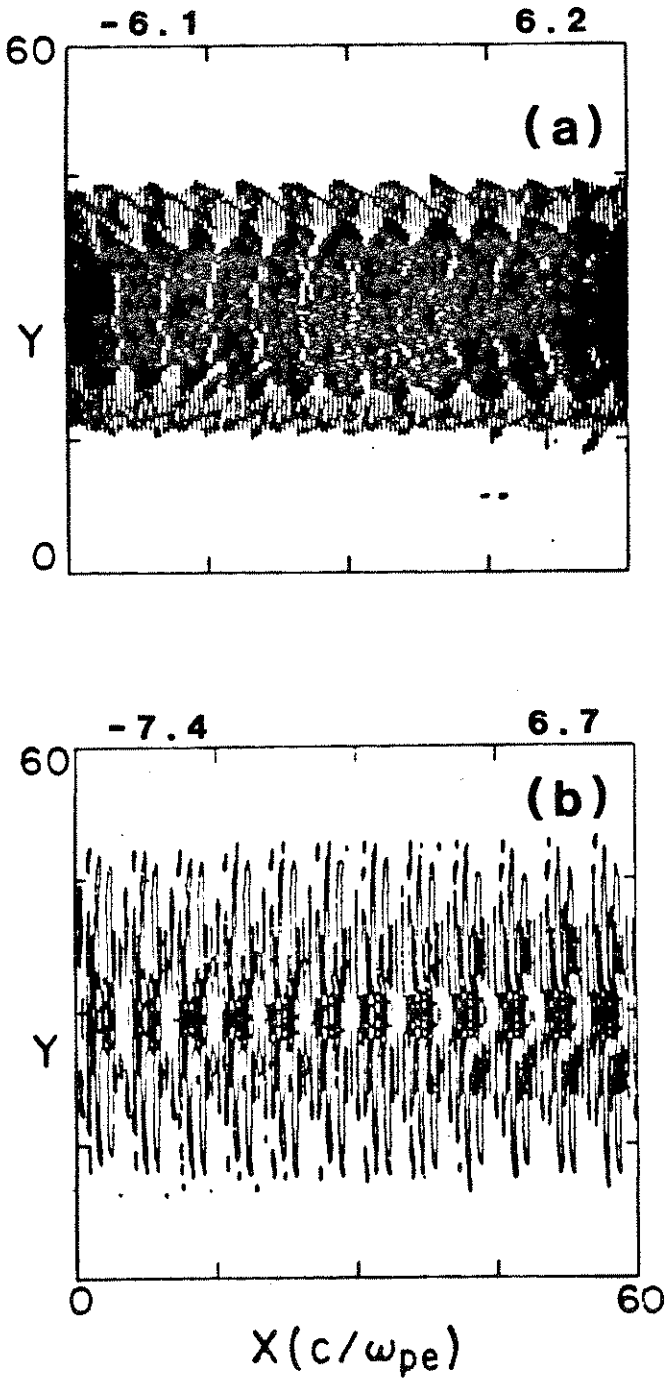

Figure 33. The contour plot of the lasers' field E_z leaving the right-hand boundary with L_o = 40 c/ω_p and τ = 800 for (a) single frequency and (b) double frequency illumination at $\omega_p t$ = 540. The values of the minimum and maximum contours are given.

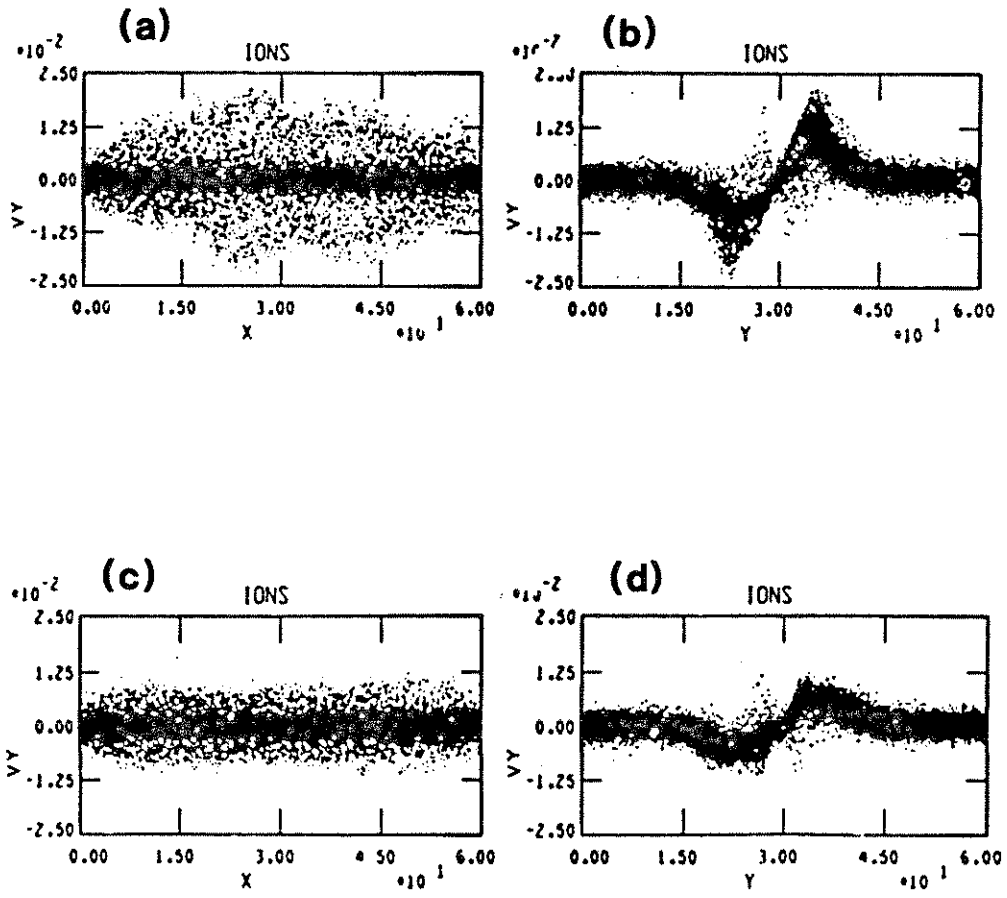

Figure 34. The ion phase space plots (a) V_y vs. x and (b) V_y vs. y for double frequency illumination and (c) V_y vs. x and (d) V_y vs. y for single frequency illumination. The time is $\omega_p t = 720$ with $\tau = 800\omega_p^{-1}$.

quantitatively describes this behavior as yet. In both simulations II12 and II14 filamentation eventually occurs. It occurs first in the double frequency case by roughly $50\omega_p^{-1}$.

Under double frequency illumination, when the lasers' rise time is reduced to $\tau = 150\omega_p^{-1}$ (II16), the properties of the channel depend strongly on relativistic self-focusing. The lasers have relativistically self-focused strongly by $\omega_p t = 200$. This is illustrated in Fig. 35a from the contour plot of E_z leaving the right-hand boundary at $\omega_p t = 237$ presented in Fig. 35a. The spot size is reduced to $\approx 5 \frac{c}{\omega_p}$ and the intensity is amplified by a factor of 2.25. The ions have not acquired much transverse velocity by this time. If all the laser energy was focused to the axis , the "ponderomotive force" would be larger by roughly a factor of 15, since it is proportional to the intensity divided by the spot size. (The 15-fold increase neglects relativistic corrections.) The ions respond more quickly on the right, since the integral of the force is larger. This is illustrated in Fig. 35b where the V_y vs. x and V_y vs. y ion phase space plots are shown at $\omega_p t = 210$. The maximum ion transverse velocity increases approximately linearly in x. In Fig. 35c there are two prominant peaks (one for positive V_y the other for negative V_y). The ions that constitute the peaks are those in the right half of the simulation box.

In this simulation (II16) the ion channel forms first on the right. This is in contrast to simulation II11 where, in spite of relativistic self-focusing, the channel forms on the left first. The qualitative difference between the two simulations exists

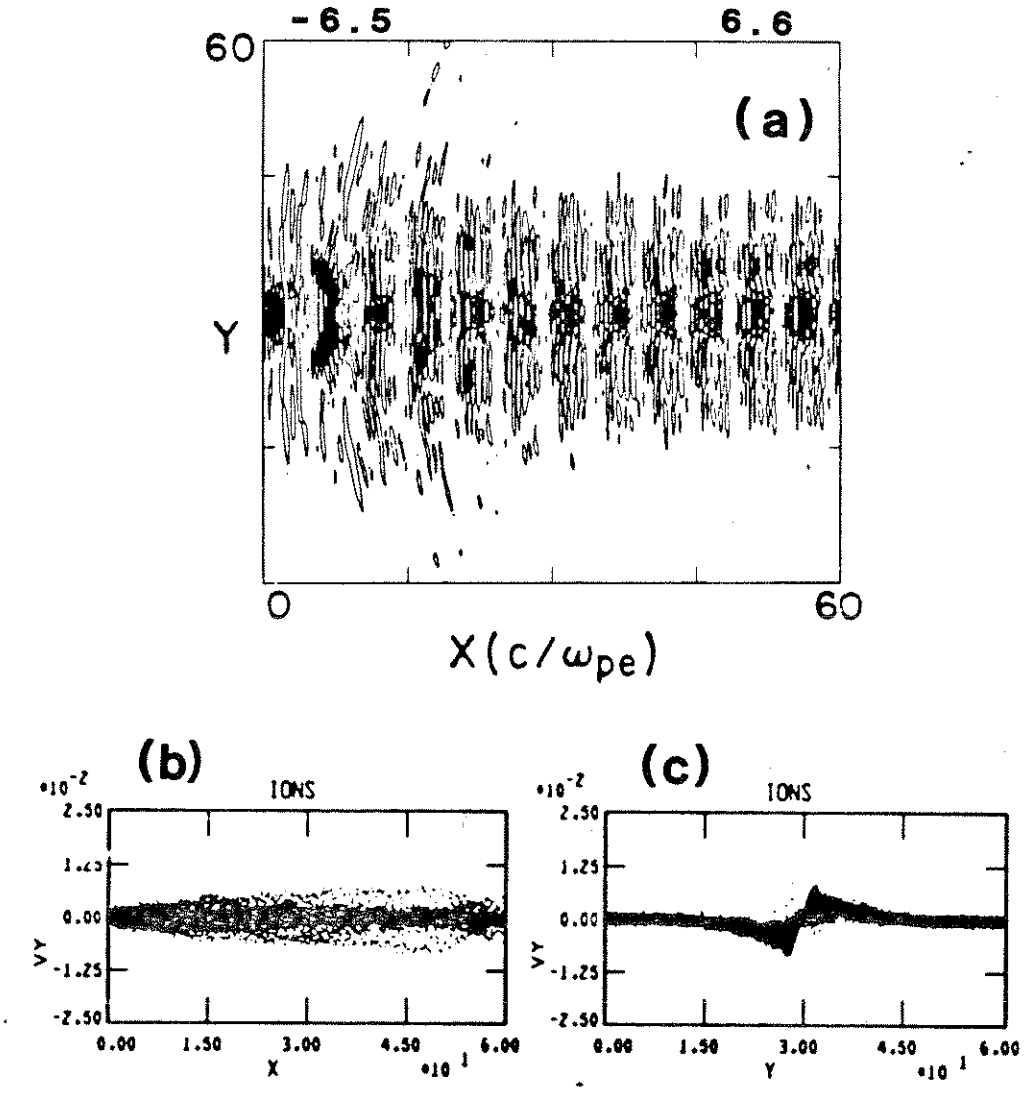

Figure 35. (a) The contour plot of the lasers' field leaving the right-hand boundary E_z at $\omega_p t$ = 237. The (b) V_y vs. x and (c) V_y vs. y ion phase space plots at $\omega_p t$ = 210. The value of L_o = 40 c/ω_p and $\tau = 150\omega_p^{-1}$. The values of the minimum and maximum contours are given.

because the shorter rise time allows the self-focusing to exist over a larger percentage of the simulation duration. In simulation II8, where a narrower initial spot size was used, the channel forms more uniformly along x. This occurred because the ponderomotive force was more uniform along x.

In simulation II16 the lasers' maximum amplification over the length of the box was a factor of 4 in intensity. The beam width collapsed down to $\approx 2 \frac{c}{\omega_p}$. This occurred at $\omega_p t = 537$. All three of the above, including the time, are almost identical to simulation II11 where the rise time was doubled. Late in the simulation at $\omega_p t = 614$ the laser beams start to filament. This is similar to both the other large spot size double-frequency simulations.

The behavior in simulation II15, where single-frequency illumination was used, was qualitatively quite different. Rather than initially self-focusing, the laser beam immediately filaments. This filamentation is first observed at $\omega_p t = 190$. (6 ps for CO_2 laser parameters). The evolution is summarized in Fig. 36. CO_2 parameters were assumed for the labeled times. The ion density on-axis in the left half filaments the light. The cause for the filamentation appears to be quite involved. Similar behavior was observed in simulation II14, and more detail was given in an earlier publication[64]; hence, we only briefly describe the observation here. The incident electromagnetic wave generates a spectrum of plasma waves from RBS and RSS. The plasma waves trap and accelerate electrons generating an anisotropic electron distribution function. The anisotropic distribution function then drives the Weibel

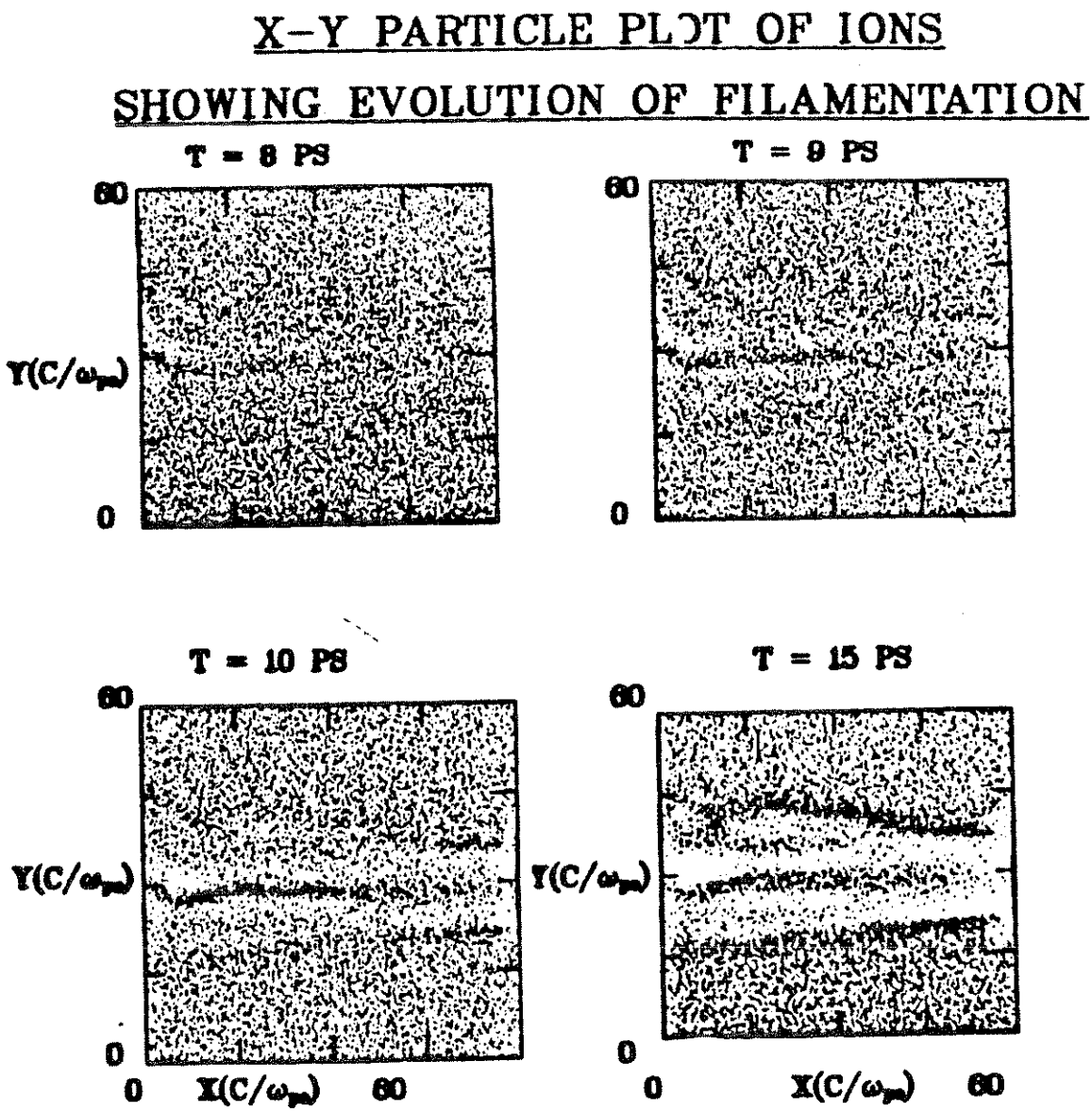

Figure 36. The evolution in time of the ion x-y phase space. The values of T correspond to CO_2 parameters.

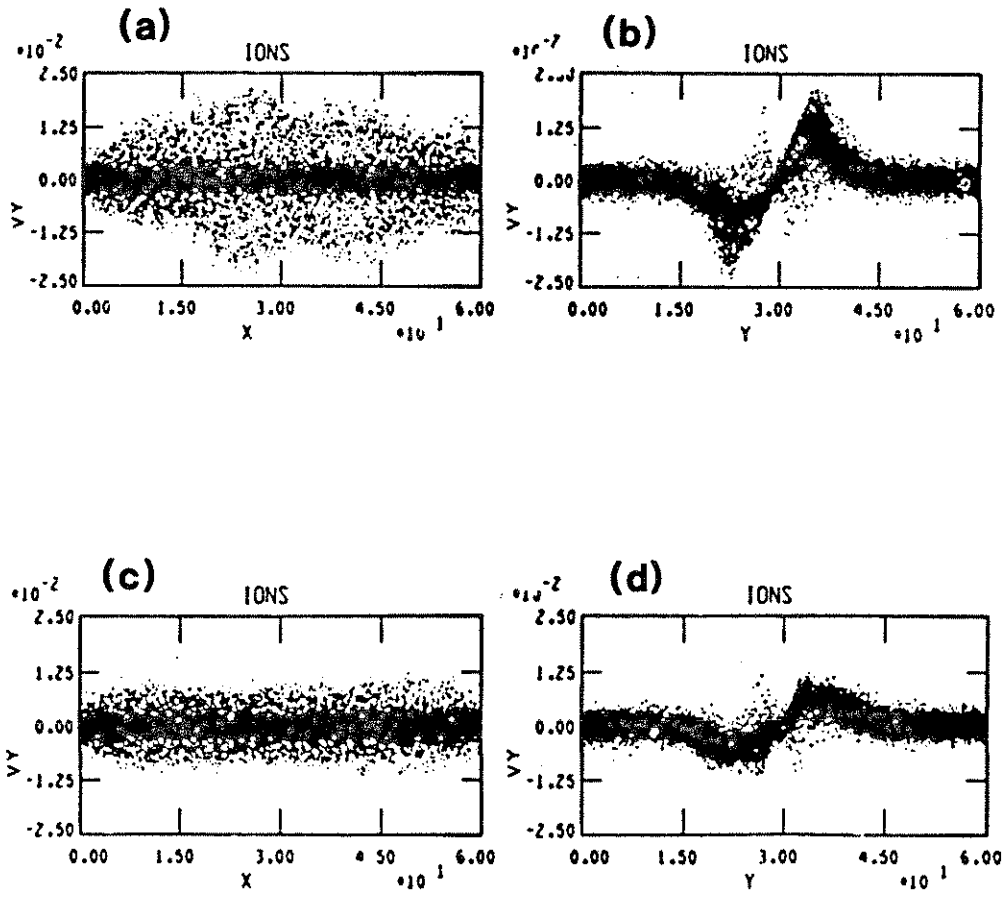

Figure 34. The ion phase space plots (a) V_y vs. x and (b) V_y vs. y for double frequency illumination and (c) V_y vs. x and (d) V_y vs. y for single frequency illumination. The time is $\omega_p t = 720$ with $\tau = 800\omega_p^{-1}$.

quantitatively describes this behavior as yet. In both simulations II12 and II14 filamentation eventually occurs. It occurs first in the double frequency case by roughly $50\omega_p^{-1}$.

Under double frequency illumination, when the lasers' rise time is reduced to $\tau = 150\omega_p^{-1}$ (II16), the properties of the channel depend strongly on relativistic self-focusing. The lasers have relativistically self-focused strongly by $\omega_p t = 200$. This is illustrated in Fig. 35a from the contour plot of E_z leaving the right-hand boundary at $\omega_p t = 237$ presented in Fig. 35a. The spot size is reduced to $\approx 5 \frac{c}{\omega_p}$ and the intensity is amplified by a factor of 2.25. The ions have not acquired much transverse velocity by this time. If all the laser energy was focused to the axis , the "ponderomotive force" would be larger by roughly a factor of 15, since it is proportional to the intensity divided by the spot size. (The 15-fold increase neglects relativistic corrections.) The ions respond more quickly on the right, since the integral of the force is larger. This is illustrated in Fig. 35b where the V_y vs. x and V_y vs. y ion phase space plots are shown at $\omega_p t = 210$. The maximum ion transverse velocity increases approximately linearly in x. In Fig. 35c there are two prominant peaks (one for positive V_y the other for negative V_y). The ions that constitute the peaks are those in the right half of the simulation box.

In this simulation (II16) the ion channel forms first on the right. This is in contrast to simulation II11 where, in spite of relativistic self-focusing, the channel forms on the left first. The qualitative difference between the two simulations exists

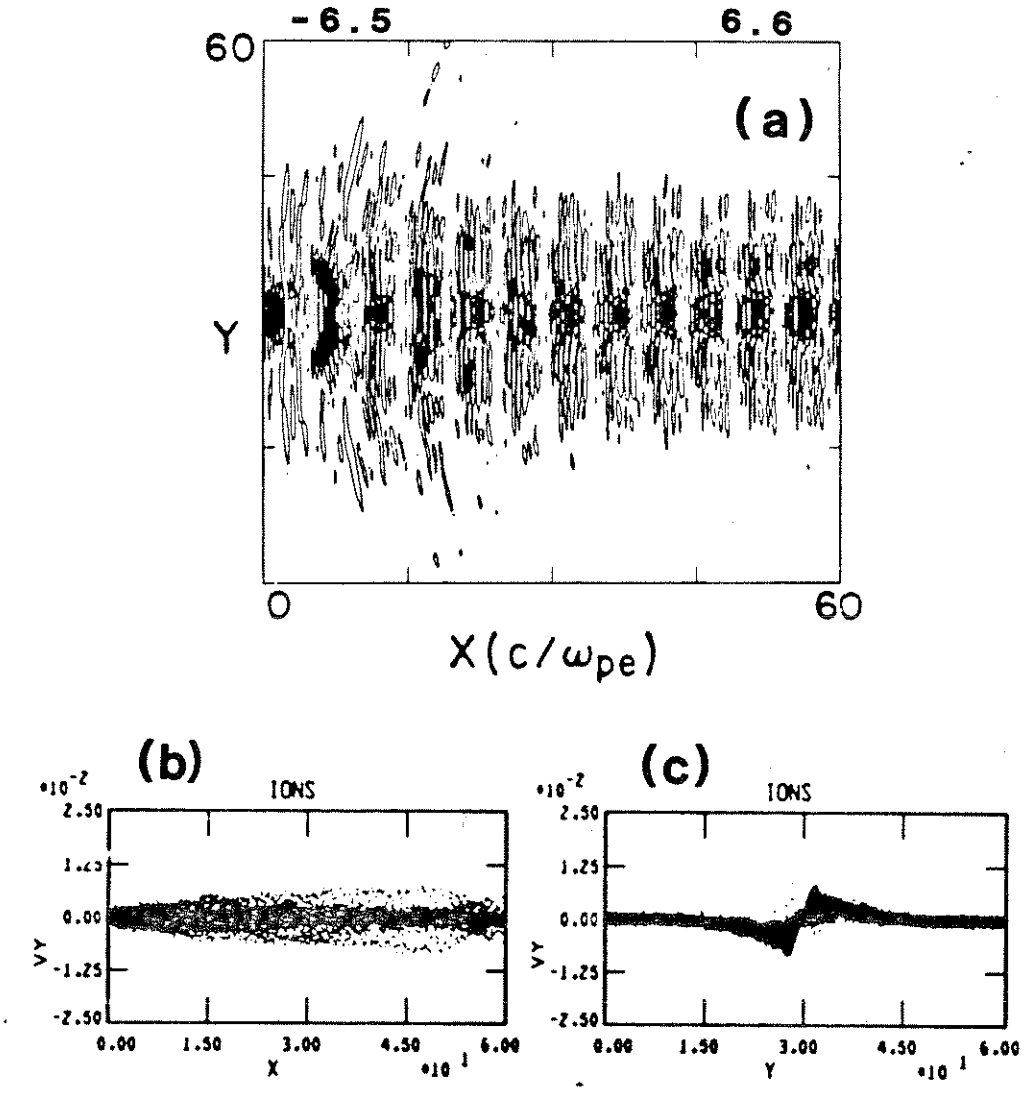

Figure 35. (a) The contour plot of the lasers' field leaving the right-hand boundary E_z at $\omega_p t$ = 237. The (b) V_y vs. x and (c) V_y vs. y ion phase space plots at $\omega_p t$ = 210. The value of L_o = 40 c/ω_p and $\tau = 150\omega_p^{-1}$. The values of the minimum and maximum contours are given.

because the shorter rise time allows the self-focusing to exist over a larger percentage of the simulation duration. In simulation II8, where a narrower initial spot size was used, the channel forms more uniformly along x. This occurred because the ponderomotive force was more uniform along x.

In simulation II16 the lasers' maximum amplification over the length of the box was a factor of 4 in intensity. The beam width collapsed down to $\approx 2 \frac{c}{\omega_p}$. This occurred at $\omega_p t = 537$. All three of the above, including the time, are almost identical to simulation II11 where the rise time was doubled. Late in the simulation at $\omega_p t = 614$ the laser beams start to filament. This is similar to both the other large spot size double-frequency simulations.

The behavior in simulation II15, where single-frequency illumination was used, was qualitatively quite different. Rather than initially self-focusing, the laser beam immediately filaments. This filamentation is first observed at $\omega_p t = 190$. (6 ps for CO_2 laser parameters). The evolution is summarized in Fig. 36. CO_2 parameters were assumed for the labeled times. The ion density on-axis in the left half filaments the light. The cause for the filamentation appears to be quite involved. Similar behavior was observed in simulation II14, and more detail was given in an earlier publication[64]; hence, we only briefly describe the observation here. The incident electromagnetic wave generates a spectrum of plasma waves from RBS and RSS. The plasma waves trap and accelerate electrons generating an anisotropic electron distribution function. The anisotropic distribution function then drives the Weibel

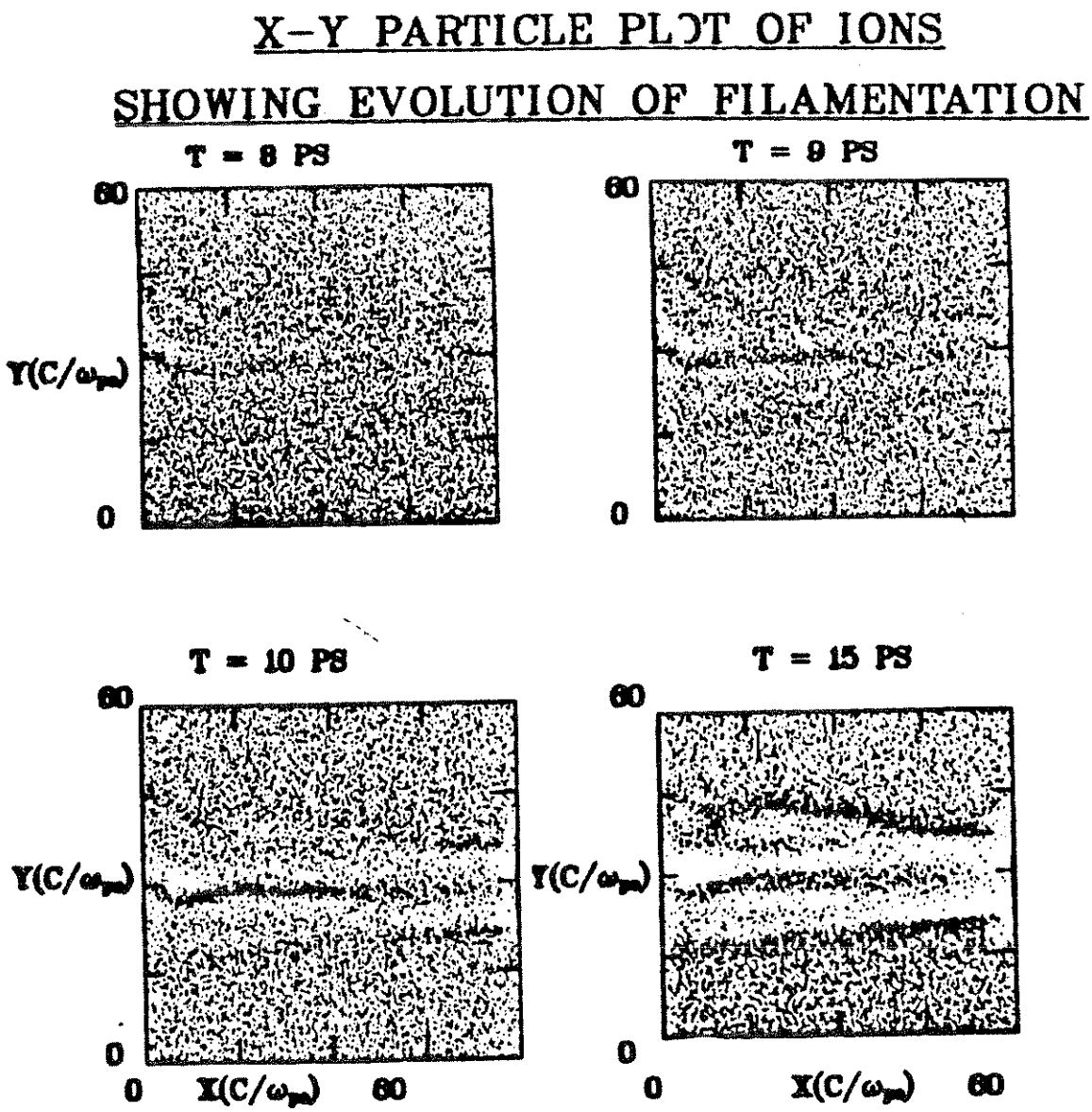

Figure 36. The evolution in time of the ion x-y phase space. The values of T correspond to CO_2 parameters.

instability causing the accelerating electrons to filament. The current filaments give rise to electron density striations. The space charge field then forces the ions to follow. The density striations then cause the lasers to filament. This description is by no means conclusive as it involves many inferences. However, it hopefully points out the richness of the plasma physics that occurs when a high intensity light impinges on an unmagnetized plasma. The amount of reflection from RBS in this simulation was .4 percent. This is larger than in simulation II14 because of the lower initial electron temperature.

VB3. Long Time Evolution

The simulations model a certain section of plasma with the laser pulse moving through it. On the other hand, what is of interest for the PBWA is the evolution of the laser pulse as it moves into fresh plasma. In order to obtain a better idea of the self-focusing behavior of the laser beams for longer propagation distances, simulation II9 was done. Simulation parameters were identical to II8 except for the system size, which was doubled in x and halved in y.

The results are summarized in Fig. 37 where the contour plot of the lasers' magnetic field B_y is shown at $\omega_p t = 390$ and $\omega_p t = 600$. At $\omega_p t = 390$, the laser is at full intensity across almost the entire box since $\tau = 300\omega_p^{-1}$ and $L_x = 120\ \frac{c}{\omega_p}$. In Fig. 37a the effect of relativistic self-focusing is evident. The laser collapses to its narrowest point at $x = 30\ \frac{c}{\omega_p}$ and then remains at a reasonably

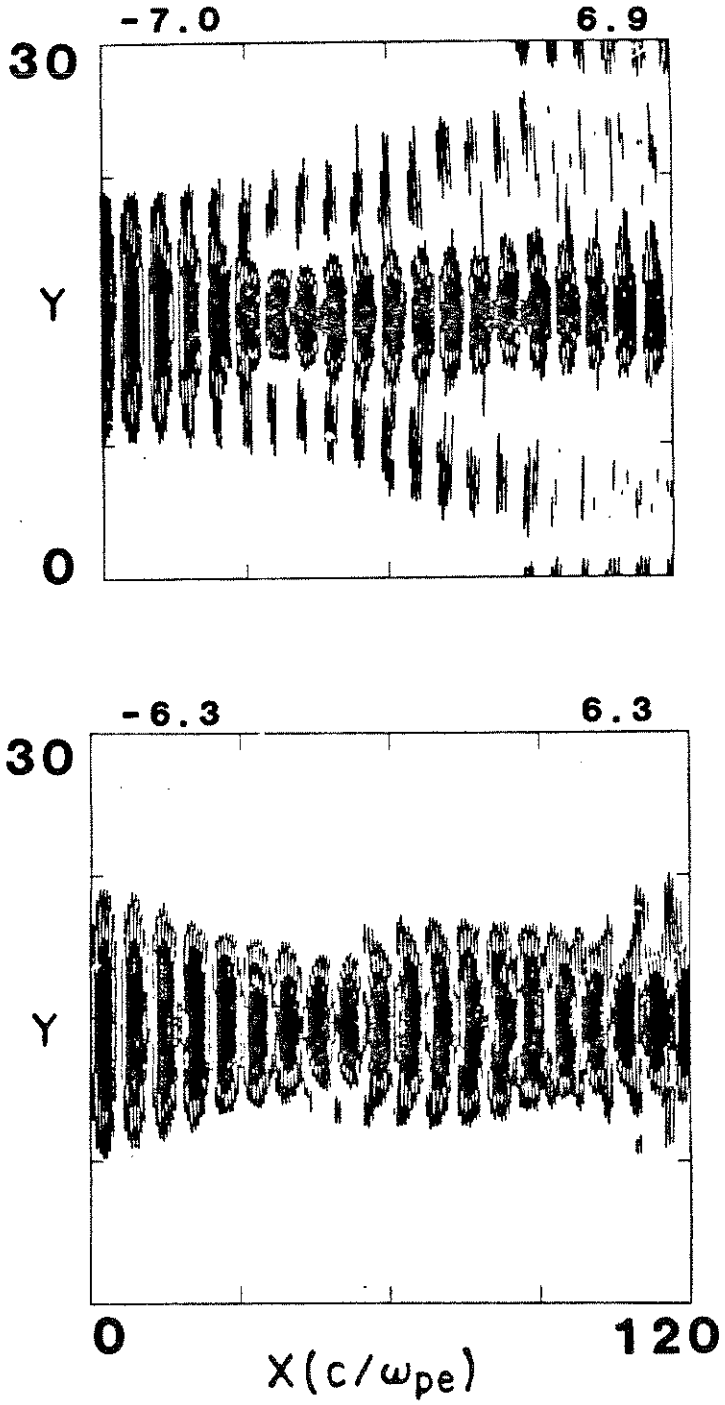

Figure 37. The contour plot of the lasers' field E_z at (a) $\omega_p t$ = 420 and (b) $\omega_p t$ = 600 for $\tau = 300\omega_p^{-1}$ and $L_o = 20\ c/\omega_p$. The values of the minimum and maximum contours are given.

constant diameter of $\approx 5 \frac{c}{\omega_p}$ in the second half of the box. The left half of Fig. 37a is essentially identical to Fig. 30 taken from simulation II8. Even by this time an ion channel has formed, especially on the left. However, the laser profile is determined primarily by relativistic self-focusing. From this simulation it appears that the leading edge of the laser pulse collapses down to a rather constant radius in the absence of ion inertia for distances larger than the acceleration ($2\pi\gamma\phi^2\ c/\omega_p$) distance. Sprangle and Tang[61] have recently investigated under what conditions the beam radius oscillates, remains constant, or blows up.

The effect of the channel formation is seen in Fig. 37b. The point at where the laser beam first converges has moved slightly to the right. As time progresses further, this point continues to move to the right. The laser beam then begins to expand before it is focused again. Furthermore, the laser beam has expanded everywhere along x. This occurs when the ions are expelled, since the laser beam fills the entire channel. As the laser beam continues to expand, the ponderomotive force pushes the channel wall out further. The ions, having acquired significant velocities, would continue to move outward anyway. Steady state is, therefore, not readily attainable in these high intensity simulations where the relativistic self-focusing occurs first.

As the laser continues to move into fixed plasma (ignoring energy loss to the plasma wave), the ions will be expelled more quickly since the ponderomotive force gets larger. As discussed earlier, this increase in the ponderomotive force can be substan-

tial. In some cases, with enough laser power the eventual ponderomotive force could expel the ions on time scales less than an ion plasma period.

An interesting possibility is that the laser pulse could lose energy to the plasma wave at such a rate that relativistic self-focusing would keep the intensity on-axis constant. In this way the ponderomotive force of the focused beam would not be quite as large and the channel would take longer to form.

We summarize by stating that this simulation with a larger L_x indicates a laser beam may relativistically self-focus to a beam radius on the order of a few $\frac{c}{\omega_p}$ for "long" distances. We do not want to make any unwarranted conclusions based on only one simulation. However, due to computer cost constraints this is all that is available to date.

VC. Ion Instabilities

Earlier in Sec. IIIB6 we described results that indicated that the discreteness of the ion background is important. We also demonstrated that a single large-amplitude ion ripple (which requires ion dynamics to form) can lead to mode-coupling that disrupts the BWE process. In this section we illustrate via kinetic simulations how ion inertia is deleterious to BWE in 1-D.

Ion inertia gives rise to several competing instabilities. In Chapter IV we identified SBS of the light wave and parametric decay of the plasma wave as the most important 1-D ion instabilities. Although both instabilities occur in most simulations, their

effects are easily separable. We therefore discuss them separately.

VC1. SBS

We begin by describing simulation II16 since it is very illustrative. The other simulations are presented in the context of how they differ with simulation II16. The relevant parameters of II16 are

$$\frac{v_{os}}{c} = .1,\ \omega_{1,2} = 5,4,\ a_e = .03,\ \frac{M_i}{m_e} = 1836,\ \frac{T_i}{T_e} = 0,\ L_x = 100\frac{c}{\omega_p},$$

and $\tau = 50\omega_p^{-1}$.

SBS is therefore in the highly coupled regime, and the convective growth for the low-frequency pump is $.02\ \omega_p$. The instability is already evident at $\omega_p t = 315$ in the ion density spectrum, $|n_i(k)|^2$, plot shown in Fig. 38a. (By this time there has been six e-foldings of growth.) The largest modes are $2k_2$, where k_2 is the wavenumber of the low-frequency pump, and $2(2k_2 - k_1)$, where k_1 is the wavenumber of the high-frequency pump. The mode at $2(2k_1 - k_2)$ corresponds to SBS of the first low-frequency cascaded mode. Although at this time the ion wave is large with $\frac{\delta n}{n} \simeq .1$ the amount of integrated scattered power is low, ~.1 to 1 percent. The large ion wave allows the BWE wave to mode couple to shorter wavelength modes. This is seen in the hashy appearance of the plasma wave depicted in Fig. 38b. In Sec. IIIB5 this behavior was already

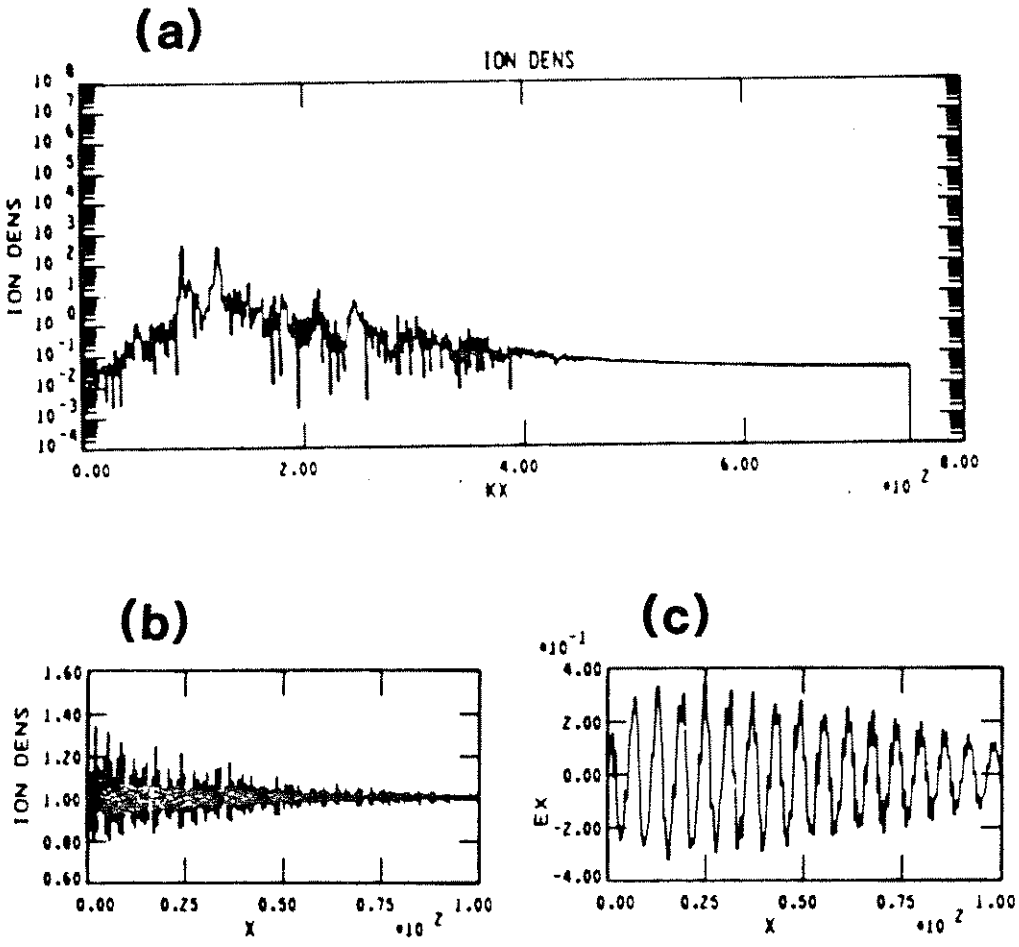

Figure 38. (a) The ion density spectrum, (b) the ion density n_i vs. x and (c) the longitudinal field E_x vs. x at $\omega_p t$ = 315. Relevant parameters are M_i/m_e = 1836 and T_i/T_e = 0.

described for a pre- existing ion ripple. Later in time the scattering is predominantly from the low-frequency cascaded mode. The scattered power eventually becomes as high as 10 percent of the incident power.

The mode coupling in the plasma wave k space is not entirely the result of the SBS ion wave. This is strikingly demonstrated in Fig. 39a where with fixed ions the high k modes are evident in the $\frac{E_x^2}{8\pi}(k)$ plot. This is very similar to the identical type of plot from the mobile ion simulation. In the mobile ion case there are more peaks and they are slightly larger. The coupling results from RBS. The electron temperature is low enough that $2k_o\lambda_d << 1$ so it has a higher growth rate than SBS and thus occurs first. RBS is not in the Compton regime. (In some experimental situations SBS occurs first because it has a lower threshold.) However, from monitoring the reflected light we observe RBS to occur in a short burst, heat the electrons, and shut off. When mobile ions are used, the amount of reflected light continues to increase; while with fixed ions, the reflected light ceases since SBS begins to occur momentarily. In the fixed ion case the short wavelength fluctuations in the E_x vs. x plots are reduced toward the left-hand boundary; while in the mobile ion case, they continue. This is shown in Fig. 39b where E_x vs. x is plotted at $\omega_p t = 315$ from simulation I15. When compared to Fig. 38c, the reduction of the hash is noticeable. The ion wave is shown in Fig. 38b. The ion wave is clearly largest toward the left, and since SRS is no longer occurring there, SBS is the sole reason that E_x is not smooth on the left-hand boundary in Fig. 38c.

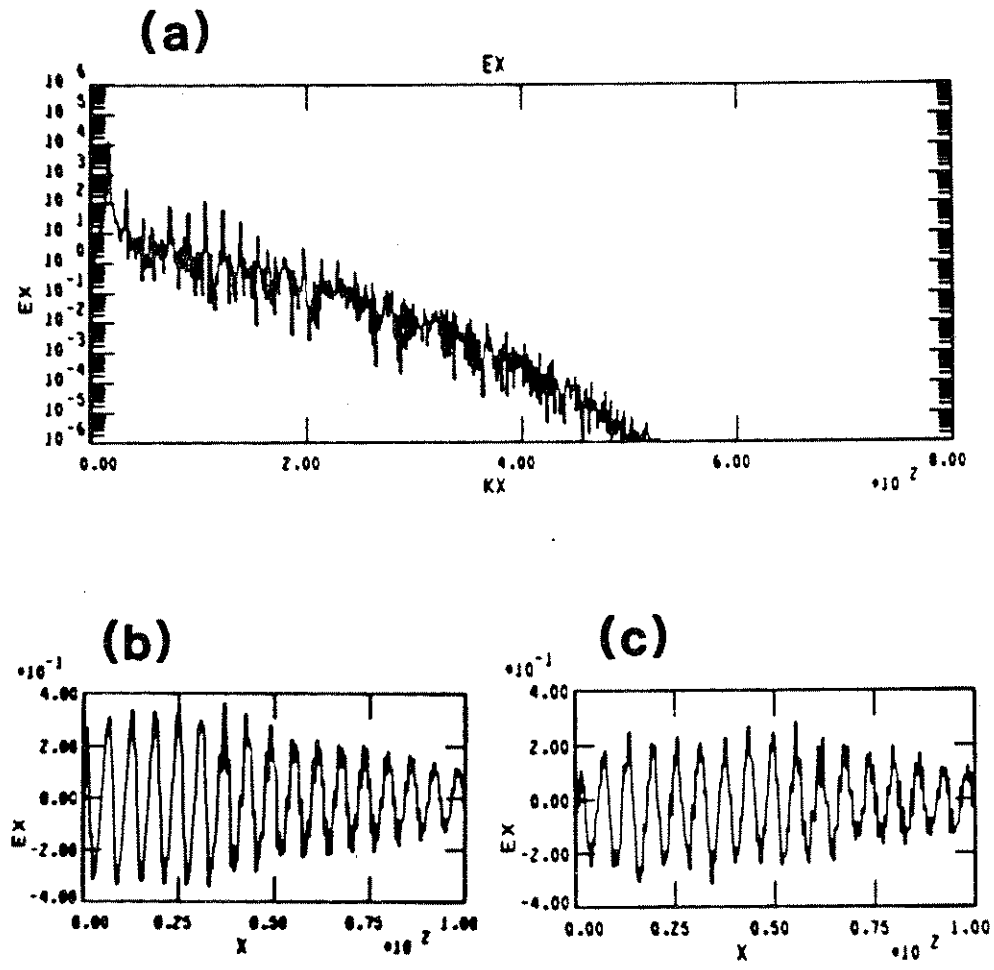

Figure 39. (a) The longitudinal field energy spectrum $E_x^2/8\pi(k)$, (b) the longitudinal field E_x vs. x at $\omega_p t$ = 315. Relevant parameters are $M_i/m_e = \infty$. (c) The longitudinal field E_x vs. x at $\omega_p t$ = 315 for M_i/m_e = 400.

The growth rate for SBS scales as the mass ratio to the -1/3 power. A smaller mass ratio provides a larger growth rate. In simulation I17 the mass ratio is reduced to 400, giving a growth rate $\simeq .03$, which is 1.5 times larger than before. In this simulation the amount of RBS decreases, while the amount of SBS increases. The electric field E_x vs. x is given in Fig. 39c at $\omega_p t = 315$. The plasma wave is smaller in amplitude on the left than before in Fig. 38c. This could be the result of the large ion fluctuations (smaller mass ratio) providing an effective damping.

When the temperature ratio $\frac{T_i}{T_e}$ is ≥ 1, the ion wave is heavily Landau damped. In simulation I19 the ratio was set equal to unity to see whether SBS could be suppressed. The laser intensity is in the strongly coupled regime. This simulation can be summarized in Fig. 40 where the k spectrum of the ion density, $|n_i(k)|^2$ vs. x, is plotted at $\omega_p t = 405$ and 495. At the earlier time there is some evidence of SBS (peaks at $2k_i$ of the light), but it is significantly reduced from simulation I16 where the temperature ratio was zero. The peaks at $2k_o$ arise from the decay of the plasma, and this is discussed shortly. It is also worthwhile to note that while SBS was reduced, SRS was more prelavent later in time. RBS occurred as before in a short burst (although this was reduced), but whereas before SBS subsequently occurred, in this simulation RBS recurs. It would appear that SBS shuts off SRS. The interplay between SRS and SBS is currently under intensive investigation in the laser fusion community and the interested reader should consult those references.[59]

In simulation I18 there are two changes from simulation I16, the meaningful one being the reduction in the laser power. In this simulation both SRS and SBS occur as before. The interesting point is that now the dominant SBS mode is that corresponding to the low-frequency pump rather than the first low-frequency cascaded pump. The reason for this is simply that, for this system size, the amplitude of the plasma wave for the cascaded mode is not large enough to scatter.

In simulation I23 the pump was lowered even further. The electron temperature was increased but this should not be a significant factor. The instability is still in the strongly coupled regime with a growth rate .008 ω_p. No significant SBS is observed during the simulation. This length of the run was 450 ω_p^{-1} so the maximum number of e-foldings was 3.6. The plasma wave grows in the expected fashion. In this simulation initially the ion temperature was zero. The ion fluctuations were, consequently, very small. During the course of the simulation, as the ions thermalize the fluctuation level increased. The plasma wave is never very smooth and background fluctuations may be the reason.

The scenario observed in simulation I22 is quite different from the above description. Due to the initial finite temperature (T_i/T_e= .05) the fluctuation level of the ion density is significant to initially impede the plasma wave growth. This was discussed in Sec. IIIB6. Furthermore, the reduction in the mass ratio means that the growth rate is larger than in I23, .016 ω_p, even though SBS is now in the weakly coupled regime. Once the ion wave

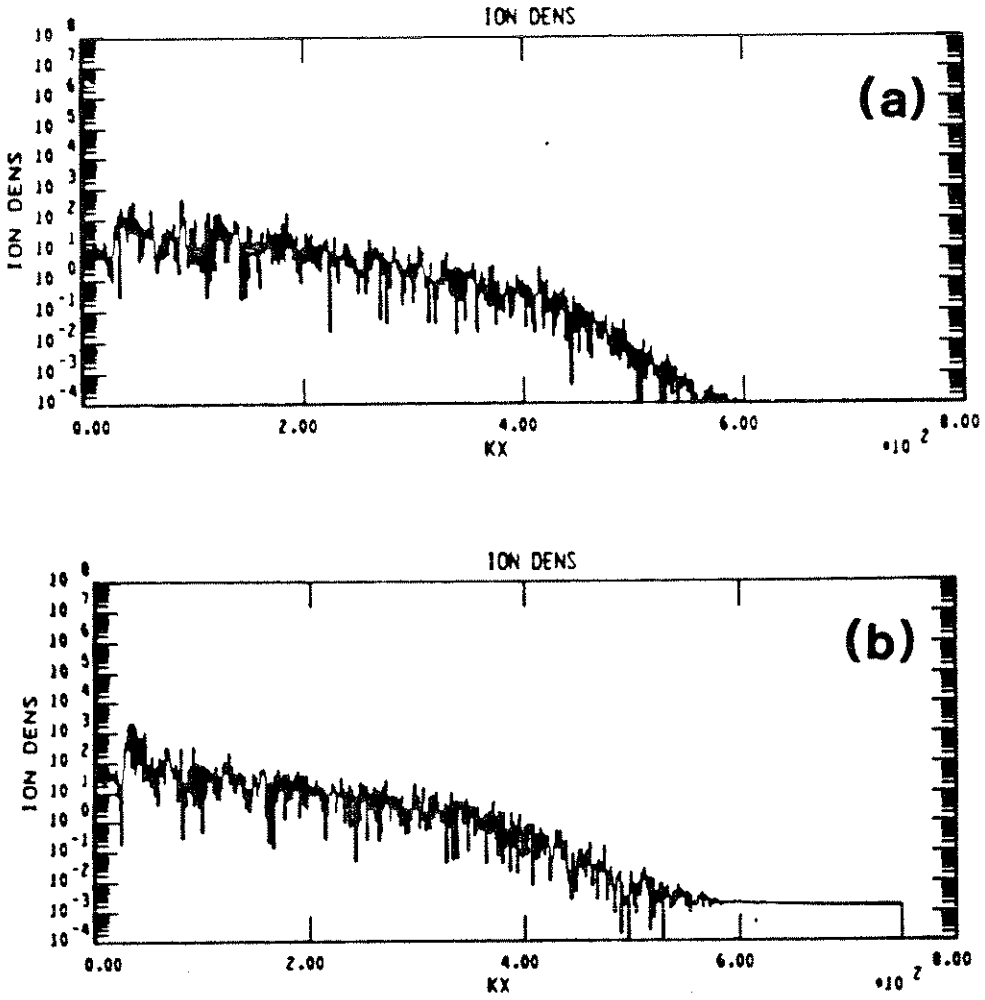

Figure 40. The ion density spectrum at (a) $\omega_p t$ = 405 and (b) $\omega_p t$ = 495 for T_i/T_e = 1.

grows the plasma wave growth ceases. No resemblance of a BWE plasma wave is evident. Furthermore, the amount of reflected power approaches 25-50 percent of the incident power. Most of the reflected power is in $\omega = 4\omega_p$ mode. If this much power is reflected, then the amount available to drive the plasma wave is profoundly reduced.

In simulation I21 the temperature ratio was increased to $T_i/T_e = .2$. This reduced the amount of SBS in the earlier times. Whereas in simulation I22 the amount of scattered power was ~40 percent at $\omega_p t = 614$ and 25 percent at $\omega_p t = 921$, in simulation I21 the fractions are ~50 percent at $\omega_p t = 64$ and 25 percent at $\omega_p t = 921$. This difference was not a factor in the BWE process since a discernible BWE wave was not excited in either case.

In the 2-D simulations SBS was not a factor for several reasons. First, the temperature ratio was unity and second $2k_o\lambda_d$ was ~.7. The temperature ratio was set to unity intentially in order to avoid SBS. We point out that in general wave-particle interactions heat electrons before the ions. This will lower the temperature ratio but it will also increase $2k_o\lambda_d$. In addition, the plasma wave is excited very quickly when the pump strength is so large. The growth rate for strongly coupled SBS scales as $\left(\frac{v_o^2}{c^2}\right)^{1/3}$ while the resonant growth for a BWE scales as $\frac{v_o^2}{c^2}$.

To obtain a handy formula to determine the importance of SBS, we multiply the strongly coupled growth rate by the BWE growth time to obtain the number of e-foldings in a BWE growth period. This gives

$$\text{No. of e-foldings} \simeq 4.8\left(\frac{m}{M}\right)^{1/3}\left(\frac{\omega_1}{\omega_p}\right)^{1/3}\alpha_1^{-1/3}$$

This predicts only a few e-foldings of growth for the 2-D simulations. In eventual experiments $\frac{\omega_p}{\omega_1}$ will be smaller but the number of e- foldings given by the above formula will be only slightly increased because of the 1/3 power.

In sum, we have found no real surprises. SBS can, as expected, reflect a significant percentage of the incoming light. For SBS to be important the pulse needs to be at least a few temporal growth times in duration. The lower frequency pump and the lower frequency cascaded waves (if they become intense enough) are the waves that Brillouin scatter. By increasing the temperature ratio the instability is significantly reduced or suppressed. Mode coupling is observed, although it is complicated by simultaneous occurrences of SRS.

VC2. Parametric Decay

The previous section addressed SBS, an instability of light waves based on ion inertia. In this section we investigate strongly coupled parametric decay on an ion inertia based instability of the plasma wave. We find that it is the most salient instability of the plasma wave.

It was earlier argued that the plasma wave is relativistically modulational unstable owing to the negative relativistic nonlinear frequency shift. It was subsequently argued, based on their linear

growth rates, that strongly coupled parameteric decay is typically dominant. To confirm this, we compare the plasma wave evolution from simulation I15 to that of simulation I16. In Fig. 41 we plot the E_x vs. x at $\omega_p t$ = 495 from both simulations. Recall that in the SBS section we gave the same plots at $\omega_p t$ = 315 to demonstrate mode coupling. For the fixed ion case, the plasma wave is rather coherent in appearance. In contrast, with mobile ions the wave is incoherent and unacceptable for use in a particle accelerator. Although not shown, at $\omega_p t$ = 540 the wave is completely incoherent. The reason for the incoherence is discerned in the density spectrum where a large peak at $2k_o$ is evident. This is shown in Fig. 42a. This results from parametric decay in the strongly coupled regime. The growth rate from Eq. (189) is .03 ω_p for $e_o \simeq .2$. Therefore, over the course of the simulation several e-foldings of growth were possible.

Increasing the temperature ratio does not prevent strongly coupled parametric decay from occurring. In simulation I19 the temperature ratio is unity. While SBS was suppressed, parametric decay was not. In fact, it is more prevalent for the higher temperature ratio. This is seen in Figs. 40b, 41b, 41c, and 42a. In the density spectrum $|n_i(k)|^2$, the peak is larger and broader for the $2k_o$ mode in Fig. 40b than in Fig. 42a. Furthermore, the electric field is noticeably more incoherent for the larger temperature ratio as shown in the E_x vs. x plots in Fig. 41c and Fig. 41b. All plots were for $\omega_p t$ = 495. A possible explanation for this observation is that the ion wave from SBS hinders the

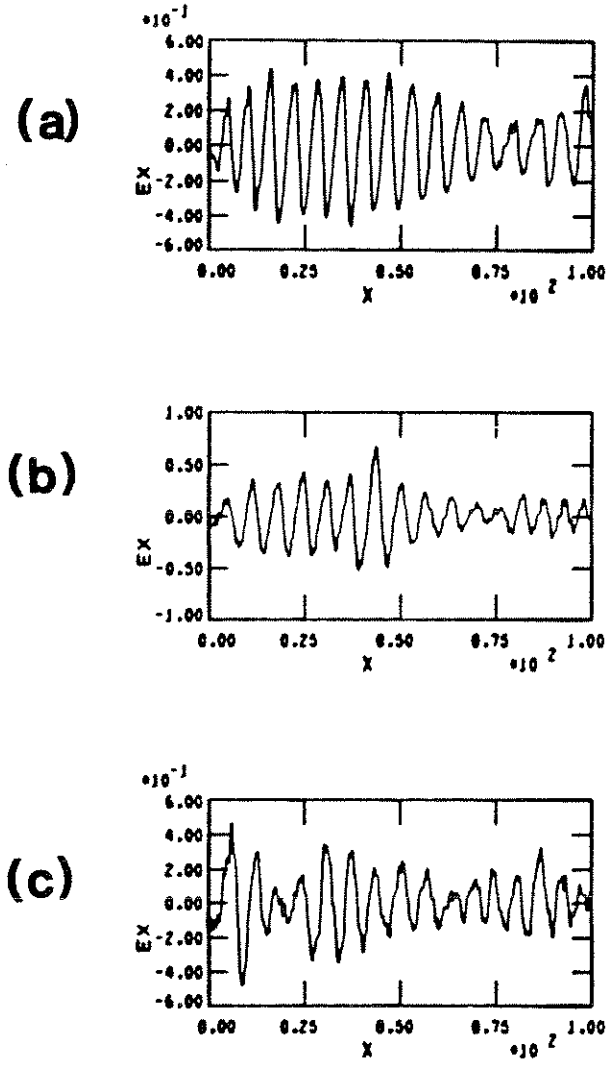

Figure 41. The longitudinal electric field E_x vs. x at $\omega_p t$ = 495 for (a) $M_i/m_e = \infty$, (b) M_i/m_e = 1836, and (c) T_i/T_e = 1.

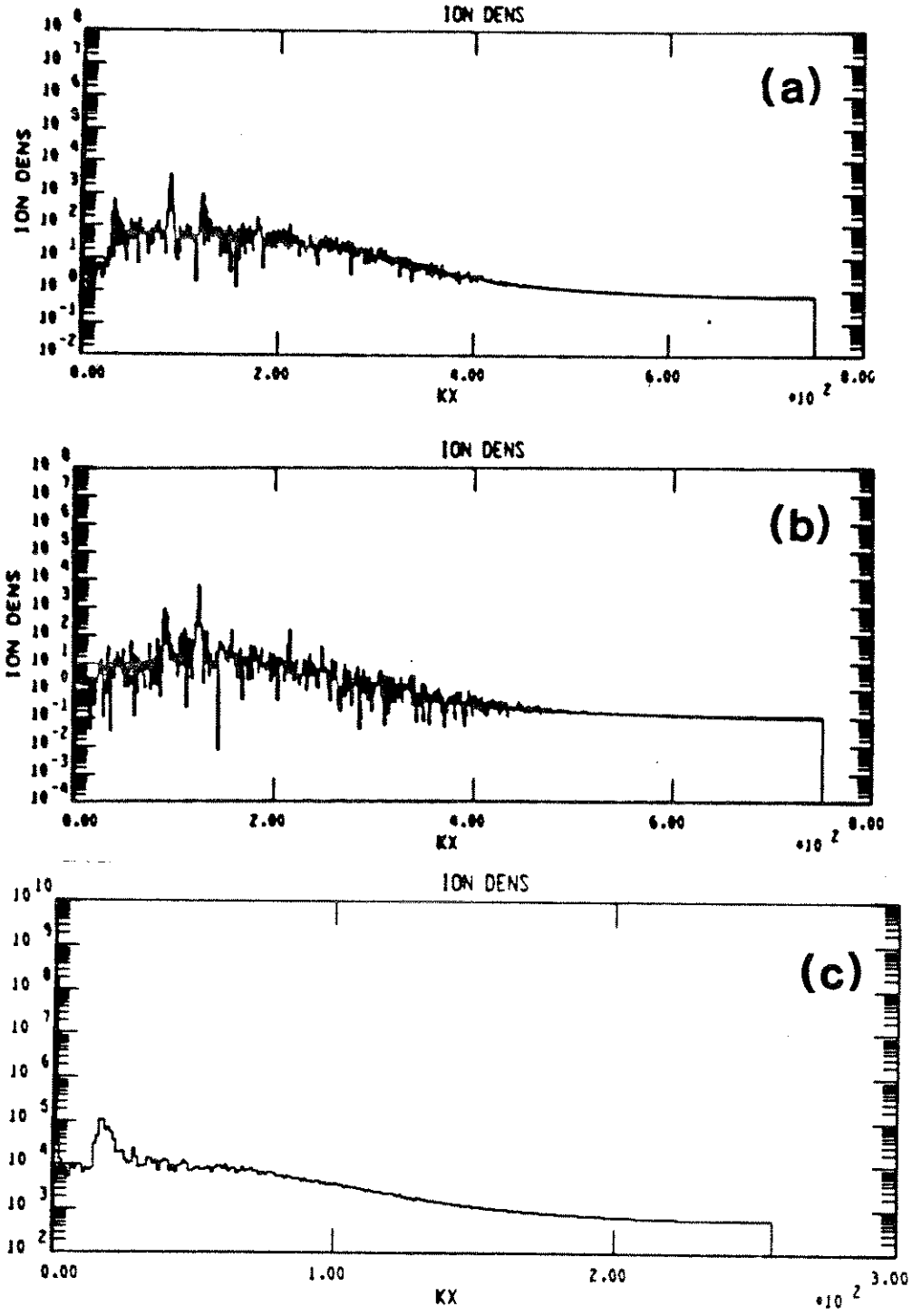

Figure 42. The ion density spectrum from a simulation with (a) $\alpha_1 = \alpha_2 = .1$ and (b) $\alpha_1 = \alpha_2 = .05$ at $\omega_p t = 495$. (c) $\alpha_1 = \alpha_2 = .56$, $L_o = 40c/\omega_p$ and $\tau = 800$ at $\omega_p t = 540$. The mass ratio is 1836 for all three cases.

decay of the plasma wave.

In simulation I18 the pump strength was lowered from $\alpha_1 = .1$ to $\alpha_1 = .05$. The plasma wave amplitude is therefore reduced. The growth rate of strongly coupled parametric decay is lower, so consequently it occurs later in time. This is shown in Fig. 42 where the density spectrum $|n_i(k)|^2$ is plotted from both I16 and I18 at $\omega_p t = 495$. The mode at $2k_o$ is 10 times smaller for the smaller wave amplitude. The plasma wave is nevertheless equally as unacceptable for a high energy accelerator. The number of e-foldings of instability growth can be obtained by integrating the growth rate over the BWE growth time. If the rise time of the lasers is neglected, we find

$$\text{No. of e-foldings} \equiv n = 4.2\left(\frac{m}{M}\right)^{1/3}\alpha_1^{-8/9}.$$

The value of n scales $\alpha_1^{-8/9}$. This means that for larger pump strengths the plasma wave is excited so fast that less decay is observed even though the plasma wave is larger.

The plasma wave is never large or coherent enough to undergo parametric decay in simulations I21 and I22. The background noise and SBS were, by themselves, enough to prevent plasma wave growth. On the other hand, in simulation I23 a plasma wave was excited due to the lower noise level. However, over the length of the run it did not get large enough to go unstable. At $\omega_p t = 450$, the end of the run, a peak at $2k_o$ was barely discernable in the ion density spectrum.

In the 2-D simulations strongly coupled parametric decay was also seen. In the high intensity simulations where $\frac{v_{os}}{c} = .56$ it was not a problem in the short rise time simulations. It did occur later in time, but this was after a Rosenbluth and Liu cycles of growth and decay. The plasma wave saturated before parametric decay occurred. Eventually instabilities of the laser beam occur and wave-particle interactions disrupt the recurring excitation process. In the longer rise time high-intensity simulation II12, the instability was evident. This is shown in Fig. 42c where the ion density spectrum is presented for $\omega_p t = 540$. This is a major reason for the inability to excite as coherent a wave in simulation II12, the long rise time simulation, as that excited in the short rise time simulations.

When the pump is reduced to $\frac{v_o}{c} = .14$, parameteric decay is dramatic. With no SBS occurring, the long wavelength ion wave is clearly evident. This is shown in Fig. 43a and b where the contour plot and a slice plot through $y = 30c/\omega_p$ of the ion density are presented at $\omega_p t = 450$. The density spectrum is similar to that in Fig. 42c. The ion wave approaches $\delta N/N = .5$ in some places. The instability is strongest in the center of the box. The plasma wave amplitude is near $e_o \simeq .3$, so the strongly coupled growth rate is $.6\omega_{pi}$. The plasma wave is correspondingly very incoherent as expected. The instability occurs primarily with the wavefronts of the ion mode parallel to the y axis as seen in Fig. 43a.

The conclusion is, therefore, that strongly-coupled parametric decay is a ubiquitous instability for large-amplitude plasma waves.

(a)

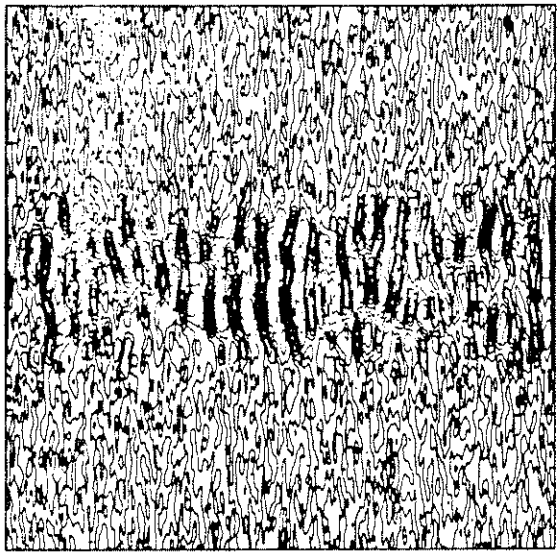

(b)

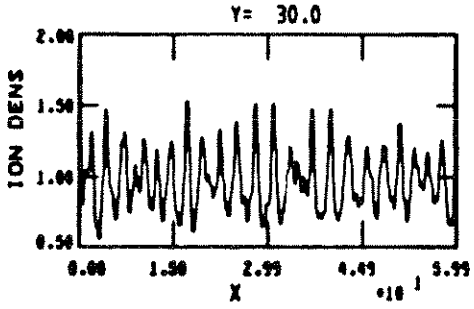

Figure 43. The (a) ion density contour plot and (b) ion density n_i vs. x plot at $\omega_p t$ = 450 for $\alpha_1 = \alpha_2 = .14$ and $\tau = 300\ \omega_p^{-1}$.

It cannot be avoided simply by making $k_i\lambda_d > 1$ or $\frac{T_i}{T_e} > 1$. It would appear the best way to avoid it is to use short intense laser pulses. Fortunately, this requirement on the laser pulse is consistent with the avoidance of the light wave instabilities in the PBWA.

VD. Summary and Conclusions

We have investigated the importance of the various instabilities that compete with the BWE process. The importance of an instability depends on two issues--first whether the instability occurs, and second what effect the instability has on BWE once it arises. Here we summarize the conclusions of this chapter for the most important instabilities.

Self-Focusing

We investigated self-focusing and filamentation of the electromagnetic waves from relativistic effects. The power threshold for self-focusing was found to be consistent with the simulations. Conclusive evidence for relativistic filamentation by itself was not obtained. We observed light to filament when fixed ions were used, but many other processes occurred simultaneously making it difficult to isolate relativistic filamentation.

We showed that when the laser power exceeds the self-focusing threshold the lasers' spot size collapses down to 2-5 c/ω_p in only 60 c/ω_p. The spot size was also observed to remain relatively constant at the final value for at least another 60 c/ω_p.

When the ions move, initially the laser overfocuses, then creates a widening channel void of plasma, and ultimately spreads out. Ponderomotive filamentation is observed at the edge of the channel where a density spike forms and then relaxes. The channel formation time decreases as the laser beam relativistically self-focuses because the ponderomotive force increases, both since E_1 increases and "L_o" decreases.

The simulations provide an indication of the effects of self-focusing. They demonstrate that, as expected, ponderomotive self-focusing is undesirable since the formation of the channel destroys the resonance and hence disrupts the BWE process. Relativistic self-focusing is anticipated to be a positive effect since it would permit propagation distances longer than a Rayleigh length. The simulations indicate that this is true although, since in every case the laser beams entered the plasma with zero divergence, we cannot state this unequivocally. The simulations also point out that a detrimental result of relativistic self-focusing is that it quickens the onset of ponderomotive self-focusing. Pump depletion is still observed in the longer system size simulation; however, the simulation parameters were not optimized. Future work is necessary in order to determine the optimum pulse shape (including transverse), spot size, laser power, and frequency ratio to exploit relativistic self-focusing.

SRS

We found, by multiplying the instability growth rate by the

BWE growth time, that for simulation parameters SRS inevitably should occur. The simulations show that this is indeed the case. For parameters relevant to an accelerator the RBS instability is expected to be in the stimulated Compton regime. The simulations also show that RBS does not lead to significant reflection. The instability occurs and then ceases after the resulting plasma wave breaks and heats the plasma. In the mobile ion simulations RBS does not recur. On the other hand, 4 wave RSS and RFS, as they relate to 1-D and 2-D cascading, need to be investigated further.

In conclusion, RBS is not important because (a) it occurs in a short burst and then does not recur and (b) it is prevented from occurring by making $2\kappa_1\lambda_d > 1$, while 4 wave RSS and RFS need further investigation in the large ω_0/ω_p limit.

SBS

As for SRS, we multiplied the instability growth rate by the BWE growth time to determine whether SBS will occur. Unlike SRS, since its growth rate is lower, it is not always important before a BWE growth time. In the simulations it is found that the linear stability theory is a good guide. The onset of the instability occurs later when the mass ratio is raised or the laser intensity is lowered. The instability is avoided if the temperature ratio is 1.

The resulting ion wave from SBS leads to mode coupling of the BWE plasma wave. We note that the plasma waveform RBS also mode-couples the plasma wave to a spectrum of slower phase velocity

waves. However, the ion wave persists while the plasma wave, as already noted, breaks. Mode coupling from a fixed density ripple was earlier shown in Sec. IIB7 to lead to a lower initial peak plasma wave amplitude. Reflection from SBS was observed to be substantial (50 percent) and this leads to lower overall efficiency. SBS occurs predominantly in the lower frequency light modes. This is also true for RBS.

To summarize, SBS if it occurs is observed to cause mode-coupling and reflect a significant amount of the incident pumps. It is observed to be eliminated by raising the temperature ratio and is believed to be eliminated by making $2\kappa_i\lambda_d \geq 1$. The importance of mode-coupling is that it gives rise to a reduced saturated amplitude. It also creates a spectrum of "slow" plasma waves. Some of these waves couple to RBS. How such a spectrum influences the injected electrons' beam quality needs to be investigated.

Parametric Decay

It was found that, typically, strongly coupled parametric decay was the most important instability, even more important than relativistic self-modulation. In order to determine the importance of parametric decay, we integrated the growth rate over a BWE growth time. Unlike SRS and SBS, there appears to be no way to eliminate this instability for accelerator parameters. Therefore, it is the limiting factor for the number of plasma wavelengths possible for use in an accelerator.

The simulations demonstrate that indeed for relevant parameters the ion-driven instability is significant and more important than the relativistically driven one. The instability creates a spectrum of ion modes centered at $2\kappa_0$. Once the instability onsets the plasma wave appears very incoherent.

We conclude by remarking that the simulations demonstrate that treating each instability separately to determine whether it will not occur gives reasonable results.

Chapter VI. SOME FINAL COMMENTS

This dissertation examined the characteristics of plasma waves driven by collinear optical mixing. The major motivation was to determine the feasibility of using such a plasma wave as the basis for a future high energy accelerator. We conclude that neither the analytical work nor the simulations indicates any fundamental obstacle to the realization of the PBWA concept. The dissertation clarifies the results of recent BWE experiments and identifies those areas where future work should be concentrated.

The results of this work give insight into the recent experiments at Los Alamos,[69] UCLA,[16,40,41,56] and Rutherford.[30] In the Los Alamos experiment a single frequency laser pulse from a CO_2 laser was incident upon a plasma of 5 percent critical density. The experiment failed to generate any fast electrons (the detectors looked at energies above 15 MeV). The results of this experiment can be understood from the following two reasons. First, only a single frequency laser pulse was used so the generation of a plasma wave relied on Raman Forward Scatter. However, the laser-plasma interaction length was too short to allow more than a few e-foldings of the RFS instability (Sec. IVA2b). Second, the laser pulse was too long and too intense resulting in ponderomotive blow-out as described in Sec. VB2. Simulation II13 had very similar parameters to this experiment and it modeled the experiment accurately.

The UCLA experiment exhibited several phenomena illustrated in this dissertation. The saturation amplitude in this experiment is consistent with our theoretical results in Sec. IIB3 on the effects of laser rise time. It is also within experimental uncertainty to the mode-coupling phenomenon discussed in Sec. IIB5. Further evidence of mode coupling was obtained by the UCLA experimentalists who detected the spectrum of secondary electrostatic modes [plasma waves at $(\omega_o, \kappa_o \pm n2\kappa_1)$, and ion waves at $(\omega_{ac}, 2\kappa_1)$]. The secondary modes and mode-coupling were observed in the computer experiments.

The Rutherford group obtained null results. This can be understood from Sec. IIB2a where the effects of phenomenological damping were included. Given the collisional damping and pump strengths in their experiment, a plasma wave below the detection threshold is predicted.

This dissertation does not answer all questions but it helped to identify those areas of BWE where future work is necessary. These include the determination of the efficiency of converting the laser energy into plasma wave energy. An accurate assessment of the efficiency will depend on a clear understanding of cascading, both in one and two dimensions. Previous work on cascading has neglected higher-order couplings such as that between the plasma wave and two light waves separated by $2\omega_p$. Understanding cascading is also necessary in order to determine the phase velocity of the acceleration wave as seen by an injected particle. Another area where future work is required is the determination of

the optimum pulse shape to best utilize the relativistic self-focusing of the lasers.

A complete analysis of the PBWA would also include the topic of beam loading as well as BWE. Beam loading attempts to determine how many and with what beam quality electrons (or other appropiate particles) can be accelerated. We did not address beam loading in this dissertation as it has only recently been examined for the PBWA and other plasma accelerators.[70]

REFERENCES

(1) C. Joshi, IEEE Trans. on Nucl. Sci., NS-32, 1576 (1985)

(2) Maury Tigner, IEEE Trans. on Nucl. Sci., NS-32, 1556 (1985)

(3) A. Loeb and L. Friedland, Phys. Rev. A. 33(3), 1828 (1986)

(4) J. Fontana, Laser Acceleration of Particles (Malibu, 1985), AIP Conference Proc. No. 130, C. Joshi and T. Katsouleas, Ed. (New York, 1985)

(5) C. Joshi et al, Nature (Lond.) 311, 525 (1984).

(6) T. Tajima and J. M. Dawson, Phys. Rev. Lett. 43 267 (1979).

(7) C. Joshi et al., Phys. Rev. Lett. 47,1285 (1981)

(8) M. N . Rosenbluth and C. S. Liu, Phys. Rev. Lett 29, 701 (1972).

(9) C. M. Tang, P. Sprangle, and R. Sudan, Phys. Fluids 28, 1974 (1985)

(10) D.W. Forslund, J.M. Kindel and E.L. Lindman, Phys. Fluids 18, 1002 (1975) and references therein.

(11) D.W. Forslund, J.M. Kindel and E.L. Lindman, Phys. Fluids 18, 1017 (1975) and references therein.

(12) A.B. Langdon, B.F. Lasinski, and W.L. Kruer Phys. Rev. Lett. 43, 133 (1979) and references therein.

(13) Kent Estabrook and W.L. Kruer, Phys. Fluids 26, 1892 (1983)

(14) T. Katsouleas and J.M. Dawson, Phys. Rev. Lett. 51, 392 (1983)

(15) D.W. Forslund et al., Phys. Rev. Lett. 54, 558 (1985)

(16) C. Clayton el al., Phys. Rev. Lett. 55, 1652 (1985)

(17) P. Chen, J. M. Dawson, R. Huff, T. Katsouleas, Phys. Rev. Lett 54, 693 (1985).

(18) Norman M. Kroll, Amiron Ron, and Norman Rostoker, Phys. Rev. Lett. 13, 83 (1964)

(19) B.I. Cohen, A.N. Kaufman, and K.M. Watson, Phys. Rev. Lett. 29, 581 (1972)

(20) B.I. Cohen, Comments on Plasma Physics and Controlled Fusion 8, 197 (1984)

(21) G. Weyl, Phys. Fluids 13, 1802 (1970)

(22) R. J. Noble, Phys. Rev. A 32 460 (1985).

(23) R. Bingham, R. A. Cairns, and R. G. Evans, Report RAL-84-12, Rutherford Appleton Laboratory, 1984.

(24) J. T. Mendonca, J. Plasma Physics 34, 115 (1985).

(25) W.B. Mori, Proceedings of the 1985 CECAM Workshop on Interaction and Transport in Laser-Plasmas (1986)

(26) C. J. McKinstrie and D. W. Forslund, Los Alamos Lab Report LA-VR86-621 (1986) to be published in Phys. Fluids

(27) N. Bogoliubov and Y. A. Mitropolskii, Asymptotic Methods in the Theory of Nonlinear Oscillations, Gordon and Breach Science Publishers, New York (1961).

(28) D. Montgomery and P. Tidman, Phys. Fluids 7, 242 (1964). and F.W. Sluijter and D. Montgomery, Phys. Fluids 7, 242 (1964)

(29) P.S. Lee et al, Phys. Rev. Lett. 30, 538 (1973)

(30) R. Bingham et al., to be published in J. Plasma Physics

(31) C.M. Bender and S.A. Orszag, Advanced Mathematical Methods for Scientists and Engineers, McGraw Hill, New York

(32) Handbook of Mathematical Functions, National Bureau of Standards AMS 55, Ed. Milton Abramowitz and Irene Stegun

(33) L.D.Landau and E.M. Lifshitz, Mechanics, Pergamon Press, New York

(34) Steven W. McDonald et al., Physica 17D, (1985) 125

(35) W.B. Mori, Masters Thesis, UCLA (1984) and W.B. Mori, C. Joshi, and J.M. Dawson, IEEE Trans. on Nucl. Sci. NS-30, 3244 (1983)

(36) D.J. Sullivan and B.B. Godfrey, Laser Acceleration of Particles (Los Alamos, 1982) AIP Conference Proceedings No. 91, P. Channel, Ed. (New York, 1982)

(37) A. I. Akhiezer and R. V. Polovin, Sov. Phys. JETP 3, 696 (1956).

(38) W. Horton and T. Tajima to be published in Phys. Rev. A

(39) S.J. Karttunen and R.R.E. Salomaa, Phys. Rev. Lett. 56, 604 (1986) and S.J. Karttunen and R.R.E. Salomaa, IEEE Trans. on Nucl. Sci. PS-15, 2 (1987), Special Issue on Plasma Based

Accelerators, T. Katsouleas, Ed.

(40) C. Darrow et al., Phys. Rev. Lett. 56, 2629 (1986)

(41) C. Darrow et al., IEEE Trans. Plasma Sci. PS-15, 2 (1987) Special Issue on Plasma Based High Energy Accelerators T. Katsouleas, Ed.

(42) John Dawson and Carl Oberman, Phys. Fluids 5, 518 (1962)

(43) John Dawson and Carl Oberman, Phys. Fluids 6, 394 (1963)

(44) W.L. Kruer, Phys. Fluids 15, 2423 (1972)

(45) P.K. Kaw, A.T. Lin, and J.M. Dawson, Phys. Fluids 14, 1967 (1973)

(46) W. Horton and T. Tajima, Phys. Rev. A 31, 3937 (1985)

(47) R. Bingham, RAL Report RAL-83-058 (1985)

(48) C.E. Max, J. Arons, and A.B. Langdon, Phys. Rev. Lett. 33, 209 (1974)

(49) R. Ruth et al., Particle Accelerators 17, 171 (1985)

(50) R. Fedele, U. de Angeles and T. Katsouleas, Phys. Rev. A 33, 4412 (1986)

(51) W.B. Mori, to be published

(52) C.K. Birdsall and A.B. Langdon, Plasma Physics via Computer Simulation, (McGraw-Hill, New York, 1985).

(53) R.L. Morse and C.W. Nielson, Phys. Fluids 14, 830 (1971)

(54) David W. Forslund, Space Science Reviews 42, 3 (1985)

(55) D.F. Dubois et al., 16th Anomalous Absorption Conference, July 13-18, 1986 (New York)

(56) C. Darrow, Ph.D. Dissertation UCLA

(57) Bruce I. Cohen and Claire Ellen Max, Phys. Fluids 22, 1115 (1979)

(58) J. Nuckolls et al., Nature 239, 139 (1972)

(59) C. Aldrich, B. Bezzerides, D.F. Dubois, H. Rose, Los Alamos Report No. LA-UR 85-2099 (unpublished), and Bulletin of the 16th Anomalous Absorption Conference, July 13-18, 1986, Lake Luzerne, New York.

(60) B.D. Fried et al., Phys. Fluids 19, 1975 (1976)

(61) P. Sprangle and C.M. Tang, IEEE Trans. on Plasma Sci. PS-15, 2 (1987), Special Issue on Plasma Based High Energy Accelerators, T. Katsouleas, Ed.. and P. Sprangle and C.M. Tang, Laser Acceleration of Particles, AIP Conference Proc. No. 130, C. Joshi and T. Katsouleas, Ed., (New York, 1985)

(62) G. Schmidt and W. Horton, Comments on Plasma Physics and Controlled Fusion 9, 85 (1985)

(63) C. Joshi, C.E. Clayton and F.F. Chen, Phys. Rev. Lett. 48, 874 (1982)

(64) P.K. Kaw, G. Schmidt and T. Wilcox, Phys. Fluids 16, 1522 (1973)

(65) W.B. Mori et al., Laser Interactions and Related Plasma Phenomena, H. Hora and G. Miley Eds. (Plenum, New York, 1986) Vol. 7

(66) J. M. Dawson, Phys. Rev. 113, 383 (1959)

(67) P. Sturrock, Proc. Roy. Soc. (London) A242, 277 (1957)

(68) E. A. Jackson, Phys. Fluids 5, 831 (1960)

(69) P. Goldstone, Workshop on Laser Acceleration of Particles, Malibu, 1985.

(70) T. Katsouleas et al., to be published in Particle Accelerators.

APPENDIX A

ON NONLINEAR PLASMA FREQUENCY SHIFTS IN BEAT WAVE EXCITATION

In this appendix we will resolve a controversy that has arisen recently in Beat Wave Excitation. The controversy has arisen over the magnitude and sign of the nonlinear frequency shift. In particular, the discrepancy exists between the use of the Eulerian or Lagrangian fluid description. On the one hand, the works of Rosenbluth and Liu[8]; Tang, Sprangle, and Sudan[9]; and Noble[22] conclude that only relativistic effects contribute to the nonlinear frequency shift; while, on the other hand, Bingham, Cairns, and Evans[23] and Mendonca[24] claim that harmonics contribute an additional frequency shift larger in magnitude and opposite in sign to the relativistic one. With the exception of Noble, the former group used Lagrangian coordinates. Bingham et al. and Mendonca used Eulerian coordinates and both used the continuity equation rather than Ampere's law, which is a stronger condition in one dimension. Therefore, their set of equations possessed an ambiguity which they eliminated by requiring that the second-order fluid velocity vanish. This leads to a plasma drift (a point to be made more explicit later) and a doppler-shifted frequency. This doppler shift is the additional frequency shift. By using Ampere's Law, this drift is eliminated due to the induced electric field. Noble used Eulerian coordinates and obtained only a relativistic shift, but the error of Bingham et al. and Mendonca is not explicitly exposed.

In the past literature many papers are devoted to large-amplitude plasma oscillations. Among the first was the work of Akhiezer and Polovin[37] who studied both transverse and longitudinal oscillations in the Eulerian description. For longitudinal oscillations, they conclude that the only nonlinear frequency shift is negative and due to relativisitc effects (thermal corrections have been neglected throughout). This point, however, is never explicitly mentioned. In 1959, Dawson[66] showed through the Lagrangian description, with the exclusion of relativistic effects, that until wave breaking even large- amplitude oscillations are modeled by a linear differential equation. Consequently, he also found no nonlinear frequency shift. In 1957 Sturrock,[67] using the Eulerian description and a multiple time scale analysis, concluded that there was a positive frequency shift. In 1961, Jackson,[68] bothered by the apparent discrepancy, concluded that Sturrock had erred. Now, 25 years later, a similar controversy has arisen.

In what follows, we explicitly resolve the controversy using the perturbation techniques of Krylov, Bogoliubov, and Mitropolsky[27,28] and the Eulerian description. The starting point is Eq. (13) in the text.

$$\left(\frac{\partial^2}{\partial t^2} + \omega_p^2\right) E_x = \tfrac{3}{2}\,\omega_p^2\,\epsilon^2\,\frac{v_x^2}{c^2}\,E_x + \tfrac{1}{2}\omega_p^2\,\epsilon^2\,\frac{v_z^2}{c^2}\,E_x$$

$$+ \epsilon\,4\pi e\left(\frac{\partial}{\partial t}\,nv_x - \bar{n}_o\,v_x\,\frac{\partial}{\partial x}\,v_x\right.$$

$$\left. + \epsilon\,\frac{\bar{n}_o e}{m}\,\frac{v_x v_z}{c^2}\,E_z - \frac{\bar{n}_o e}{m}\,\frac{(\vec{v}\times\vec{B})}{c}\,x\right) \qquad (A.1)$$

From now on we normalize time to ω_p^{-1}, distance to the collision-skin depth c/ω_p, and current to $e\bar{n}_o c$. We assume that the lasers are polarized in the $\hat{z}$ direction and are propagating in the $\hat{x}$ direction. The parameter ϵ is used to order the fields and for bookkeeping purposes. The product of two laser quantities is of order ϵ. We are solving for E_x, v_x, and n for given v_z's and E_z's; therefore, the indexes will be dropped. We assume E, v, and n are of the form

$$E = e_o \cos \psi_e + \sum_{i=1} \epsilon^i e_i \qquad (A.2)$$

$$v = v_o \sin \psi_v + \sum_{i=1} \epsilon^i v_i \qquad (A.3)$$

$$n = n_o \sin \psi_n + \sum_{i=1} \epsilon^i n_i \qquad (A.4)$$

while E_j is of the form $E_{zj} \sin (\kappa_j x - \omega_j t)$. To complete our set of equations, we use Ampere's Law and Gauss's Law.

$$\frac{\partial E}{\partial t} + j = \frac{\partial E}{\partial t} - Nv = 0 \qquad (A.5)$$

$$\nabla \cdot E = \rho = -n \ . \qquad (A.6)$$

Note that the continuity equation is $\partial/\partial x$ of Eq. (A.5), so Eq. (A.5) is a stronger statement. In addition we assume that

$$\frac{\partial e_o}{\partial t} = \epsilon\ A_1^e(e_o,\phi_e,F) + \epsilon^2\ A_2^e + \ldots \qquad (A.7)$$

$$\frac{\partial e_o}{\partial x} = \epsilon\ D_1^e(e_o,\phi_e,F) + \epsilon^2\ D_2^e + \ldots \qquad (A.8)$$

$$\frac{\partial \psi_e}{\partial t} = -\omega_o + \epsilon\ B_1^e(e_o,\phi_e,F) + \epsilon^2\ B_2^e + \ldots \qquad (A.9)$$

$$\frac{\partial \psi_e}{\partial x} = \kappa_o + \epsilon\ C_1^e(e_o,\phi_e,F) + \epsilon^2\ C_2^e + \ldots \qquad (A.10)$$

where ϕ_e is the phase difference between the electric field and the driving force and F is the amplitude of the driving force. The dependence on F is included for pump rise time considerations. Analogous notation for v and n is employed. The quantities A_1, B_1, C_1, and D_1 are eventually chosen to eliminate secular growth. Equations (A.7) and (A.9) are the standard two-coupled first-order nonlinear differential equations found in Refs. 8 and 9.

Substituting Eqs. (A.2) and (A.7) through (A.10) into the linear operator on the left-hand side of Eq. (A.1) gives

$$\left(\frac{\partial^2}{\partial t^2} + 1\right)\vec{E} = \epsilon^0\ \left(-\omega_o^2\ e_o \cos\psi_e + e_o \cos\psi_e\right)$$

$$+ \epsilon^1\left(2\omega_o\ A_1^e \sin\psi_e + 2e_o\omega_o B_1^e \cos\psi_e + \omega_o^2 \frac{\partial^2 e_1}{\partial \psi_e^2} + \omega_o^2\ e_1\right)$$

$$+ \epsilon^2\left(A_1^e \frac{\partial A_1^e}{\partial e_o} \cos\psi_e + B_1^e \frac{\partial A_1^e}{\partial \phi_e} \cos\psi_e - 2A_1^e\ B_1^e \sin\psi_e\right.$$

$$\left. + 2\omega_o A_2^e \sin\psi_e - e_o A_1^e \frac{\partial B_1^e}{\partial e_o} \sin\psi_e - e_o B_1^e \frac{\partial B_1^e}{\partial \phi_e} \sin\psi_e\right.$$

$$- e_o B_1^{e2} \cos \psi_e + 2\omega_o e_o B_2^e \cos \psi_e - 2\omega_o A_1^e \frac{\partial^2 e_1}{\partial \psi_e \partial e_o}$$

$$- 2\omega_o B_1^e \frac{\partial^2 e_1}{\partial \psi_e^2} + \omega_o^2 \frac{\partial^2 e_2}{\partial \psi_e^2} + \omega_o^2 e_2$$

$$+ \frac{\partial F}{\partial t} \frac{\partial A_1^e}{\partial F} \cos \psi_e - e_o \frac{\partial F}{\partial t} \frac{\partial B_1^e}{\partial F} \sin \psi_e \Big) . \qquad (A.11)$$

We now begin the process of equating the coefficients of the ϵ^i's in Eq. (A.1). Since the right-hand side of Eq. (A.1) has terms of order ϵ or higher, then the coefficient of ϵ^o in Eq. (A.11) must vanish. So

$$-\omega_o^2 e_o \cos \psi_e + e_o \cos \psi_e = O(\epsilon) \cos \psi_e \qquad (A.12)$$

or

$$\omega_o^2 = 1 + O(\epsilon)$$

Next, we need the coefficients of ϵ^2 on the right-hand side of Eq. (A.6). Since it is already multiplied by ϵ, to obtain the ϵ^1 term we use the zero order solutions of n and v, n_o and v_o to obtain

$$\epsilon^1 \left\{ \left[\frac{\partial}{\partial t} n_o v_o - v_o \frac{\partial}{\partial x} v_o - (\vec{v}_z \times \vec{B}_y) \right] \right\} \qquad (A.13)$$

where $\vec{v}_z$ and $\vec{B}_y$ are prescribed. On the other hand, n_o and v_o need to be calculated as functions of e_o from Ampere's Law and Gauss's Law.

From Gauss's Law and Eqs. (A.2), (A.4), and (A.7) through (A-10) we find

$$\varepsilon^0\left(-\kappa_o e_o \sin\psi_e = -4\pi e n_o \sin\psi_n\right)$$

$$+ \varepsilon^1\left(-C_1^e\, e_o \sin\psi_e + D_1^e \cos\psi_e + \kappa_o \frac{\partial e_1}{\partial \psi_e} = -n_1\right)$$

$$+ \varepsilon^2\left(-C_2^e\, e_o \sin\psi_e + D_2^e \cos\psi_e + D_1^e \frac{\partial e_1}{\partial e_o} + C_1^e \frac{\partial e_1}{\partial \psi_e}\right.$$

$$\left. + \kappa_o \frac{\partial e_2}{\partial \psi_e} = n_2\right) + \ldots \qquad \text{(A.14)}$$

The ε^0 term of Eq. (A.13) leads to

$$\kappa_o e_o = n_o \quad \text{and} \quad \psi_e = \psi_n \qquad \text{(A.15)}$$

In addition, from Ampere's Law and Eqs. (A.2) through (A.4), (A.8) through (A.10) we find

$$\varepsilon^0\left(\omega_o e_o \sin\psi_e = v_o \sin\psi_v\right) + \varepsilon^1\left(-B_1^e\, e_o \sin\psi_e + A_1^e \cos\psi_e - \omega_o \frac{\partial e_1}{\partial \psi_e}\right.$$

$$\left. = n_o v_o \sin\psi_v \sin\psi_e + v_1\right) + \varepsilon^2\left(-B_2^e\, e_o \sin\psi_e + A_2^e \cos\psi_e\right.$$

$$\left. + A_1^e \frac{\partial e_1}{\partial e_o} + B_1^e \frac{\partial e_1}{\partial \psi_e} - \omega_o \frac{\partial e_2}{\partial \psi_e}\right.$$

$$\left. = v_2 + n_o v_1 \sin\psi_e + n_1 v_o \sin\psi_v\right) + \ldots \qquad \text{(A.16)}$$

The ϵ^0 term in Eq. (A.15) gives

$$\omega_o e_o \sin \psi_e = v_o \sin \psi_v \tag{A.17}$$

so

$$v_o = \omega_o e_o \qquad \text{and} \qquad \psi_v = \psi_e$$

The fact that $\psi_e = \psi_v = \psi_n$ is consistent with our assumption that A_1, B_1, C_1, and D_1 were functions of ϕ_e but not ϕ_n and ψ_v.

After making use of Eqs. (A.15), (A.17), and the prescribed forms for $\vec{v}_z$ and $\vec{B}_y$, expression (A.13) becomes

$$-\frac{3}{2}\kappa_o\omega_o^2 e_o^2 \sin 2\psi_e - \frac{1}{2}\alpha_1\alpha_2 \sin \psi \tag{A.18}$$

where $\alpha_1 = \dfrac{eE_{zi}}{mc\omega_i}$. Equating Eq. (A.18) to the ϵ^1 term in Eq. (A.11) gives

$$2A_1^e \sin \psi_e + 2e_o B_1^e \cos \psi_e + (1 - \omega_o^2) e_o \cos \psi_e$$

$$+ \omega_o^2 \left(\frac{\partial^2 e_1}{\partial \psi_e^2} + e_1\right) = -\frac{3}{2}\kappa_o\omega_o^2 e_o^2 \sin 2\psi_e - \frac{1}{2}\alpha_1\alpha_2 \sin \psi. \tag{A.19}$$

In addition, we define $\phi = \psi_e - \psi$.

To eliminate scalar growth for e_1 we require

$$A_1^e = \frac{\alpha_1\alpha_2}{4} \cos \phi = F \cos \phi \tag{A.20}$$

$$e_o B_1^e = -\frac{\alpha_1\alpha_2}{4}\sin\phi + \frac{(\omega_o^2 - 1)}{2} e_o = -F\sin\phi + \frac{(\omega_o^2 - 1)}{2} e_o \tag{A.21}$$

where

$$F = \frac{\alpha_1\alpha_2}{4} .$$

In addition, from Eq. (A.21) we find

$$e_1 = \frac{1}{2}\kappa_o e_o^2 \sin 2\psi_e . \tag{A.22}$$

We are interested in A_1 and B_1 to second order, so next we proceed to find A_2^e and B_2^e. These are determined from the ϵ^2 coefficients in Eq. (A.1). The contribution from the left-hand side of Eq. (A.6) is found in Eq. (A.11). The ϵ^2 coefficient from the right-hand side of Eq. (A.1) is

$$\epsilon^2\left(\frac{\partial}{\partial t} n_1 v_o + \frac{\partial}{\partial t} n_o v_1 - v_1 \frac{\partial}{\partial x} v_o - v_o \frac{\partial}{\partial x} v_1 + v_o v_z E_z \right.$$

$$\left. + \frac{3}{2} v_o^2 e_o + \frac{1}{2} v_z^2 e_o\right) \tag{A.23}$$

Expressions for n_1 and v_1 as functions of e_1 are determined from the ϵ^1 terms of Ampere's Law and Gauss's Law in Eqs. (A.14) and (A.16), and they are

$$n_1 = -\kappa_o^2 e_o^2 \cos 2\psi_e \tag{A.24}$$

and

$$v_1 = \frac{\alpha_1\alpha_2}{4}\cos(\psi_e + \phi) + \frac{(1 - \omega_o^2)}{2} e_o \sin\psi_e - \kappa_o \frac{\omega_o e_o^2}{2}$$

$$(1 + \cos 2\psi_e). \qquad (A.25)$$

The first term of v_1 is independent of the wave amplitude e_o. Therefore, at early times it is possible for $v_1 > v_o$. This is not true, however, for times larger than ω_o^{-1}, so this term will be neglected. Substituting Eqs. (A.15), (A.17), (A.24), and (A.25) together with the assumed form of E_z into Eq. (A.23) gives

$$\frac{3}{2}\kappa_o^2\omega_o^2 e_o^3 \cos 3\psi_e - \kappa_o^2 \frac{\omega_o^2}{2} e_o^3 \cos\psi_e - \kappa_o(1 - \omega_o^2)\omega_o e_o^2 \sin 2\psi_e$$

$$+ \kappa_o^2 \frac{\omega_o^2}{2} e_o^3 \cos\psi_e - \frac{3}{4}\kappa_o^2\omega_o^2 e_o^3 \cos 3\psi_e - \frac{1}{4}\kappa_o^2\omega_o^2 e_o^3 \cos\psi_e$$

$$- \kappa_o\omega_o \frac{(1 - \omega_o^2)}{2} \sin 2\psi_o + \frac{\kappa_o^2\omega_o^2}{2} e_o^3 \cos\psi_e + \frac{3}{4}\omega_o^2\kappa_o^2 e_o^3 \cos 3\psi_e$$

$$- \frac{\omega_o^2\kappa_o^2}{4} e_o^3 \cos\psi_e + \frac{3}{8}\omega_o^2 e_o^3 \cos\psi_e - \frac{3}{8}\omega_o^2 e_o^3 \cos 3\psi_e$$

$$+ \frac{1}{4}(\alpha_1^2 + \alpha_2^2) e_o \cos\psi_e. \qquad (A.26)$$

Equating Eq. (A.26) to the ϵ^2 term in Eq. (A.11) gives

$$\frac{1}{4} e_o(\alpha_1^2 + \alpha_2^2) + \frac{3}{8}\omega_o^2 e_o^3 = B_1^e \frac{\partial A_1^e}{\partial \phi_e} - e_o B_1^{e2} + 2\omega_o e_o B_2^e + \frac{\partial F}{\partial t}\frac{\partial A_1^e}{\partial F}$$

(A.27)

where the fact that $\frac{\partial A_1^e}{\partial e_o} = 0$ was used. It follows then that

$$\omega_o e_o B_2^e = \frac{1}{8} e_o(\alpha_1^2 + \alpha_2^2) + \frac{3}{16} \omega_o e_o^3 - \mathring{F} \cos \phi \qquad (A.28)$$

where the terms $B_1^e \frac{\partial A_1^e}{\partial \phi_e} - e_o B_1^{e2}$ were neglected since they are higher order. We note that Eq. (A.28) contains only terms due to relativistic and rise time effects. The terms in Eq. (A.26) arising from the harmonics of n_1, v_1, and e_1 cancelled each other. Bingham et al. and Mendonca obtained additional terms in Eq. (A.28) because their v_1 did not contain the D.C. term of Eq. (A.25). In Eulerian coordinates a D.C. fluid velocity does not imply a D.C. current. The second order current is

$$j_1 = -(n_o v_o + v_1) = -(\kappa_o \omega_o e^2 \sin 2\psi_e) + \left(-\kappa_o \frac{\omega_o e_o^2}{2}\right)$$

$$= \kappa_o \omega_o e_o^2 \cos 2\psi_e \qquad (A.29)$$

which has no D.C. component. If the D.C. component of v_1 was absent, then j_1 would have a D.C. component. This would imply that the plasma had a D.C. drift. The magnitude of the accompanying doppler frequency shift would be

$$-\kappa_o j_1 = \frac{1}{2} \kappa_o^2 \omega_o e_o^2 \quad , \qquad (A.30)$$

precisely the magnitude and sign of the extra shift found by

Bingham et al., and by Mendonca. Ampere's Law prevents such a drift by inducing an electric field. When using periodic particle codes, therefore, one must be careful in the choice of the conditions imposed on the $\kappa = 0$ component of the longitudinal electric field.

From Eq. (A.26) we find no contributions to A_2^e. The only contributions to A_2^e, therefore, come from Eq. (A.11)

$$2\omega_o A_2^e = 2A_1^e B_1^e + e_o A_1^e \frac{\partial B_1^e}{\partial e_o} + e_o B_1^e \frac{\partial B_1^e}{\partial \phi_e} + e_o \frac{\partial F}{\partial t} \frac{\partial B_1^e}{\partial F} . \qquad (A.31)$$

The only term on the right-hand side of Eq. (A.31) with low enough order to be of interest is

$$2\omega_o A_2^e = e_o \frac{\partial F}{\partial t} \frac{\partial B_1^e}{\partial F} = - \dot{F} \sin \phi . \qquad (A.32)$$

Consequently, our final set of equations is

$$\omega_o \dot{e}_o = A_1^e + A_2^e = F \cos \phi - \dot{F} \sin \phi \qquad (A.33)$$

$$\omega_o e_o \dot{\phi} = \omega_o e_o (B_1^e + B_2^e) = \frac{\left(\omega_o^2 - 1 + \frac{1}{4}(\alpha_1^2 + \alpha_2^2)\right)}{2} e_o + \frac{3}{16} \omega_o e_o^3$$

$$- F \sin \phi - \dot{F} \cos \phi \qquad (A.34)$$

Equations (A.33) and (A.34) are the well-known set of coupled first-order nonlinear partial differential equations describing Beat Wave excitation of Rosenbluth and Liu and Tang, Sprangle, and

Sudan. The only modification is the inclusion of the terms involving $\dot{F}$ which arise because of the rise time of the pumps. In addition, from the treatment we also have the magnitude of the second harmonic e_1 and third harmonic e_2 as a function of e_0.

In summary, we have shown that the conclusions of Rosenbluth and Liu,[8] Tang et al.,[9] and Noble,[22] that only a relativistic amplitude dependent frequency shift exists, are correct. Bingham et al.[23] and Mendonca[24] erred by using the continuity equation rather than Ampere's Law and imposing the condition $\langle v_1 \rangle = 0$. If they had imposed the condition $\langle j_1 \rangle = 0$ instead, they would have obtained the correct result. We have shown that by using Ampere's Law, $\langle j_1 \rangle$ is forced to vanish (no ambiguity exists). Consequently, no plasma drift ensues and no doppler frequency shift exists. Recently, McKinstrie and Forslund[26] have independently reached similar conclusions.

APPENDIX B

EXCITATION OF PLASMA WAVES WITH $\Delta\omega = 2\omega_p$

The decay of two light waves, whose frequency difference is $2\omega_p$, into a plasma wave was first reported by Rosenbluth and Liu.[8] However, they neglected a term on the same order as the term they retained. Fortuitously, this leads to an error of only a factor of 5/4. In this appendix we review the problem in both Eulerian and Lagrangian coordinates.

The nonlinear driving force [Eq. (13) in the text] to order v^3 is (We use the same dimensionless units of Appendix A.)

$$\left(\frac{\partial}{\partial t}\, n\vec{v} - \vec{v}\cdot\nabla\vec{v}\right) + \vec{v}\vec{v}\cdot\vec{E} + \frac{v^2}{2}\,\vec{E} - \vec{v}\times\vec{B} \qquad \text{(B.1a)}$$

where the term in brackets arises only for Eulerian coordinates. Rosenbluth and Liu carried out the analysis in Lagrangian coordinates and retained only the $\vec{v}\times\vec{B}$ term. Henceforth, we take

$$E_z = E_{z1}\cos\psi_1 + E_{z2}\cos\psi_2 \text{ and } E_x = e_o\cos\psi_o$$

where $\psi_i = \kappa_i x - \omega_i t$ and $\psi_o = x - t$. The forms for the v's and B_i's follow from the above definitions. We rewrite the $\hat{x}$ component of Eq. (B.1a) to obtain the relevant driving terms

$$\left(\frac{\partial}{\partial t}\, nv_x - v_x\,\frac{\partial}{\partial x}\, v_x\right) + v_x v_z E_x + v_z B_z. \qquad \text{(B.1b)}$$

We want to find terms in Eq. (B.1) that possess resonant contributions at ψ_o when $\psi_1 - \psi_2 = 2\psi_o + \phi$. We begin by evaluating each term separately first for Lagrangian coordinates and then we repeat the process for Eulerian coordinates.

$$v_x v_y E_z = e_o \frac{E_{z1}E_{z2}}{\omega_1\omega_2} \sin\psi_o \left[\frac{\Delta\omega}{2}\left(\sin(\psi_1 + \psi_2) - \sin\Delta\psi\right)\right.$$

$$\left. + \omega_2 \sin(\psi_1 + \psi_2)\right] \qquad \text{(B.2a)}$$

and the only possible resonant term is

$$= -e_o \frac{E_{z1}E_{z2}}{\omega_1\omega_2} \frac{\Delta\omega}{4} \cos(\psi_o - \Delta\psi) \qquad \text{(B.2b)}$$

In Lagrangian coordinates $\psi_o \rightarrow \tilde{\psi}_o = x_o - t$ and $\Delta\psi \rightarrow \Delta\kappa[x_o + \xi(x_o,t)] - \Delta\omega t + \phi$ where $x = x_o + \xi(x_o,t)$ and $\xi(x_o,t) = e_o \cos\psi o$. As a result, Eq. (B.2b) reduces to

$$-e_o \frac{E_{z1}E_{z2}}{\omega_1\omega_2} \frac{\Delta\omega}{4}\left(\frac{1}{2} e^{i(\phi+\tilde{\psi}_o)} \sum_{-\infty}^{\infty} i^n J_n(\Delta\kappa e_o) e^{in\tilde{\psi}_o} + c.c.\right) \qquad \text{(B.3a)}$$

with the only resonant contribution of $O(e_o)$ being

$$-e_o F\Delta\omega \cos(\tilde{\psi}_o + \phi) \qquad \text{(B.3b)}$$

where, as before, $F \equiv \frac{E_{z1}E_{z2}}{4\omega_1\omega_2}$.

Likewise, the resonant contribution of the $v_{z1}v_{z2}E_x$ term is

$$v_{z1}v_{z2}E_x = e_o\ F\ \cos(\psi_o - \Delta\psi) \tag{B.4}$$

which for Lagrangian coordinates is

$$e_o\ F\left[\frac{1}{2}\ e^{i(\psi+\bar{\psi}_o)}\ \sum_{-\infty}^{\infty} i^n\ J_n(\Delta\kappa e_o)e^{in\bar{\psi}_o} + c.c.\right] \simeq e_oF\ \cos(\bar{\psi}_o + \phi). \tag{B.5}$$

The v_zB_y term as first found by Rosenbluth and Liu for Lagrangian coordinates is

$$v_zB_y = 4F\left\{\frac{\Delta\kappa}{2}\ \left[\sin\ (\psi_1 + \psi_2) - \sin\ \Delta\psi\right] + \kappa_2\ \sin\ (\psi_1 + \psi_2)\right\} \tag{B.6}$$

with the resonant contribution

$$= -2F\Delta\kappa\ \sin\ \Delta\psi$$

$$= -2F\Delta\kappa\left[\frac{1}{2}\ e^{i(2\tilde{\psi}_o+\phi)}\ \sum_{-\infty}^{\infty} i^n\ J_n(\Delta\kappa e_o)e^{in\psi_o} - c.c.\right]\ . \tag{B.7}$$

The lowest order, $O(e_o)$, contribution is

$$= -2F\Delta\kappa\ J_1(2e_o)\ \cos(\tilde{\psi}_o + \phi)$$

$$\simeq -2Fe_o\Delta\kappa\ \cos(\tilde{\psi}_o + \phi). \tag{B.8}$$

Therefore, the total contribution found using Lagrangian coordinates is for $\Delta\omega = \Delta\kappa = 2$

$$E = e_o \cos \psi_o \tag{B.13a}$$

$$n = e_o \sin \psi_o \tag{B.13b}$$

$$v = e_o \sin \psi_o \ . \tag{B.13c}$$

Hence to $O(e_o)$

$$\frac{\partial}{\partial t} nv - \frac{\partial}{\partial x} \frac{v^2}{2} = \frac{\partial}{\partial t} \left(-\frac{4}{3} e_o F \sin \psi_o \cos(2\psi_o + \phi)\right)$$

$$- \frac{\partial}{\partial x} \left(-\frac{2}{3} F e_o \sin \psi_o \cos(2\psi_o + \phi)\right)$$

$$= - \frac{2}{3} e_o F \cos(\psi_o + \phi) - \frac{1}{3} e_o F \cos(\psi_o + \phi)$$

$$= - e_o F \cos(\varkappa_o + \phi) \tag{B.14}$$

which is identical to the $v_z \beta_y$ term when Lagrangian coordinates were used. The total contribution is therefore

$$-5 F e_o \cos(\psi_o + \phi) \tag{B.15}$$

which is identical to that found using Lagrangian coordinates. The resulting growth rate[8] for the instability is therefore SF/2.